

VIBRATIONAL PROPERTIES OF DISORDERED SYSTEMS

*THESIS SUBMITTED FOR THE DEGREE OF
DOCTOR OF PHILOSOPHY (SCIENCE)
OF THE
UNIVERSITY OF JADAVPUR*

AFTAB ALAM

*SATYENDRANATH BOSE NATIONAL CENTRE
FOR BASIC SCIENCES
JD BLOCK, SECTOR 3, SALT LAKE CITY
KOLKATA 700 098, INDIA*

OCTOBER, 2006

CERTIFICATE FROM THE SUPERVISOR

This is to certify that the thesis entitled **Vibrational properties of disordered systems** submitted by **Aftab Alam**, who got his name registered on **June 29, 2004** for the award of **Ph.D. (Science) degree of Jadavpur University**, is absolutely based upon his own work under the supervision of **Professor Abhijit Mookerjee** at **S. N. Bose National Centre For Basic Sciences, Kolkata, India** and that neither this thesis nor any part of it has been submitted for any degree/diploma or any other academic award anywhere before.

ABHIJIT MOOKERJEE

Senior Professor,

Head, Condensed Matter Physics Group,

Satyendranath Bose National Centre For Basic Sciences,

JD Block, Sector 3, Salt Lake City, Kolkata 700 098

India

Date :

Acknowledgments

I am very happy to express my gratitude to Prof. Abhijit Mookerjee who has been a wonderful thesis adviser. His patience and persistence, insights into various problems, critical thinking and insistence of clarity have been most useful and inspiring. Working with him has been a rich and rare experience and I am indebted to him for reasons much beyond the pages of this thesis.

I would like to express my thanks to my collaborators with whom I had interacted directly at work. I am grateful to Dr. Subhradip Ghosh of Indian Institute of Technology, Guwahati, Assam for his active involvement in the work on first-principles calculation of the vibrational properties of disordered alloys. I am thankful to Dr. Tanusri Saha-Dasgupta of S N Bose National Centre for her fruitful collaboration and continued interest in the work on phase stability of disordered hcp-alloys.

I would like to thank Prof. Ole Krogh Andersen of *Max-Planck Institut, Stuttgart, Germany* for a months visit to his place and an enthusiastic discussion on NMTO-method and maximally localized wannier function. I also would like to thank the *University of Colorado, Boulder, USA* for giving me the opportunity to present some of my very recent work in the *16th Symposium on Thermophysical Properties* held at their place.

I would like to thank my colleagues : Durga (now at *Ames. Lab.*), Kamal (at *Max-Planck Institute, Halle, Germany*), Ainul-Huda (Lecturer in a college at Bangladesh), Kartick as well as Atish, Monodeep, Mukul, Moshour and Shreemoyee of our centre. I have had a nice time with many friends in the institute - Ankush, Soumen, Prasad, Malay, Kuldeep, Priya, Satamita, Shantanu, Rahul, Irfan and Rashidul have been particularly close. It has been fun interacting with them and other students over all these years.

I would like to acknowledge financial support from the Council of Scientific and Industrial Research (CSIR), Government of India during the period of this work.

My sincerest thanks go to my parents, sister and especially to my father for sharing my dreams and for giving me encouragement to work for my goal.

List of Publications

1. **Vibrational properties of phonons in random binary alloys : An augmented space recursive technique in k-space representation**
Aftab Alam and Abhijit Mookerjee
Phys. Rev. B **69** 024205 (2004).
2. **Behaviour of phonon excitations in disordered alloys**
Aftab Alam and Abhijit Mookerjee
Proceedings of the DAE Solid State Physics Symposium Vol. **49**, 590-591 (2004).
3. **Inelastic neutron scattering in random binary alloys : An augmented space approach**
Aftab Alam and Abhijit Mookerjee
Phys. Rev. B **71** 094210 (2005).
4. **Lattice thermal conductivity of disordered binary alloys**
Aftab Alam and Abhijit Mookerjee
Phys. Rev. B **72** 214207 (2005).
5. **Response functions in disordered alloys : an approach via the augmented space recursion.**
Kartick Tarafder, Kamal K. Saha, Aftab Alam and Abhijit Mookerjee
Journal of Physics : conference series **29** 27-38 (2006).
6. **Lattice thermal conductivity of disordered NiPd and NiPt alloys : A numerical study**
Aftab Alam and Abhijit Mookerjee
Journal of Physics : Condens. Matter **18** 4589-4608 (2006).
7. **An augmented space approach to the study of phonons in disordered alloys : Comparison between the itinerant coherent-potential approximation and the augmented space recursion**
Aftab Alam, Subhradip Ghosh and Abhijit Mookerjee
(Communicated to Phys. Rev. B) : (Cond-mat/0610391)

⁰The contents of the paper with serial number (5) is not included in this thesis.

Contents

1	Overview of lattice dynamics calculations	1
1.1	Introduction	1
1.2	Lattice Green function and dispersion curves	5
1.3	Experimentally observed quantities	5
1.3.1	Density of States	5
1.3.2	Coherent structure factors and phonon lifetimes	6
1.3.3	Inelastic Neutron Scattering	6
1.3.4	Thermal Conductivity	7
1.4	The Recursion Method	8
1.4.1	Termination of the Continued Fraction	11
1.4.2	Block Recursion and the Self Energy Matrix	13
2	Configuration Averaging in Disordered systems	16
2.1	Introduction	16
2.2	Mean field theories of disorder : an outline	17
2.2.1	The Virtual Crystal Approximation	18
2.2.2	The Coherent Potential Approximation : its limitations and generalizations	19
2.3	The Augmented Space Formalism	21
2.3.1	The Configuration Space	21
2.3.2	Augmented Space Theorem	24
3	Behavior of phonon excitations in random binary alloys	27
3.1	Introduction	27
3.2	The augmented space formalism for phonons	29
3.3	Dispersion Relations and disorder induced line-widths	36
3.4	Ni ₅₅ Pd ₄₅ face-centered cubic binary alloy (Strong Mass Disorder)	38
3.5	Ni ₈₈ Cr ₁₂ binary alloy (Strong Force constant disorder)	42
3.6	Ni ₅₀ Pt ₅₀ alloy (Strong Mass and Force constant disorder)	45

3.7	Concluding Remarks	48
4	The Itinerant CPA and Augmented Space Recursion	49
4.1	Introduction	49
4.2	The Itinerant CPA and Augmented space recursion	51
4.3	First principles calculations of force constants in alloys	54
4.3.1	Density functional perturbation theory	55
4.3.2	Random alloy force constants from DFPT	55
4.3.3	Details of first-principles calculations	56
4.4	Results and Discussions	57
4.5	CONCLUSIONS	63
5	Inelastic neutron scattering in random binary alloys	67
5.1	Introduction	67
5.2	The Formulation	69
5.3	A generalized multiple scattering diagram approach	73
5.4	Coherent and Incoherent Inelastic scattering cross sections	80
5.5	RESULTS AND DISCUSSION	85
5.5.1	Ni₅₅Pd₄₅ Alloy	86
5.5.2	Ni₅₀Pt₅₀ Alloy	88
5.6	Concluding Remarks	93
6	Thermal transport in disordered binary alloys	94
6.1	Introduction	94
6.2	Lattice Thermal Conductivity : A Kubo Greenwood formulation	96
6.3	Effects of disorder scattering correction : A scattering diagram approach	99
6.3.1	Configuration averaging of lattice thermal conductivity	101
6.3.2	The vertex correction	109
6.4	Configuration averaged thermal diffusivity	115
6.5	Details of Numerical Implementation	117
6.6	Results and Discussion	118
6.6.1	NiPd alloy : Strong mass and weak force constant disorder.	118

6.6.2	NiPt alloy : Strong mass and force constant disorder	126
6.7	Conclusion	132
7	An assessment of the work and future plans	135
7.1	Concluding Remarks	135
7.2	Future directions	137

List of Figures

2.1	Schematic diagram illustrating spatial ergodicity. Each subsystem shown here resembles a configuration when the size diverges. The composition shown here is 45% - 55%	17
2.2	A schematic diagram for the self-consistency of the CPA	19
3.1	Total coherent structure factors in different directions with different branches for $\text{Ni}_{55}\text{Pd}_{45}$. In each of the different directions and branches, the various curves indicate the total structure factors for various ζ values starting from the lowest value to the edge of the Brillouin zone. In $[\zeta 0 0]$ direction T1 and T2 modes are degenerate, in $[\zeta \zeta 0]$ direction L and T1 modes are degenerate and in $[\zeta \zeta \zeta]$ direction all the three modes are degenerate. The y-axis is in an arbitrary scale with heights scaled to the maximum height. Different curves for different ζ values are shifted along the x-axis in order to facilitate vision.	41
3.2	Dispersion Curves (frequency ν vs. reduced wave vector ζ) for $\text{Ni}_{55}\text{Pd}_{45}$ calculated from recursion (solid line). The force constants used are given in the text. The filled circles are the experimental data [Kamitakahara and Brockhouse, 1974]. In all the three panels the thin dotted lines span the FWHM's.	42
3.3	Full widths at half-maximum for the NiPd alloy as function of frequency for different directions in k-space and different modes without (left) and with (right) the inclusion of the scattering length fluctuation. The filled circles along with the error bars are the experimental data [Kamitakahara and Brockhouse, 1974]	43
3.4	Dispersion Curves (frequency ν vs. reduced wave vector ζ) for $\text{Ni}_{88}\text{Cr}_{12}$ calculated from recursion (solid line). The force constants used are given in the text. The filled circles are the 2 CPA results of R.P.Singh's thesis 1982. In all the three panels the thin dotted lines span the FWHM's.	44

3.5	Full widths at half-maximum for the NiCr alloy as function of frequency for different directions in k-space and different modes.	45
3.6	Dispersion Curves (frequency ν vs. reduced wave vector ζ) for Ni ₅₀ Pt ₅₀ calculated from recursion . The force constants used are given in the text. The solid lines are the L-branch in all the three panels, the dashed lines are the T-branch in the left and right panels. In the $[\zeta \zeta 0]$ direction the dashed line indicate the T1 branch while the dot-dashed line indicate the T2 branch. The filled circles are the ICPA results [Ghosh <i>et al</i> 2002]. In all the three panels the thin dotted lines span the FWHM's.	46
3.7	Full widths at half-maximum for the NiPt alloy as function of frequency for different directions in k-space and different modes including the scattering length fluctuation.	47
4.1	Dispersion Curves (frequency ν vs. reduced wave vector ζ) for Fe ₅₀ Pd ₅₀ alloy. The upper panel correponds to the ASR results however the lower panel to the ICPA results. The filled circles are the experimental data Mahaddene <i>et al</i> 2004. The force constants used are given in Table 4.1.	58
4.2	Partial and total structure factors calculated in the ICPA for various ζ -values along the $[\zeta, 0, 0]$ and $[\zeta, \zeta, \zeta]$ directions in Fe ₅₀ Pd ₅₀ alloy. The solid line are the total contribution, the dotted lines are the Fe-Pd spectra, the long-dashed lines are the Fe-Fe spectra, and the dot-dashed lines are the Pd-Pd contributions. The type of mode is labelled along a particular symmetry direction. The force constants used are given in Table 4.1. The details are given in the text.	59
4.3	Dispersion Curves (frequency ν vs. reduced wave vector ζ) for Fe ₅₀ Pd ₅₀ alloy. The upper panel correponds to the ASR results however thelower panel to the ICPA results. The filled circles are the experimental data Mahaddene <i>et al</i> 2004. The error bar in the ASR result basically represents the full widths at half maxima (FWHM) at various ζ values. The force constants used are given in Table 4.2.	61
4.4	Same as Fig. 4.2 but with the force constants of Table 4.2. Other details are given in the text.	63
4.5	Phonon density of states for Fe ₅₀ Pd ₅₀ alloy. The upper and lower panel shows ICPA and ASR results respectively. The force constants used are that of experiment given in Table 4.2.	64

4.6	Disorder-induced FWHM's vs wave vector (ζ) for $\text{Fe}_{50}\text{Pd}_{50}$ alloy. The upper and lower panels show ASR and ICPA results respectively. The force constants used are given in Table 4.2.	65
4.7	Total coherent structure factors in different directions with different branches for $\text{Fe}_{50}\text{Pd}_{50}$ alloy. The upper and lower box shows ASR and ICPA results respectively. In each of the different directions and branches, the various curves indicate the total structure factors for various ζ values starting from the lowest value to the edge of the Brillouin zone. For the ASR result, the T1 and T2 modes are degenerate along $[\zeta 00]$ direction, L and T1 modes are degenerate along the $[\zeta \zeta 0]$ direction, however all the three modes are degenerate along the $[\zeta \zeta \zeta]$ directions. In the ICPA result, non of the modes are degenerate. Such differences are hidden inside the structure of two different calculations. In both the boxes, the different curves for different ζ values are shifted along the x-axis in order to facilitate vision.	66
5.1	Bond coherent potential approximations	71
5.2	Our model, where the correlation between bonds arises because of the common vertex which is random	72
5.3	The scattering vertices for the averaged Green function	73
5.4	The scattering diagrams for n=2.	75
5.5	The topologically distinct scattering diagrams for n=3.	76
5.6	The topologically distinct classes of scattering diagrams for n=4.	77
5.7	Structure of skeleton diagrams for the self-energy	78
5.8	Details of some skeleton diagrams for the self-energy	79
5.9	The scattering vertices related to the fluctuations in W	81
5.10	The scattering diagrams for the inelastic scattering cross-section	82
5.11	The coherent scattering cross section in different directions for $\text{Ni}_{55}\text{Pd}_{45}$. In each of the different directions, the various curves indicate the cross sections for various ζ values starting from the lowest value to the edge of the Brillouin zone. The y-axis is in an arbitrary scale with heights scaled to the maximum height. Different curves for different ζ values are shifted along the x-axis in order to facilitate vision.	87

5.12	The incoherent scattering cross sections in different directions for $Ni_{55}Pd_{45}$ alloy with $\Phi_{Ni-Pd} = 0.7 \Phi_{Ni-Ni}$. In each of the different directions, the various curves indicate the cross sections for various ζ values starting from the lowest value to the edge of the Brillouin zone.	89
5.13	Same as Fig. (5.11) but for $Ni_{50}Pt_{50}$ alloy	90
5.14	Same as Fig. (5.13) but for $Ni_{50}Pt_{50}$ alloy.	91
5.15	The incoherent scattering cross section for $Ni_{50}Pt_{50}$. The left panel, middle panel and right panel display the block recursion result, experimental curve and the CPA result respectively.	92
6.1	The scattering vertices for the averaged Green function	100
6.2	The scattering vertices associated with the random current terms	103
6.3	The VCA or zero-th order approximation for $\ll \kappa(z_1, z_2) \gg$	104
6.4	Few examples of scattering diagrams where no disorder line joins the two phonon propagators.	104
6.5	Scattering diagrams contributing to effective heat current.	105
6.6	The scattering diagrams associated with joint fluctuations of one current term and two propagators.	107
6.7	The scattering diagrams associated with joint fluctuations of two current terms and one propagator.	108
6.8	The scattering diagrams leading to vertex correction.	110
6.9	The Bethe-Salpeter equation for the thermal conductivity	110
6.10	The ladder scattering diagrams for the vertex correction.	111
6.11	The structure of infinite series of ladder diagrams contributing to the correlation function $\ll \kappa(z_1, z_2) \gg$	114
6.12	Configuration averaged lattice thermal conductivity vs phonon frequency ν (THz) for $Ni_{50}Pd_{50}$ disordered alloy. The red line and black line shows the conductivity using the average VCA current and effective current (consisting of average VCA current + disorder corrections + vertex correction) respectively. The green line in indicates the configuration averaged joint density of states.	119

6.13	Thermal conductivity vs temperature T(K) for NiPd alloys and Amorphous Si. The top panel shows our results on the lattice conductivity for Ni ₉₉ Pd ₀₁ alloy at three different frequency cut-off ν . The middle panel shows the lattice conductivity for amorphous Si [Feldman <i>et al</i> 1993] at three different cut-off frequency, while the panel at the bottom shows the experimental data [Farrell and Greig 1969] for the total thermal conductivity (= lattice + electronic contribution) of the same Ni ₉₉ Pd ₀₁ alloy.	121
6.14	Residual or impurity contribution of the electronic part of the thermal conductivity	122
6.15	κ vs T^2 for low temperatures for 50-50 NiPd alloy	123
6.16	The configuration averaged lattice thermal conductivity vs phonon frequency ν (THz) at different temperatures T for Ni ₅₀ Pd ₅₀ alloy.	124
6.17	Frequency dependence of lattice thermal conductivity for various alloys Ni _{1-x} Pd _x at T=100 K.	125
6.18	The configuration averaged thermal diffusivities $D(\nu)$ for Ni _{1-x} Pd _x alloys. (a) x=0.1; (b) x=0.3; (c) x=0.5; (d) x=0.7; (e) x=0.9. The broad line on the frequency axis shows the extent of the vibrational spectrum.	126
6.19	The behaviour of thermal diffusivity as a function of $(\nu_c - \nu)^\alpha$	127
6.20	The position of the mobility edge (bottom) and the percentage of mobile phonon states (top) as a function of the alloy composition for NiPd alloy. .	128
6.21	Same as Fig. (6.12) but for Ni ₅₀ Pt ₅₀ disordered alloy.	129
6.22	The averaged lattice thermal conductivity vs temperature T(K) at various cut-off frequency ν_{cutoff} for Ni ₅₀ Pt ₅₀ alloy.	130
6.23	Lattice thermal conductivity vs Pt-concentration for various temperature T at phonon frequency $\nu = 1.05 THz$	131
6.24	Same as Fig. (6.18) but for Ni ₅₀ Pt ₅₀ alloy.	132
6.25	Same as Fig. (6.20) but for Ni ₅₀ Pt ₅₀ alloy.	133

List of Tables

3.1	General properties of fcc Ni, Pd, Pt and Cr. The force constants for Ni, Pd and Pt are taken from Dutton <i>et al</i> 1972 and that for Cr is taken from Mookerjee and Singh 1988	39
4.1	Real-space nearest neighbor force constants for Fe ₅₀ Pd ₅₀ obtained by DFPT calculations on the artificial ordered structure. The units are dyn cm ⁻¹ . . .	57
4.2	Real-space nearest neighbor force constants for Fe ₅₀ Pd ₅₀ obtained from experimental data Mahaddene <i>et al</i> 2004 on L10 structure at 860K. The units are dyn cm ⁻¹	62

Chapter 1

Overview of lattice dynamics calculations

1.1 Introduction

The subject matter of this thesis is the lattice vibrational properties of disordered binary alloys. The varied chemical and physical properties of alloys pose a stimulating challenge to physicists and, for a thorough understanding of these diverse physical phenomena, a sound theoretical frame work is necessary. Disorder in alloys may appear in various forms like topological, substitutional, positional and so on. In this work we shall be concerned with substitutional disorder only. Atoms in alloys with substitutional disorder sit on an underlying crystalline lattice but the lattice sites are occupied by the constituent atoms randomly with varying degree of statistical correlations.

Let us focus our attention on disordered binary alloys. When atoms of different masses and force constant matrices alloy substitutionally in a crystal, there are, in general, three types of changes to the system Hamiltonian : diagonal disorder arising from the mass difference $m_A - m_B$; off-diagonal disorder arising from differences in the force constant matrix Φ_{ij} (where j is some neighbouring sites of i) which can take values Φ_{ij}^{AA} , Φ_{ij}^{AB} or Φ_{ij}^{BB} ; and environmental disorder arising from the diagonal term of the force constant matrix Φ_{ii} which is related to its environment by the sum rule $\Phi_{ii} = -\sum_k \Phi_{ik}$. Unlike the electronic problem, such types of disorder are coupled in the phonon problem. This necessitates careful reformulation of the usual ideas of dealing with disorder problems with statistically independent variables.

A discussion of the vibrational properties of alloys will certainly require a digression on lattice dynamics calculations. We shall frame a brief overview of the phonon problem.

Let us begin by considering system consisting of N_c ion-cores bonded in a solid by N_e valence electrons. The many body Hamiltonian is :

$$H = \sum_{I=1}^{N_c} \frac{P_I^2}{2M_I} + \sum_{i=1}^{N_e} \frac{p_i^2}{2m_e} + V_{ee}(\{\mathbf{r}\}) + V_{eN}(\{\mathbf{r}\}, \{\mathbf{R}\}) + V_{NN}(\{\mathbf{R}\})$$

where V_{ee} , V_{NN} and V_{eN} are the Coulomb interactions between the electrons, the ions themselves and between the electrons and ions. We can group the terms as follows :

$$H = H_e + T_N(\{\mathbf{R}\}) + V_{NN}(\{\mathbf{R}\})$$

where T_N is the kinetic energy of the ion-cores.

Schrodinger equation for the total Hamiltonian H is :

$$H \Psi(\{\mathbf{r}\}, \{\mathbf{R}\}) = E \Psi(\{\mathbf{r}\}, \{\mathbf{R}\}) \quad (1.1)$$

Since the time scale corresponding to electron dynamics is much smaller than that of the ions, we can carry out the Born-Oppenheimer or adiabatic approximation which assumes that during the short time the electron dynamically evolves, the ions are frozen or stationary. This allows us to solve the electronic problem with a fixed ion-core configuration.

$$H_e \phi_n(\{\mathbf{r}\}, \{\mathbf{R}\}) = \mathcal{E}_n(\{\mathbf{R}\}) \phi_n(\{\mathbf{r}\}, \{\mathbf{R}\}) \quad (1.2)$$

Using the separability condition on the wave-function we may write :

$$\Psi(\{\mathbf{r}\}, \{\mathbf{R}\}) = \sum_n \Theta_n(\{\mathbf{R}\}) \phi_n(\{\mathbf{r}\}, \{\mathbf{R}\}) \quad (1.3)$$

Substituting Eqn. (1.3) in Eqn. (1.1) we get

$$\left[T_N + \mathcal{E}_m(\{\mathbf{R}\}) + V_{NN}(\{\mathbf{R}\}) \right] \Theta_m(\{\mathbf{R}\}) + \sum_n \Lambda_{mn}(\{\mathbf{R}\}) \Theta_n(\{\mathbf{R}\}) = E \Theta_m(\{\mathbf{R}\}) \quad (1.4)$$

where

$$\Lambda_{mn}(\{\mathbf{R}\}) = \sum_I -\frac{\hbar^2}{2M_I} \left[\mathcal{A}_{mn}^I \frac{\partial}{\partial R_I} + \frac{1}{2} \mathcal{B}_{mn}^I \right]$$

with

$$\mathcal{A}_{mn}^I = \langle \phi_m | \frac{\partial}{\partial R_I} | \phi_n \rangle \quad \mathcal{B}_{mn}^I = \langle \phi_m | \frac{\partial^2}{\partial R_I^2} | \phi_n \rangle$$

The adiabatic approximation now neglects the second term in the right hand side of Eqn. (1.4) :

$$\left[T_N + \mathcal{E}_m(\{\mathbf{R}\}) + V_{NN}(\{\mathbf{R}\}) \right] \Theta_m(\{\mathbf{R}\}) = E \Theta_m(\{\mathbf{R}\}) \quad (1.5)$$

The effect of the term Λ_{mn} , which we have neglected under the adiabatic approximation is to couple the nuclear states $\Theta_m(\{\mathbf{R}\})$ pertaining to different electronic states and they allow non-radiative transitions between the electronic states.

The Born-Oppenheimer Hamiltonian for the ion-cores is given by Eqn. (1.5) as :

$$H^I = \sum_{I=1}^{N_c} \frac{P_I^2}{2M_I} + V_{eff}(\{\mathbf{R}\})$$

with potential energy

$$V_{eff}(\{\mathbf{R}\}) = \mathcal{E}_m(\{\mathbf{R}\}) + \sum_{I>J} \frac{Ze^2}{|\mathbf{R}_I - \mathbf{R}_J|} \quad (1.6)$$

The potential energy is a minimum for a configuration which is the equilibrium lattice. In terms of the basis vectors $\mathbf{a}_1, \mathbf{a}_2, \mathbf{a}_3$ let the equilibrium position of the ions are denoted by \mathbf{R}^o as :

$$\mathbf{R}_I^o = l_1 \mathbf{a}_1 + l_2 \mathbf{a}_2 + l_3 \mathbf{a}_3$$

where l_1, l_2, l_3 are any set of integers (+ve, -ve or zero).

Now as a result of thermal fluctuations at finite temperatures, the constituent atoms in a crystalline solid execute small oscillation about their equilibrium positions. Let the displacement of atom from its equilibrium position be $\mathbf{u}(\mathbf{R}_I, t)$, so that the displaced position is

$$\mathbf{R}_I = \mathbf{R}_I^o + \mathbf{u}(\mathbf{R}_I, t)$$

For small oscillations, we may expand the potential energy in Eqn. (1.6) in powers of displacement. The series may be expected to converge rapidly if the displacements are small compared to inter-atomic spacing.

$$V_{eff}(\mathbf{R}) = V_{eff}(\mathbf{R}_0) + \frac{1}{2} \sum_{IJ} \sum_{\mu\nu} \frac{\partial^2 V_{eff}}{\partial u_\mu(\mathbf{R}_I) \partial u_\nu(\mathbf{R}_J)} \Big|_0 u_\mu(\mathbf{R}_I) u_\nu(\mathbf{R}_J) + \dots \quad (1.7)$$

This is the harmonic approximation. The equation of motion then becomes :

$$M_I \ddot{u}_\mu(\mathbf{R}_I) = - \frac{\partial V_{eff}(\{\mathbf{R}\})}{\partial u_\mu(\mathbf{R}_I)} = - \sum_{J,\nu} \frac{\partial^2 V_{eff}(\{\mathbf{R}\})}{\partial u_\mu(\mathbf{R}_I) \partial u_\nu(\mathbf{R}_J)} \Big|_0 u_\nu(\mathbf{R}_J) \quad (1.8)$$

Let us denote

$$\Phi_{\mu\nu}(\mathbf{R}_I, \mathbf{R}_J) = \left. \frac{\partial^2 V_{eff}(\{\mathbf{R}\})}{\partial u_\mu(\mathbf{R}_I) \partial u_\nu(\mathbf{R}_J)} \right|_o,$$

$\Phi_{\mu\nu}(\mathbf{R}_I, \mathbf{R}_J)$ are the *force constants* which satisfy the following conditions,

- $\Phi_{\mu\nu}(\mathbf{R}_I, \mathbf{R}_J) = \Phi_{\nu\mu}(\mathbf{R}_J, \mathbf{R}_I)$
- The translational symmetry of the lattice requires

$$\Phi_{\mu\nu}(\mathbf{R}_I, \mathbf{R}_J) = \Phi_{\nu\mu}(\mathbf{R}_I - \mathbf{R}_J)$$
- If we wish to eliminate the uniform translation mode, then Eqn. (1.8) gives the following condition on the force constants :

$$\sum_J \Phi_{\mu\nu}(\mathbf{R}_I - \mathbf{R}_J) = 0 \Rightarrow \Phi_{\mu\nu}(0) = - \sum_{J \neq I} \Phi_{\mu\nu}(\mathbf{R}_I - \mathbf{R}_J)$$

Let us choose a monochromatic oscillatory solution of Eqn. (1.8) as :

$$u(\mathbf{R}, t) = \frac{1}{\sqrt{N}} \mathbf{e}^{i(\mathbf{k} \cdot \mathbf{R} - \omega t)} \boldsymbol{\epsilon}$$

This leads to the equation :

$$\left[\mathbf{M}\omega^2 - \mathbf{D}(\mathbf{k}) \right] \boldsymbol{\epsilon} = 0 \quad (1.9)$$

where \mathbf{D} is a Hermitian matrix called the *Dynamical matrix* whose elements are given by

$$D_{\mu\nu}(\mathbf{k}) = \sum_{\mathbf{R}} \Phi_{\mu\nu}(\mathbf{R}) \mathbf{e}^{-i\mathbf{k} \cdot \mathbf{R}}$$

Equation (1.9) represents a set of three linear homogeneous equations in three unknown ϵ_ν ($\nu=1,2,3$). The three solutions $\omega_p(\mathbf{k})$ ($p=1,2,3$) for each value of \mathbf{k} are obtained by finding roots of the determinantal *Secular equation* :

$$\det(\mathbf{M}\omega^2 - \mathbf{D}) = 0$$

The relation between the frequency ω and the wave-vector \mathbf{k} for a polarization index p is known as the dispersion relation.

$$\omega = \omega_p(\mathbf{k}), \quad p = 1, 2, 3$$

1.2 Lattice Green function and dispersion curves

The basic problem of the theory of phonons in a most general 3-D realistic system is to solve a secular equation of the form of Eqn. (1.9). The Green function corresponding to the displacement vector ϵ is

$$G_{nn}(\mathbf{k}, \omega^2) = \langle n | (\mathbf{M}\omega^2 - \mathbf{D}(\mathbf{k}))^{-1} | n \rangle \quad (1.10)$$

where the mass operator \mathbf{M} and the dynamical matrix operator \mathbf{D} in terms of a tight binding representation is given by

$$\begin{aligned} \mathbf{M} &= \sum_R m_R \delta_{\mu\nu} P_R \\ \mathbf{D} &= \sum_R D_{RR}^{\mu\nu} P_R + \sum_{RR'} D_{RR'}^{\mu\nu} T_{RR'} \end{aligned} \quad (1.11)$$

Equation (1.10) can also be expressed in the form

$$G_{nn}(\mathbf{k}, \omega^2) = \langle n_s | (\omega^2 \mathbf{I} - \mathbf{H}(\mathbf{k}))^{-1} | n_s \rangle \quad (1.12)$$

where $n_s = \mathbf{M}^{-1/2} | n \rangle$ and $\mathbf{H}(\mathbf{k}) = \mathbf{M}^{-1/2} \mathbf{D} \mathbf{M}^{-1/2}$.

The spectral function can be calculated by just taking the imaginary part of $G_{nn}(\mathbf{k}, \omega^2)$. The dispersion relation can then be obtained by simply finding the peak positions of this spectral function for each wave-vector \mathbf{k} along a particular symmetry direction for the concerned lattice.

1.3 Experimentally observed quantities

1.3.1 Density of States

The vibrational (phonon) density of states $\rho(\omega)$ is related to the *mass weighted* displacement-displacement Green function as

$$\rho(\omega) = -\frac{2\omega}{3\pi} \sum_{\lambda} \int_{BZ} \frac{d^3\mathbf{k}}{8\pi^3} \Im m \left[\mathbf{Tr} \{ \mathbf{G}^{\lambda}(\mathbf{k}, \omega^2) \} \right] \quad (1.13)$$

where λ labels the particular normal mode branch, the integration is over the entire Brillouin zone (BZ) and \mathbf{G} is given by Eqn. (1.12). The expression holds good if one gets the

normal mode easily [Maradudin *et al* 1971]. But in disordered lattices, the identification of normal modes seems to be difficult because of lack of translational invariance. The evaluation becomes even more difficult in the reciprocal space representation. However under the theoretical framework of our formalism combined with the recursion method, it comes out to be tractable with quite a good accuracy. The recursion method is explained in the following Section 2.4.

1.3.2 Coherent structure factors and phonon lifetimes

Experimental determination of the phonon dispersion and line widths are from the coherent scattering structure factors defined as

$$\mathbf{S}_{coh}^\lambda(\mathbf{k}, \omega^2) = -\frac{1}{\pi} \Im m \left[\mathbf{Tr} \{ \mathbf{b} \mathbf{G}^\lambda(\mathbf{k}, \omega^2) \mathbf{b} \} \right]$$

where \mathbf{b} stands for the scattering length operator related to the scattering length of the nucleus of atoms. The actual dispersion curves comparable to the experiments are obtained by finding the peak positions for these structure factors for each phonon modes along various symmetry directions.

The disorder induced effects make the coherent structure factors look like Lorentzians. The phonon lifetimes are obtained by just taking the inverse of full widths at half maxima of these Lorentzian shaped structure factors.

1.3.3 Inelastic Neutron Scattering

The formal expression for the inelastic cross-section for the scattering of thermal neutrons from an initial state labelled by \mathbf{k} to a final state \mathbf{k}' with a change of energy $E = \hbar\omega = \frac{\hbar^2}{2M_n}(k^2 - k'^2)$ and a change of wave-vector $\mathbf{q} = \mathbf{k} - \mathbf{k}' + \mathbf{Q}$, where \mathbf{Q} is a reciprocal lattice vector is:

$$\frac{d^2\sigma}{d\Omega dE} = \frac{1}{2N\hbar} \frac{k'}{k} \sum_R \sum_{R'} \sum_{\alpha\beta} q^\alpha q^\beta \left(W_R \Im m G_{RR'}^{\alpha\beta}(\omega) W_{R'} \right) n(\omega) \exp \{ i\mathbf{q} \cdot (\mathbf{R} - \mathbf{R}') \}$$

where $W_R = w_R \{ \exp[-(1/2)\langle (\mathbf{q} \cdot \mathbf{u}_R)^2 \rangle_{th}] \}$ and w_R is the scattering length of the nucleus of an atom sitting at R , its equilibrium position, and $\mathbf{u}_R(t)$ is its deviation from equilibrium at the time t . $n(\omega)$ is the Bose distribution function.

The total inelastic neutron scattering cross section consists of a coherent and incoherent part. The coherent part is related to a weighted average over the displacement-displacement correlation function. It allows a direct measurement of $\mathbf{G}(\mathbf{k}, \omega)$ and gives the most detailed experimental information about phonons in mixed crystals. However the incoherent scattering cross section is related to a weighted average of the single site Green function and hence to the density of states. The separation of the total inelastic neutron scattering cross section into the coherent and incoherent part for a perfect crystal is quite straight forward and the theory has been set up on a rigorous basis [Sjölander 1964, Lovesey and Marshall 1971]. However we must make the same statement for disordered alloys with more care. This is because the theory of neutron scattering in random alloys require two basic inputs : first is the formulation of the problem and second its actual numerical implementation in realistic situations. In chapter 5 we shall discuss a multiple scattering diagram technique to suggest how to separate the coherent and incoherent part of the total inelastic scattering cross section for disordered binary alloys.

1.3.4 Thermal Conductivity

The Kubo formula which relates the optical conductivity to a current-current correlation function is well established. For the case of an electron in an electro-magnetic field, the Hamiltonian contains a term $\mathbf{j} \cdot \mathbf{A}(\underline{r}, t)$ which drives the electrical current. For thermal conductivity we do not have a similar term in the Hamiltonian which drives a heat current. The derivation of a Kubo formula in this situation requires an additional statistical hypothesis, which states that a system in steady state has a space dependent *local* temperature $T(\underline{r}) = [\kappa_B \beta(\underline{r})]^{-1}$. The expression for the lattice thermal conductivity has been discussed in great detail by Allen and Feldman 1993. Keeping in mind the heat conduction through a solid due to the existence of a temperature gradient, the formal expression for the lattice thermal conductivity is given by the Kubo-Greenwood formula as :

$$\kappa(\omega, T) = \frac{1}{3\pi T} \sum_{\mu} \int d\omega' \int \frac{d^3\mathbf{k}}{8\pi^3} \text{Tr} \left[\hat{\mathbf{S}}^{\mu}(\mathbf{k}, T) \Im m\{\mathbf{G}(\mathbf{k}, \omega')\} \hat{\mathbf{S}}^{\mu}(\mathbf{k}, T) \Im m\{\mathbf{G}(\mathbf{k}, \omega' + \omega)\} \right] \quad (1.14)$$

where the summation is over the direction indices, the integration is over the entire Brillouin zone, $\widehat{\mathbf{S}}$ is the heat current operator given by the following expression :

$$\widehat{\mathbf{S}}_{\gamma\gamma'}^{\mu}(\mathbf{k}) = \frac{\hbar}{2} (\omega_{\mathbf{k}\gamma} + \omega_{\mathbf{k}\gamma'}) \mathbf{v}_{\gamma\gamma'}^{\mu}(\mathbf{k}, T)$$

where ω 's are the eigen-frequencies of various modes of vibration labelled by γ, γ' . \mathbf{k} is the reciprocal wave-vector and \mathbf{v} is the phonon group velocity which depends on temperature via the Bose distribution function $n(\omega, T)$. Also \mathbf{G} is the Green matrix in the reciprocal space representation.

For disordered materials, we have to calculate the configuration averaged lattice thermal conductivity, which require the average of the product of four random functions as in the right hand side of Eqn. (1.14). The evaluation of such an average purely analytically is extremely cumbersome, however a multiple scattering diagram approach makes this calculation quite simpler. We shall discuss this calculation in detail in chapter 6 for disordered binary alloys.

Although a direct comparison of the theoretical result (based on the lattice conductivity) with the experimental data for the thermal conductivity is difficult, because the experimental thermal conductivity also has a component arising out of the contribution from electrons. We have nevertheless compared the two results in chapter 6 subtracting a hypothetical electronic contribution using the Wiedemann-Franz law in our theoretical framework.

1.4 The Recursion Method

We shall now describe a powerful technique for the calculation of the Green function and the related quantities described in the previous section. The Recursion method was introduced by Haydock *et al* 1972 to deal with systems without lattice translation symmetry and has since proved to be one of the important calculational techniques in this area.

It has been argued by Heine (Heine 1980) that many of the properties of solids are dependent on the local chemistry of the atoms constituting the solid. He enunciated a black body theorem for such properties, which essentially states that the very far environment

of an atom in solid has very little influence on its local chemistry. In other words the physics is better understood by means of a solution that explicitly accounts for the role of local environment. The recursion method introduced by Haydock *et al* 1972 is a lucid approach in this direction. It expresses the Hamiltonian in a form that couples an atom to its first nearest neighbours, then through them to its distant neighbours and so on.

The central idea in this method is to calculate the physical quantities of interest by expressing themselves directly or indirectly as a diagonal matrix element of the Green operator. The recursion method is simply a tool for the calculation of the diagonal matrix element of the resolvent operator by transforming the original Hamiltonian to a tridiagonal representation. Starting with $|\phi_{i,\alpha}\rangle = |0\rangle$, an initial phonon mode basis or a suitable combination of modes, which define the physical quantity to be calculated at the site i , we construct a new state $|1\rangle$ as

$$b_1|1\rangle = H|0\rangle - a_0|0\rangle$$

The whole set of orthogonal states are generated by the following three term recurrence relation :

$$b_{n+1}|n+1\rangle = H|n\rangle - a_n|n\rangle - b_n|n-1\rangle \quad (1.15)$$

a_n and b_n are the coefficients to orthogonalize $H|n\rangle$ to the preceding vectors $|n\rangle$, $|n-1\rangle$ and b_{n+1} is the coefficient to normalize $|n+1\rangle$ to unity. b_0 is assumed to be unity. In the new basis the Hamiltonian matrix elements are

$$\frac{\langle n|H|n\rangle}{\langle n|n\rangle} = a_n \quad \frac{\langle n-1|H|n\rangle}{[\langle n|n\rangle\langle n-1|n-1\rangle]^{1/2}} = b_n \quad \langle n|H|m\rangle = 0 \quad (1.16)$$

The Hamiltonian H in the new basis has the following tridiagonal form :

$$\begin{pmatrix} a_0 & b_1 & 0 & 0 & 0 & \dots \\ b_1 & a_1 & b_2 & 0 & 0 & \dots \\ 0 & b_2 & a_2 & b_3 & 0 & \dots \\ 0 & 0 & b_3 & a_3 & b_4 & \dots \\ 0 & 0 & \ddots & \ddots & \ddots & \dots \end{pmatrix}$$

For systems where the lattice symmetry breaks down, we can not apply Bloch's theorem, so we take recourse to an alternative approach to calculate the vibrational properties

instead of solving Schrodinger equation. In this approach, properties are extracted from the corresponding Green function of the system which is defined as the resolvent of the Hamiltonian :

$$\mathbf{G}(z) = (z\mathbf{I} - \mathbf{H})^{-1}$$

In the recursion method, we use the same approach and calculate the diagonal elements of the Green function which is directly related to the density of states, spectral function, structure factors etc. and most of the material properties follow thereafter. The starting state of recursion is then :

$$|0\rangle = |R, \alpha\rangle$$

where R indicates the position of the R -th unit cell and α the Cartesian direction. The diagonal element of the Green function by definition is,

$$G_{00}(E) = \langle 0 | (E\mathbf{I} - \mathbf{H})^{-1} | 0 \rangle = \frac{M_1(E)}{M_0(E)} = \frac{1}{R_1(E)}$$

where M_0 and M_1 are the determinant of the matrix $(E\mathbf{I} - \mathbf{H})^{-1}$ (represented in the new basis $\{|n\rangle\}$) and the determinant of the matrix obtained from the original matrix by deleting the first row and column respectively.

Using Cauchy's expansion theorem,

$$\begin{aligned} M_n(E) &= (E - a_n)M_{n+1} - b_{n+1}^2 M_{n+2} \\ R_{n+1} &= E - a_n - \frac{b_{n+1}^2}{R_{n+2}} \end{aligned} \quad (1.17)$$

This suggests that it is possible to express the Green function as a continued fraction expansion characterized by a set of coefficients,

$$G_{00}(E) = \frac{1}{E - a_0 - \frac{b_1^2}{E - a_1 - \frac{b_2^2}{E - a_2 - \frac{b_3^2}{E - a_3 - \frac{b_4^2}{\ddots}}}}} \quad (1.18)$$

where the coefficients $\{a_n\}$ and $\{b_n\}$ are the ones appearing in the tridiagonal matrix H .

1.4.1 Termination of the Continued Fraction

The recursive calculation described earlier gives rise to a set of continued fraction coefficients $\{a_n, b_n\}$. In any practical calculation we can go only up to a finite number of steps, consistent with our computational process. If one tries to model an infinitely extended system, the recursion algorithm after n -steps contains contributions only from a central cluster of $O(n^3)$ atoms. For numerical purpose, this limits the number of atoms that can be modeled, and also implies that one is always studying a finite system. The terminating continued fraction obtained in this process yields a number of isolated bound states, appropriate for a finite cluster. For most purpose this is an unphysical approximation to the problem under investigation and one needs to overcome these finite size effects by embedding the cluster in an infinite medium. Mathematically a suitable terminator should be appended to the continued fraction so as to obtain a Green function with a branch cut, rather than a set of simple poles. Several terminators are available in the literature which reflects the asymptotic properties of the continued fraction expansion of the Green function accurately. The advantage of such a termination procedure is that the approximate resolvent retains the analytic properties of the Green function, called the Herglotz properties which are as follows :

- All the singularities of $G(z)$ lie on the real z -axis.
- $\Im[G(z)] > 0$ when $\Im(z) < 0$ and $\Im[G(z)] < 0$ when $\Im(z) > 0$.
- $G(z) \rightarrow 1/z$ when $\Re(z) \rightarrow \infty$ along the real axis. Terminator preserves the first $2n$ -moments of the density of states exactly.

In case the coefficients converge, i.e. if $|a_n - a| \leq \epsilon$, $|b_n - b| \leq \epsilon$ for $n \geq N$, we may replace $\{a_n, b_n\}$ by $\{a, b\}$ for all $n \geq N$. In that case the asymptotic part of the continued fraction may be analytically summed to obtain :

$$T(E) = (1/2) \left(E - a - \sqrt{(E - a)^2 - 4b^2} \right)$$

which gives a continuous spectrum $a - 2b \leq E \leq a + 2b$. Since the terminator coefficients are related to the band edges and widths, a sensible criterion for the choice of these asymptotic coefficients is necessary, so as not to give arise to spurious structures in our

calculations. Beer and Pettifor 1984 suggested a sensible criterion : given a finite number of coefficients, we must choose $\{a, b\}$ in such a way so as to give, for this set of coefficients, the minimum bandwidth consistent with no loss of spectral weight from the band. This criterion is easily translated into mathematical terms. The delta functions that would carry weight out of the band must then be situated exactly at the band edges. We thus demand that the continued fraction diverge simultaneously at both the top and the bottom of the band.

At the band edges : $T(a \pm 2b) = \pm b$ so,

$$\ll G(a \pm 2b) \gg = \frac{b_1^2/4}{\pm b - \frac{1}{2}(a_1 - a) - \frac{b_2^2/4}{\pm b - \frac{1}{2}(a_2 - a) - \frac{b_3^2/4}{\dots - \frac{b_N^2/2}{\pm b - (a_N - a)}}}}$$

For a given a , the $(N+1)$ eigenvalues of the finite tridiagonal matrix :

$$\begin{pmatrix} \frac{1}{2}(a_1 - a) & \frac{1}{2}b_2 & 0 & \dots & 0 \\ \frac{1}{2}b_2 & \frac{1}{2}(a_2 - a) & \frac{1}{2}b_3 & \dots & 0 \\ 0 & \frac{1}{2}b_3 & \dots & \dots & 0 \\ \dots & \dots & \dots & \dots & \frac{1}{\sqrt{2}}b_N \\ \dots & \dots & \dots & \frac{1}{\sqrt{2}}b_N & (a_N - a) \end{pmatrix}$$

are values at which the Green function diverges. The maximum and minimum of this set of eigenvalues are those values of b for which spectral weight has just split off from the band. Thus our choice of a is that value for which the maximum eigenvalue is the largest and the minimum the smallest. Since the continued fraction involves b^2 then,

$$b_c = \sup_{\{a\}} b_{max}(a_c) = \inf_{\{a\}} |b_{min}(a_c)|$$

With this choice the terminator $T(E)$ has all the Herglotz properties required. Luchini and Nex 1987 further modified this by replacing the “butt joining” $\{a_n, b_n\}$ to a, b by a smooth linear interpolation :

$$\hat{a}_n, \hat{b}_n = \begin{cases} a_n, b_n & n < n_1 \\ (a_n(N - n) + a(n - n_1))/(N - n_1) & n_1 \leq n \leq N \\ (b_n(N - n) + b(n - n_1))/(N - n_1) & n_1 \leq n \leq N \\ a, b & n > N \end{cases}$$

They argued that most of the possible spurious structures are removed by such interpolation. In our work we have used these two ideas to estimate the terminator.

1.4.2 Block Recursion and the Self Energy Matrix

Although our initial focus during the ongoing work was on the Green function, coherent structure factors, complex dispersion relation and phonon lifetimes (Chapter 4), we also propose to study the inelastic neutron scattering cross section (Chapter 5) and the thermal conductivity (Chapter 6) of disordered alloys. These further studies require the full Green matrices and not only the diagonal elements (as discussed in the previous section). We shall introduce here a generalization of the recursion method of Haydock *et al* 1972. The block recursion technique had been introduced earlier by [Godin and Haydock 1988 , Godin and Haydock 1992] in the very different context for obtaining the scattering S-matrix for finite scatterers attached to perfect leads. We shall borrow their ideas and set up a block recursion in the space of vibrational modes in order to obtain the Green matrices directly.

The recursion method essentially starts from a denumerably infinite basis and changes the basis to one in which the dynamical matrix (or the Hamiltonian, in electronic problems) is tri-diagonal. In the block recursion we start from a matrix basis of the form : $\{\Psi_{J,\alpha\beta}^{(n)}\}$, where J is the discrete labeling of the lattice sites and the α, β labels the Cartesian directions (i.e. the modes of vibration). The inner product of such basis is defined by :

$$\left(\Psi^{(n)}, \Psi^{(m)}\right) = \sum_J \sum_{\beta'} \Psi_{\alpha\beta',J}^{(n)\dagger} \Psi_{J,\beta'\beta}^{(m)} = N_{\alpha\beta}^{nm}$$

We start the recursion with a state $\{\Psi_{J,\alpha\beta}^{(1)}\}$. The remaining terms in the basis are recursively obtained from :

$$\begin{aligned} \sum_{\beta'} \Psi_{J,\alpha\beta'}^{(2)} B_{\beta'\beta}^{(2)\dagger} &= \sum_{J'} \sum_{\beta'} H_{J\alpha,J'\beta'} \Psi_{J',\beta'\beta}^{(1)} - \sum_{\beta'} \Psi_{J,\alpha\beta'}^{(1)} A_{\beta'\beta}^{(1)} \\ \sum_{\beta'} \Psi_{J,\alpha\beta'}^{(n+1)} B_{\beta'\beta}^{(n+1)\dagger} &= \sum_{J'} \sum_{\beta'} H_{J\alpha,J'\beta'} \Psi_{J',\beta'\beta}^{(n)} - \sum_{\beta'} \Psi_{J,\alpha\beta'}^{(n)} A_{\beta'\beta}^{(n)} - \sum_{\beta'} \Psi_{J,\alpha\beta'}^{(n-1)} B_{\beta'\beta}^{(n)} \end{aligned} \quad (1.19)$$

where $\mathbf{H} = \mathbf{M}^{-1/2} \mathbf{D} \mathbf{M}^{-1/2}$ with \mathbf{M} and \mathbf{D} given by Eqns. (1.11).

Orthogonalization of the basis gives :

$$\sum_J \sum_{\beta'} \sum_{J'} \sum_{\beta''} \Psi_{\alpha\beta',J}^{(n)\dagger} H_{J\beta',J'\beta''} \Psi_{J',\beta''\beta'}^{(n)} = \sum_{\beta'} N_{\alpha\beta'}^{nn} A_{\beta'\beta}^{(n)}$$

In matrix notation, where matrices are in the vibrational mode $(\alpha\beta)$ space :

$$\mathbf{A}^{(n)} = \left(\mathbf{N}^{nn} \right)^{-1} \sum_J \sum_{J'} \Psi_J^{(n)\dagger} \mathbf{H}_{JJ'} \Psi_{J'}^{(n)} \quad (1.20)$$

Next, we note that we had started with a orthogonal basis set of rank $J_{max} \times \alpha_{max}$. The above procedure merely gives J_{max} basis sets. We still have orthogonality conditions among the various columns of $\Psi_{J,\alpha\beta}^{(n)}$. In order to impose these conditions, consider

$$\Xi_{J,\alpha\beta} = \sum_{J'} \sum_{\beta'} H_{J\alpha,J'\beta'} \Psi_{J',\beta'\beta}^{(n)} - \sum_{\beta'} \Psi_{J,\alpha\beta'}^{(n)} A_{\beta'\beta}^{(n)} - \sum_{\beta'} \Psi_{J,\alpha\beta'}^{(n-1)} B_{\beta'\beta}^{(n)}$$

Construct three column vectors $\xi_{J\alpha}^{(\beta)}$ out of the three columns of $\Xi_{J,\alpha\beta}$ and set about to Gram-Schmidt orthonormalizing the set :

$$\begin{aligned} \xi_{\alpha J}^{(1)} &= \psi_{\alpha J}^{(1)} B_{11} \Rightarrow B_{11}^2 = \sum_{\alpha J} \xi_{J\alpha}^{(1)*} \xi_{\alpha J}^{(1)} \\ \xi_{\alpha J}^{(2)} &= \psi_{\alpha J}^{(1)} B_{12} + \psi_{\alpha J}^{(2)} B_{22} \Rightarrow B_{12} = \sum_{\alpha J} \psi_{J\alpha}^{(1)*} \xi_{\alpha J}^{(2)} \quad ; \quad B_{22}^2 = \sum_{\alpha J} \xi_{J\alpha}^{(2)*} \xi_{\alpha J}^{(2)} - B_{12}^2 \\ &\dots\dots\dots \\ &\dots\dots\dots \\ \xi_{\alpha J}^{(m)} &= \sum_{k=1}^m \psi_{\alpha J}^{(k)} B_{km} \Rightarrow B_{km} = \sum_{\alpha J} \psi_{J\alpha}^{(k)*} \xi_{\alpha J}^{(m)} \quad (k < m) \quad ; \quad B_{mm}^2 = \sum_{\alpha J} \xi_{J\alpha}^{(m)*} \xi_{\alpha J}^{(m)} - \sum_{k=1}^{m-1} B_{km}^2 \end{aligned} \quad (1.21)$$

where m stands for the total number of vibrational modes.

We may now construct $\Psi_{J,\alpha\beta}^{(n+1)}$ out of $\psi_{J\alpha}^\beta$ and note that B_{km} is indeed the matrix $\mathbf{B}^{(n+1)\dagger}$ we are looking for.

The Eqns.(1.19)-(1.21) show that we may calculate the matrices $\{\mathbf{A}^{(n)}, \mathbf{B}^{(n+1)}\}$ recursively, noting that $\mathbf{B}^{(1)} = \mathbf{I}$ and $\mathbf{B}^{(0)} = \mathbf{0}$. In this new basis, the Hamiltonian is *block tri-diagonal* and the Green matrix can be written as follows :

$$\begin{aligned} \mathbf{G}^{(n)} &= \left[w^2 \mathbf{I} - \mathbf{A}^{(n)} - \mathbf{B}^{(n+1)\dagger} \mathbf{G}^{(n+1)} \mathbf{B}^{(n+1)} \right]^{-1} \\ \ll \mathbf{G} \gg &= \mathbf{G}^{(1)} \end{aligned} \quad (1.22)$$

The terminator which replaces the asymptotic part of the matrix continued fraction is that which is used by Godin and Haydock 1992. We calculate the matrix coefficients up to a $n = N_0$ and approximate at coefficients $> N_0$ by \mathbf{A} and \mathbf{B} . We then write for a $N \gg N_0$:

$$\mathbf{G}^{(N)} = \left[(w^2 - i\delta)\mathbf{I} \right]^{-1}$$

and then iterate :

$$G^{(n)} = \left[w^2\mathbf{I} - \mathbf{A} - \mathbf{B}^\dagger \mathbf{G}^{(n+1)} \mathbf{B} \right]^{-1}$$

for $n > N_0$

A judicious choice of δ (0.001) and N (5000) gives a smooth density of states from the diagonal part of the Green matrix. The self-energy follows from the Dyson equation :

$$\Sigma = \mathbf{g}^{-1} - \mathbf{G}^{-1} \tag{1.23}$$

Chapter 2

Configuration Averaging in Disordered systems

2.1 Introduction

In this chapter we shall introduce the concept of averaging in configuration space and also describe the augmented space method, which is a powerful technique for carrying this out. In subsequent chapters we extend this formalism for application to the problem of phonon excitations in disordered alloys. The concept of averaging over all possible different states of a system is well understood both in quantum mechanics and statistical physics. However for a disordered system, we have to carry out averages for physical observables over different configurations. But the question is, “ Why do we wish to carry out such averages ? ”. The problem will be clearly understood if we analyze a specific example. Suppose an experimentalist is carrying out an energy resolved photo-emission study on a disordered metallic alloy. By varying the energy of his incident photon, he can map out the density of states of valence electrons for the alloy. If he carry out the experiment on ten different samples of the same alloy, he should obtain slightly different results. This is because the alloy is random and different samples will have different atomic arrangements of its constituents. What the experimenter actually observes is an average result ; averaged over different realizable configurations of atomic arrangements in the alloy. The same is true for other bulk properties like specific heat, conductivity and different response functions. However if we measure local properties with local probes, the situation is quite different. Configuration averaging will be meaningless if we wish to look at the local properties.

Another point of interest is “ Why do we observe configuration averaged results even

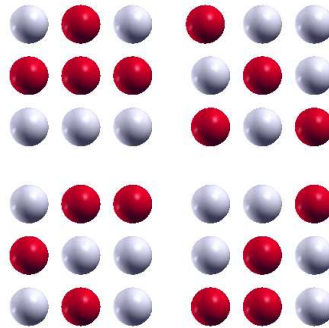


Figure 2.1: Schematic diagram illustrating spatial ergodicity. Each subsystem shown here resembles a configuration when the size diverges. The composition shown here is 45% - 55%

in a single sample ? ” To understand this, we must examine the idea of *spatial ergodicity*. We visualize a macroscopically large system as made up of subsystems each of which resembles a configuration of the system. Spatial ergodicity implies that in the limit of size and the number of subsystems becoming infinitely large, the subsystems of a single sample exactly replicates all its possible configurations. A global property which averages over the subsystems becomes the same as the averages over all configurations. This is schematically shown in Figure 2.1.

2.2 Mean field theories of disorder : an outline

In this section we shall briefly discuss the conventional mean-field theories for configurational averaging. We shall also discuss the limitations of these theories and their probable generalizations. Although it is not our intention to review these, only a brief description will be given and we shall emphasize the merits and demerits of each of these approaches.

Among the various existing theories, we confine ourselves to the crudest approximation, namely the Virtual Crystal Approximation (VCA) and the most successful single-site mean-field approximation : the Coherent Potential Approximation (CPA).

We start from the secular equation for phonons :

$$(\mathbf{M}\omega^2 - \mathbf{D}) \epsilon = 0$$

The Green function $\mathbf{G}(\omega^2)$ corresponding to the displacement vector ϵ is

$$G_{nn}(\omega^2) = \langle n | (\mathbf{M}\omega^2 - \mathbf{D})^{-1} | n \rangle$$

where the mass matrix \mathbf{M} and the dynamical matrix \mathbf{D} in terms of Andersen tight binding representation is given by :

$$\begin{aligned} \mathbf{M} &= \sum_R m_R P_R \delta_{\mu\nu} \\ \mathbf{D} &= \sum_R D_{RR}^{\mu\nu} P_R + \sum_{RR'} D_{RR'}^{\mu\nu} T_{RR'} \end{aligned} \quad (2.1)$$

\mathbf{M} and \mathbf{D} refers to the diagonal and off-diagonal parts of the secular matrix.

In general both the site diagonal and off-diagonal matrix element can be random. The assumption of diagonal randomness is viable in the electronic problem, in cases where the spatial extension of the tight-binding basis of representation is sufficiently small. However off-diagonal disorder is certainly present in the problem of phonons, due to the randomness in the dynamical matrices. When the disorder in diagonal as well as off-diagonal part of the Hamiltonian are of the same order and are correlated (as in the theory of phonons), the problem is difficult to deal with.

2.2.1 The Virtual Crystal Approximation

In the VCA it is assumed that the random variations of m_R and $D_{RR'}$ (in Eq. 2.1) are very small. The simplest possible approximation is to replace m_R and $D_{RR'}$ by their averages $\ll m \gg$ and $\ll D_{RR'} \gg$, so that :

$$\begin{aligned} \mathbf{M}_{eff}^{VCA} &= \sum_R \ll m \gg^\mu P_R \delta_{\mu\nu} \\ \mathbf{D}_{eff}^{VCA} &= \sum_R \ll D_{RR} \gg^{\mu\nu} P_R + \sum_R \sum_{R' \neq R} \ll D_{RR'} \gg^{\mu\nu} T_{RR'} \end{aligned}$$

The effective secular matrix is averaged and does not have any randomness. In this approximation we clearly miss out any scattering caused by the random components of the secular matrix about the average value. This approximation is crude and is nowadays used as the starting point of iterative calculations of more sophisticated mean-field theories.

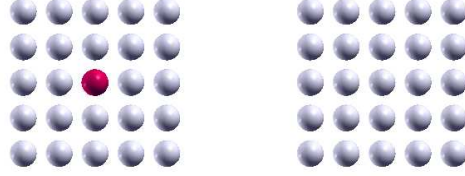


Figure 2.2: A schematic diagram for the self-consistency of the CPA

2.2.2 The Coherent Potential Approximation : its limitations and generalizations

Let us begin from a random secular matrix in which the randomness is in the mass element only. For example, m_R can take the values m_A or m_B and we replace $\mathbf{D}_{RR'}$ by $\ll \mathbf{D}_{RR'} \gg$. In the coherent potential approximation, the basic underlying idea is to obtain an effective secular matrix $\mathbf{S}_{eff}(z)$, which is lattice translationally symmetric and the representation of its Green function $\mathbf{G}^{eff}(z) = \mathbf{S}_{eff}(z)^{-1}$ is a good approximation to the averaged Green function of the random Hamiltonian. $\ll \mathbf{G}(z) \gg = \mathbf{G}^{eff}(z)$

VCA secular matrix also satisfies the lattice translation symmetry property, but is not a very good approximation.

In general such an effective CPA secular matrix $\mathbf{S}_{eff}(z)$ is both complex and frequency dependent and hence not hermitian. We should make sure that the Green function $\mathbf{G}^{eff}(z)$ constructed out of it must satisfy the necessary Herglotz properties. The effective secular matrix may be written in the form :

$$\mathbf{S}_{eff}(z) = \sum_R E(z) P_R + \sum_R \sum_{R' \neq R} \ll \mathbf{D}_{RR'} \gg T_{RR'}$$

$E(z) = \ll \mathbf{m} \gg z^2 - \ll \mathbf{D}_{RR} \gg + \Sigma(z)$, the correction to the VCA i.e. $\Sigma(z)$ is called the self energy.

The self-energy is found by the following argument : Let us consider a system in which we replace the secular matrix at every site by the effective secular matrix, but keep the

exact random diagonal part of the secular matrix at any one site (see Fig. 2.2). We can calculate the Green function at that site for this *single impurity* system (average of the left figure in Fig. 2.2). The average of this Green function over that one site should be the configuration averaged Green function (right figure in Fig. 2.2) :

$$\ll G_{RR}^{(R)}(\omega^2) \gg_{(R)} = G_{RR}^{eff}(\omega^2) = \ll G_{RR}(\omega^2) \gg$$

This is an implicit equation for the self-energy, which occurs on both sides.

This MCPA (i.e. mass CPA in case of the phonon problem) works well when mass difference of two components of a binary alloy is small and it becomes inadequate when $\delta = |\Delta M| \omega^2 / |Z \Phi|$ is large ($Z =$ co-ordination number for the concerned lattice ; $\Phi =$ average force constant). It is clear from the above formulation of the CPA, that it can explicitly deal with the disorder in one site only. It cannot take into account the configuration fluctuation effects due to two or more sites. Nor can it properly take into account off-diagonal disorder. We list the following limitations of CPA :

- CPA can not correctly deal with the off-diagonal disorder (i.e. the randomness in the force constant matrices involving two or more sites).
- Short range ordering effect due to chemical clustering or segregation cannot be taken into account.
- The effect of random (or statistical) clustering which is particularly important in impurity bands is totally absent.
- Experimentally, it has been found that the local modes show some fine structures which are lost in MCPA.
- The MCPA fails to give correct band widths.

These limitations of the CPA point toward a need to generalize the single site CPA.

Throughout the seventies of the last century there have been various suggestions of ways of generalizing the CPA to take into account the effect of random clustering, off-diagonal disorder and short range ordering effects for the multi-site scattering. As far

as off-diagonal disorder is concerned, several authors have proposed schemes for generalizing the CPA and their approaches include geometrically scaled off-diagonal disorder, linearly scaled off-diagonal disorder and independent diagonal and off-diagonal disorder. Majority of these approaches suffer from the different kinds of drawbacks : first there is no reason why the off-diagonal part of the dynamical matrix should scale either as the geometrical mean or the arithmetic mean of the individual constituents dynamical matrix. Secondly, in most cases the proposed generalization violates translation symmetry of the configuration averaged quantities for homogeneous disorder. Finally, and most seriously, the approximate configuration averaged Green functions violate the essential Herglotz analytic properties required to produce physically acceptable results.

In all the previous approaches, the dynamical behaviour of the system was described by a secular matrix (or Hamiltonian, in case of electrons), suitably set up, whereas the statistical behaviour was imposed, as it were, from outside by allowing the secular matrix elements to vary randomly according to some prescription. The secular matrix, by itself, does not describe the full statistical behaviour of the system completely. If we were to augment the secular matrix to include the information about the statistical distribution of its random elements, we would possibly have in our hands an easier tool to describe configuration averages. The Augmented space formalism of Mookerjee 1973 does exactly this and has proved to be one of the powerful techniques in this area. We shall describe this method in some detail in the next section.

2.3 The Augmented Space Formalism

2.3.1 The Configuration Space

We shall begin by clarifying the mathematical concept of the configuration space of a set of random variables. The idea of a space of configurations is quite familiar to those working with the Ising model, for instance. This model consists of a set of *spins* $\{\sigma_R\}$ arranged on a discrete lattice labelled by $\{R\}$. Each spins can have two possible states or *configurations* : $|\uparrow_R\rangle$ and $|\downarrow_R\rangle$. The collection of all linear combinations of these two states i.e. $\{a|\uparrow_R\rangle + b|\downarrow_R\rangle\}$ is called the configuration space of $\{\sigma_R\}$. It is of rank 2 and is spanned by the states $\{|\uparrow_R\rangle, |\downarrow_R\rangle\}$. Let us call this space ϕ_R .

The set of N-spins then have 2^N possible configurations, each of which can be written as a sequence of m-up states and (N-m) down-states. The number (N-m) is defined as the *cardinality* of the configuration and the sequence $\{C\}$ of sites $\{R_{i1}, R_{i2}, R_{i3}, \dots, R_{i_{N_m}}\}$ where the down states sit is called the *cardinality sequence* of configuration. For example take a particular configuration of 6-spins $\{\uparrow_1 \downarrow_2 \uparrow_3 \downarrow_4 \downarrow_5 \downarrow_6\}$. It has a cardinality 4 and a cardinality sequence $\{2 \ 4 \ 5 \ 6\}$. Another configuration $\{\downarrow_1 \uparrow_2 \uparrow_3 \downarrow_4 \downarrow_5 \downarrow_6\}$ also has cardinality 4 but its cardinality sequence is $\{1 \ 4 \ 5 \ 6\}$ which is distinct from the previous one. For a set of N-spins, the configuration space Φ is of rank 2^N and can be written as the direct product of the configuration spaces of individual spins

$$\Phi = \prod_R^{\otimes} \phi_R$$

For spins having $n > 2$ numbers of realizations, It is quite straight forward to generalize these ideas. The configuration of an individual spin can be labelled as $|\kappa_R\rangle$ where $\kappa_R = 1, 2, \dots, n$. The rank of ϕ_R is now n. Also the set of N-spins will have n^N possible configurations.

We can now translate our ideas from spins $\{\sigma_R\}$ to the random occupation variables $\{n_R\}$ for a tight binding model of a binary alloy. The occupation variables associated with a site take the values 0 and 1 when the site is occupied by an atom of the A or B types. We can immediately visualize the configuration space of the Hamiltonian variable. Whenever a set of random variables $\{n_R\}$ have a binary distribution, their configuration space is isomorphic to the one for a collection of Ising spins.

We may now set up the secular matrix for the vibrational problem in a substitutional binary alloy in terms of the occupation variables :

$$\mathbf{S}(\omega^2) = \mathbf{M} \omega^2 - \mathbf{D}_0 - \mathbf{D}_1$$

with

$$\begin{aligned} \mathbf{M} &= \sum_R \{m_A n_R + m_B (1 - n_R)\} \delta_{\mu\nu} P_R \\ \mathbf{D}_0 &= - \sum_R \mathbf{D}'_R P_R \\ \mathbf{D}_1 &= \sum_R \mathbf{D}'_R T_{RR'} \end{aligned} \quad (2.2)$$

and

$$\mathbf{D}'_R = \sum_{R'} \left\{ D_{AA}^{\mu\nu} n_R n_{R'} + D_{AB}^{\mu\nu} [n_R(1 - n_{R'}) + n_{R'}(1 - n_R)] + D_{BB}^{\mu\nu} (1 - n_R)(1 - n_{R'}) \right\}$$

Let us assume that these variables $\{n_R\}$ are independently distributed with the probability density $p_R\{n_R\}$ [for the individual variables]. The total probability density is given by :

$$P(\{n_R\}) = \prod_{R=1}^N p_R(n_R)$$

Probability density $p_R(n_R)$ satisfies the properties

- It is positive definite $p_R(n_R) \geq 0$
- We shall assume that *all* its moments are finite. This is a reasonable assumption for almost all physical distributions. $\int_{-\infty}^{\infty} n_R^k p_R(n_R) dn_R < \infty \quad k > 0$

The above properties are specific to the imaginary part of a Herglotz function. For example, the imaginary part of the Green function of a self adjoint operator H (i.e. local density of states). One should note that : the local density of states is positive definite and all its moments are finite if H is a bounded operator.

Taking clue from this, Mookerjee 1973 suggested that for a binary distribution a Hilbert space ϕ_R of rank two spanned by a basis $|\uparrow_R\rangle, |\downarrow_R\rangle$ may be introduced such that $p_R(n_R)$ corresponds to the imaginary part of the resolvent of a suitably chosen operator \mathbf{N}^R in ϕ_R .

$$\text{i.e. } p_R(n_R) = -\frac{1}{\pi} \Im m \left[\langle \uparrow_R | (z\mathbf{I} - \mathbf{N}^R)^{-1} | \uparrow_R \rangle \right] \quad (2.3)$$

where $z \rightarrow n_R + i \delta ; \delta \rightarrow 0$

Since the resolvent $\langle \uparrow_R | (z\mathbf{I} - \mathbf{N}^R)^{-1} | \uparrow_R \rangle$ is Herglotz, so it can be expanded in a convergent continued fractional form,

$$p_i(n_i) = -\frac{1}{\pi} \Im m \frac{1}{z - a_0 - \frac{b_1^2}{z - a_1}} \quad (2.4)$$

For a binary distribution $p_R(n_R) = x_A \delta(n_R - 1) + x_B \delta(n_R)$ we have : $a_0 = x_A, a_1 = x_B$ and $b_1 = \sqrt{x_A x_B}$.

If n_R takes k different values, then the configuration space is spanned by k states : $|k\rangle$ which are the eigenstates of N_R with eigenvalue k . In that case the *average state* $|\emptyset_R\rangle$, which is the equivalent of $|\uparrow_R\rangle$ is $\sum_k \sqrt{x_k} |k\rangle$ where x_k is the probability of the variable N_R to take the value k . The other members of the countable basis $|n\rangle$ may be obtained recursively from the average state through :

$$\begin{aligned} |0\rangle &= |\emptyset_R\rangle \\ b_1|1\rangle &= \mathbf{N}^R |0\rangle - a_0|0\rangle \\ \dots & \quad \dots \quad \dots \quad \dots \\ b_n|n\rangle &= \mathbf{N}^R |n-1\rangle - a_{n-1}|n-1\rangle - b_{n-1}|n-2\rangle \end{aligned}$$

In this basis, the operator \mathbf{N}^R thus has the tridiagonal form,

$$\begin{pmatrix} a_0 & b_1 & 0 & 0 & 0 & \dots \\ b_1 & a_1 & b_2 & 0 & 0 & \dots \\ 0 & b_2 & a_2 & b_3 & 0 & \dots \\ 0 & 0 & b_3 & a_3 & b_4 & \dots \\ \dots & \dots & \dots & \dots & \dots & \dots \end{pmatrix}$$

The close relation of the above procedure to the recursion method described in the previous chapter should be noted. This is not surprising, since the projected density of states and the probability density are both positive definite and integrable functions. Convergence of the continued fraction further requires finite moments to all orders in both the cases.

2.3.2 Augmented Space Theorem

We now address the problem of configuration average of physical quantities. The augmented space theorem, proposed by Mookerjee 1973, states that :

“ To each variable n_R there is associated a *configuration space* ϕ_R spanned by the *states* $\{|k\rangle\}$ of realizations of n_R and a self adjoint operator N^R , such that

$$p_R(n_R) = -\frac{1}{\pi} \Im m \langle \emptyset_R | [(n_R + i\delta)\mathbf{I} - \mathbf{N}^R]^{-1} | \emptyset_R \rangle$$

Then the average of any physical property which is a function of the set of random variables $\{n_R\}$ is

$$\ll A(\{n_R\}) \gg = \langle \emptyset | \widetilde{\mathbf{A}}(\{\mathbf{N}^R\}) | \emptyset \rangle \quad (2.5)$$

where $\widetilde{\mathbf{A}}(\{\mathbf{N}^R\})$ is an operator which is the same functional of $\{\mathbf{N}^R\}$ as $A(\{n_R\})$ is of n_R . Further, $|\emptyset\rangle = \prod_R^\otimes |\emptyset_R\rangle$ is the *average configuration state* in the product space $\Phi = \prod_R^\otimes \phi_R$. The product space Φ contains information about all possible configurations of the disordered system. ”

Let us look at the proof of the theorem for a function of single random variable n_R . The generalization for a function of the set of many random variables is quite straight forward. Let $f(n_R)$ be a function of a random variable n_R . Now,

$$\begin{aligned} \ll f(n_R) \gg &= \int_{-\infty}^{\infty} f(n_R) p_R(n_R) dn_R \\ &= -\frac{1}{\pi} \Im m \int_{-\infty}^{\infty} f(n_R) \langle \emptyset_R | (n_R I - \mathbf{N}^R)^{-1} | \emptyset_R \rangle dn_R \\ &= -\frac{1}{\pi} \Im m \sum_k \sum_{k'} \int_{-\infty}^{\infty} f(n_R) \langle \emptyset_R | k \rangle \langle k | (n_R I - \mathbf{N}^R)^{-1} | k' \rangle \langle k' | \emptyset_R \rangle dn_R \\ &= \sum_k \langle \emptyset_R | k \rangle f(k) \langle k | \emptyset_R \rangle = \langle \emptyset_R | \tilde{\mathbf{f}}(\mathbf{N}^R) | \emptyset_R \rangle \end{aligned} \quad (2.6)$$

Here $\tilde{\mathbf{f}}(\mathbf{N}^R)$ is an operator built out of $f(n_R)$ by simply replacing the variable n_R by the associated operator \mathbf{N}^R . The above expression shows that the average is obtained by taking the matrix element of this operator between the *average state* $|\emptyset_R\rangle$.

Since we have applied the theorem to a single variable alone, the power of the above theorem is not apparent. Let us now generalize the theorem to a function of many independent random variables $\{n_R\}$. The joint probability distribution is given by :

$$P(n_{R_1}, n_{R_2}, \dots, n_{R_i} \dots) = \prod_i p_i(n_{R_i})$$

The generalization of the above theorem to averages of functions of the set of random variables is straight forward.

$$\ll f(\{n_R\}) \gg = \langle \emptyset | \tilde{\mathbf{f}}(\{\widetilde{\mathbf{N}}^R\}) | \emptyset \rangle$$

All the operators in the full configuration space Φ will be denoted by tilde variables. The operator $\widetilde{\mathbf{N}}^R$ are built up from the operators \mathbf{N}^R as :

$$\widetilde{\mathbf{N}}^R = \mathbf{I} \otimes \mathbf{I} \otimes \dots \otimes \mathbf{N}^R \otimes \mathbf{I} \otimes \dots$$

This is the augmented space theorem.

If we wish to carry out the configuration averaging of the phonon Green function matrix element given by the following expression :

$$G_{RR}(\omega^2, \{n_R\}) = \langle R | \left(\mathbf{M}(\{n_R\})\omega^2 - \mathbf{D}(\{n_R\}) \right)^{-1} | R \rangle$$

The theorem leads to

$$\ll G_{RR}(\omega^2) \gg = \langle R \otimes \{\emptyset\} | \left(\widetilde{\mathbf{M}}(\{\widetilde{\mathbf{N}}^R\})\omega^2 - \widetilde{\mathbf{D}}(\{\widetilde{\mathbf{N}}^R\}) \right)^{-1} | R \otimes \{\emptyset\} \rangle \quad (2.7)$$

where $\widetilde{\mathbf{M}}(\{\widetilde{\mathbf{N}}^R\})$ is an operator having a functional form same as that of $\mathbf{M}(\{n_R\})$. $\widetilde{\mathbf{D}}(\{\widetilde{\mathbf{N}}^R\})$ is also an operator having the same functional form as that of $\mathbf{D}(\{n_R\})$. The operators in the right hand side of Eqn. (2.7) have no randomness and hence can be evaluated rather easily.

The power of the theorem now becomes apparent. The average is seen to be a particular matrix element of the Green function of an augmented Secular matrix operator. This is an operator in the augmented space $\Psi = \mathcal{H} \otimes \Phi$ where \mathcal{H} is the space spanned by the tight binding basis and Φ the full configuration space. The result is *exact*. Approximations can now be introduced in the actual calculation of this matrix element in a controlled manner. In particular we shall show that the recursion method described in the earlier chapter is ideally suited for obtaining matrix elements with greater accuracy. Since configuration averaging is an intrinsically difficult problem, we must pay the price for the above simplifications. This comes in the shape of the enormous rank of the augmented space. For sometime it was thought that recursion on the full augmented space was not a feasible proposition. However it can be shown that, if randomness is homogeneous in the sense that $p(n_R)$ is independent of the label R , then the augmented space has a large number of local point group and lattice translational symmetries. Saha *et al* 2004 utilized these symmetry and vastly reduce the rank of the effective space on which the recursion is carried out. This made augmented space recursion a viable technique and a body of work has been done based on the method [Mookerjee 2003].

Chapter 3

Behavior of phonon excitations in random binary alloys

3.1 Introduction

Many aspects of lattice vibrational, magnetic and electronic excitations in disordered alloys have been intensively studied both theoretically and experimentally over the past few decades. Of them the, the electronic problem has been covered in most detail in recent times with the emergence of first principles techniques which have made it possible for the theories to attain a much higher degree of accuracy and reliability. Among these excitations, phonons are not only conceptually the simplest, but are also the most readily accessible to experimental verification. Neutron scattering experiments [Kamitakahara and Brockhouse, 1974, Tsunoda *et al* 1979, R. M. Nicklow 1983] have provided detailed information about lattice vibrations in random alloys. A satisfactory reliable theory is still lacking. The main reason for this is that, unlike the case of electrons in substitutionally disordered alloys, where the Hamiltonian can be expressed in a form where the disorder is *diagonal* in a real space representation (This is certainly true, for example, in a LMTO formalism in the absence of local lattice distortions), the disorder in the dynamical matrix is essentially *off-diagonal*. To make things more complicated, the diagonal and off-diagonal

⁰The contents of this chapter has been published in two papers :

1. Aftab Alam and A Mookerjee, *Phys. Rev. B* **69**, 024205(2004)
2. Aftab Alam and A Mookerjee, Proceedings of the DAE solid state physics symposium, Vol. **49**, 590-591 (2004)

disorders in the dynamical matrix are coupled by the force constant sum rule $\Phi_{RR} = -\sum_{R' \neq R} \Phi_{RR'}$, which ensures that no vibration can be excited in a uniform translation of the crystal as a whole. This sum rule imposes an *environmental disorder* on the force constants. That is, the disorder in the diagonal element of the dynamical matrix depends upon its near neighbours or its immediate environment. Hence a reliable theory for phonon excitations will be that which includes all the three kinds of disorders explicitly.

From the late 1960's there were many attempts to provide an adequate theory of phonons in random alloys. Let us look at the most successful mean field approximation : the single-site coherent potential approximation (CPA), introduced first by Taylor 1967. As the name itself suggests, it is a single site approximation and per se cannot deal adequately with off-diagonal disorder. Several authors have proposed schemes for generalizing the CPA and their approaches include geometrically scaled off-diagonal disorder [H. Shiba 1968, Grunewald 1976], linearly scaled off-diagonal disorder [Kaplan and Mostoller 1974] and independent diagonal and off-diagonal disorder [Kaplan and Mostoller 1974, Kaplan and Gray 1981, Mills and Ratnavaraksha 1978, Kaplan *et al* 1980]. Most of these schemes in practice lead to a single site CPA including off-diagonal disorder. These approaches suffer from two different kinds of drawbacks : first, there is no reason why the off-diagonal part of the dynamical matrix should scale either as the geometric mean or the arithmetic mean of the constituents. Secondly, often the extra assumptions lead to approximate Green functions which violate the essential Herglotz analytic properties required to produce physically acceptable results.

The augmented space approach suggested by Mookerjee 1973 provided a very interesting starting point for the generation of appropriate approximations. The 2-site CPA proposed by Yussouff and Mookerjee 1984 for model systems and subsequently generalized [Mookerjee and Singh 1985, Mookerjee and Singh 1988] to realistic alloys was one successful approach. While it retained the Herglotz properties of the approximate Green functions, the generalization of the 2CPA to larger clusters violated the lattice translational symmetry of the *configurationally averaged* Green function for homogeneous disorder. This was overcome subsequently by the traveling cluster approximation of Kaplan and Gray 1981 also based on the augmented space method. Recently Ghosh *et al* 2002 have proposed a nearest neighbour traveling cluster CPA and have applied it to phonons

in NiPt and NiPd alloys. In the next section we shall propose a different approximation procedure. We shall start from the augmented space method and use the recursion method of Haydock *et al* 1972 to obtain the configurationally averaged Green functions. The termination of the continued fraction expansion will constitute the approximation. This will not only retain the Herglotz analytic properties of the approximate averaged Green function, but also include the effect at a site of its neighbourhood, the size of which we can control. We shall incorporate the effect of the very distant environment by the use of accurate *termination schemes* proposed e.g. by Haydock 1980, Luchini and Nex 1987 or Beer and Pettifor 1984. Since we shall incorporate the lattice translation symmetry in the full augmented space (which is characteristic of homogeneous disorder Ghosh *et al* 1997) within our approach, the drawback of the original cluster-CPAs used by Mookerjee and Singh 1985 and Mookerjee and Singh 1988 will be overcome. Further, we shall use the local point group symmetries of the lattice and the configurations on it to drastically reduce the rank of the Hilbert space on which the recursion takes place (see Dasgupta *et al* 1996). This will allow us to accurately account for large environments around a particular site. One of the strengths of the proposed method which will represent a major step forward in the theory is the possibility of including random fluctuations in force constants beyond the nearest neighbours. While in certain representations the Hamiltonian of electronic systems can be seen to be short-ranged, this is not so for dynamical matrices. The recursion method in augmented space can include beyond nearest neighbour randomness in force constants without much computational expense. In our work on NiPt and NiPd we have extended disorder up to second nearest neighbours to illustrate this. It is not immediately clear how easy it would be to extend the method proposed by Ghosh *et al* 1997 to larger sized clusters. We propose the ASR as a computationally fast and accurate technique which will incorporate configuration fluctuations over a large local environment.

3.2 The augmented space formalism for phonons

The basic problem in the theory of phonons is to solve a secular equation of the form :

$$(\mathbf{M}\omega^2 - \mathbf{D}) \mathbf{u}(R, \omega) = 0$$

where $u_\alpha(R, \omega)$ is the Fourier transform of $u_\alpha(R, t)$, the displacement of an atom from its equilibrium position R on the lattice, in the direction α at time t . \mathbf{M} is the *mass operator*, diagonal in real space and \mathbf{D} is the *dynamical matrix operator* whose tight-binding representation is of the form :

$$\mathbf{M} = \sum_R m_R \delta_{\alpha\beta} P_R, \quad (3.1)$$

$$\mathbf{D} = \sum_R \Phi_{RR}^{\alpha\beta} P_R + \sum_R \sum_{R' \neq R} \Phi_{RR'}^{\alpha\beta} T_{RR'} \quad (3.2)$$

along with the *sum rule*:

$$\Phi_{RR}^{\alpha\beta} = - \sum_{R' \neq R} \Phi_{RR'}^{\alpha\beta} \quad (3.3)$$

Here P_R is the projection operator $|R\rangle\langle R|$ and $T_{RR'}$ is the transfer operator $|R\rangle\langle R'|$ in the Hilbert space \mathcal{H} spanned by the tight-binding basis $\{|R\rangle\}$. R, R' specify the lattice sites and α, β the Cartesian directions. m_R is the mass of an atom occupying the position R and $\Phi_{RR'}^{\alpha\beta}$ is the force constant tensor.

We shall be interested in calculating the displacement-displacement Green function in the frequency-wavevector space, which in the absence of disorder in the system has the diagonal element

$$G(\mathbf{k}, \mathbf{k}', \omega^2) = G(\mathbf{k}, \omega^2) \delta(\mathbf{k} - \mathbf{k}').$$

and for the present case

$$G(\mathbf{k}, \omega^2) = \langle \mathbf{k} | (\mathbf{M}\omega^2 - \mathbf{D})^{-1} | \mathbf{k} \rangle$$

where $|\mathbf{k}\rangle$ is a state in the reciprocal space given by :

$$|\mathbf{k}\rangle = \frac{1}{\sqrt{N}} \sum_R \exp(-i\mathbf{k}\cdot\mathbf{R}) |R\rangle.$$

Since the mass matrix \mathbf{M} is perfectly diagonal, we can write

$$G(\mathbf{k}, \omega^2) = \langle \mathbf{k} | \mathbf{M}^{-1/2} (\omega^2 I - \mathbf{M}^{-1/2} \mathbf{D} \mathbf{M}^{-1/2})^{-1} \mathbf{M}^{-1/2} | \mathbf{k} \rangle \quad (3.4)$$

where

$$\mathbf{M}^{-1/2} = \sum_R m_R^{-1/2} \delta_{\alpha\beta} P_R.$$

The equation (3.4) looks exactly like the Green function for the electronic case with $\mathbf{M}^{-1/2}\mathbf{D}\mathbf{M}^{-1/2}$ playing the role of Hamiltonian \mathbf{H} , ω^2 in place of energy and $\mathbf{M}^{-1/2}|\mathbf{k}\rangle$ is the starting state of recursion.

Let us now consider a binary alloy A_xB_y consisting of two kinds of atoms A and B of masses m_A and m_B randomly occupying each lattice sites. We wish to calculate the configuration-averaged Green function $\ll G(\mathbf{k}, \omega^2) \gg$. We shall use the augmented space formalism (ASF) to do so. Since the disorder is homogeneous, averaged $\ll G(\mathbf{k}, \omega^2) \gg$ is also diagonal in reciprocal space representation [Ghosh *et al* 1997]. The first operation is to represent the random parts of the secular equation in terms of a random set of local variables $\{n_R\}$ which are 1 if the site R is occupied by an A atom and 0 if it is occupied by B. The probability densities of these variables may be written as :

$$\begin{aligned} p(n_R) &= x \delta(n_R - 1) + y \delta(n_R) \\ &= (-1/\pi) \Im m \langle \uparrow_R | (n_R \mathbf{I} - \mathbf{N}_R)^{-1} | \uparrow_R \rangle \end{aligned} \quad (3.5)$$

where x and y are the concentrations of the constituents A and B with $x + y = 1$. \mathbf{N}_R is an operator defined on the configuration space ϕ_R of the variable n_R . This is of rank 2 and is spanned by the states $\{|\uparrow_R\rangle, |\downarrow_R\rangle\}$:

$$\mathbf{N}^R = x \mathbf{p}_R^\uparrow + y \mathbf{p}_R^\downarrow + \sqrt{xy} \mathbf{T}_R^{\uparrow\downarrow}$$

where $\mathbf{p}_R^\uparrow = |\uparrow_R\rangle\langle\uparrow_R|$ is a projection operator on the average state at R and $\mathbf{T}_R^{\uparrow\downarrow} = |\uparrow_R\rangle\langle\downarrow_R| + |\downarrow_R\rangle\langle\uparrow_R|$ is a transfer or *spin flip* operator in configuration space.

Let us now carry out the ASF operations in some detail : The mass m_R of the atom sitting at the site R can then be expressed as :

$$m_R^{-1/2} = m_A^{-1/2} n_R + m_B^{-1/2} (1 - n_R) = m_B^{-1/2} + (\delta m)^{-1/2} n_R$$

where

$$(\delta m)^{-1/2} = m_A^{-1/2} - m_B^{-1/2}.$$

Therefore

$$\mathbf{M}^{-1/2} = \sum_R \left[m_B^{-1/2} + n_R (\delta m)^{-1/2} \right] \delta_{\alpha\beta} \mathbf{P}_R. \quad (3.6)$$

In the augmented space formalism, in order to obtain the configuration average we simply replace the random variables n_R by the corresponding operator \mathbf{N}^R associated with its probability density (as in equation 3.5) and take the matrix element of the resulting operator between the *reference states*.

Using the form of \mathbf{N}^R in Eq. (3.6), we get

$$\widetilde{\mathbf{M}}^{-1/2} = m_1^{-1/2} \mathbf{I} \otimes \mathbf{I} + m_2^{-1/2} \sum_R \mathbf{p}_R^\downarrow \otimes \mathbf{P}_R + m_3^{-1/2} \sum_R \mathbf{T}_R^{\uparrow\downarrow} \otimes \mathbf{P}_R \quad (3.7)$$

where

$$\left. \begin{aligned} m_1^{-1/2} &= x m_A^{-1/2} + y m_B^{-1/2} \\ m_2^{-1/2} &= (y - x) (\delta m)^{-1/2} \\ m_3^{-1/2} &= \sqrt{xy} (\delta m)^{-1/2}. \end{aligned} \right\}$$

Similarly the random off-diagonal force constants $\Phi_{RR'}^{\alpha\beta}$ between the sites R and R' can be written as :

$$\begin{aligned} \Phi_{RR'}^{\alpha\beta} &= \Phi_{AA}^{\alpha\beta} n_R n_{R'} + \Phi_{BB}^{\alpha\beta} (1 - n_R)(1 - n_{R'}) + \Phi_{AB}^{\alpha\beta} [n_R(1 - n_{R'}) + n_{R'}(1 - n_R)] \\ \Phi_{RR'}^{\alpha\beta} &= \Phi_{BB}^{\alpha\beta} + (\Phi_{AA}^{\alpha\beta} + \Phi_{BB}^{\alpha\beta} - 2\Phi_{AB}^{\alpha\beta}) n_R n_{R'} + (\Phi_{AB}^{\alpha\beta} - \Phi_{BB}^{\alpha\beta}) (n_R + n_{R'}). \end{aligned}$$

Let us define the following :

$$\begin{aligned} \Phi_{(1)}^{\alpha\beta} &= x \Phi_{AA}^{\alpha\beta} - y \Phi_{BB}^{\alpha\beta} + (y - x) \Phi_{AB}^{\alpha\beta} \\ \Phi_{(2)}^{\alpha\beta} &= \Phi_{AA}^{\alpha\beta} + \Phi_{BB}^{\alpha\beta} - 2\Phi_{AB}^{\alpha\beta}. \end{aligned}$$

In augmented space the off-diagonal force constant matrix becomes an operator :

$$\begin{aligned} \widetilde{\Phi}_{off}^{\alpha\beta} &= \sum_{RR'} \left[\ll \Phi_{RR'}^{\alpha\beta} \gg \mathbf{I} + \Phi_{(1)}^{\alpha\beta} \left\{ (y - x) (\mathbf{p}_R^\downarrow + \mathbf{p}_{R'}^\downarrow) + \sqrt{xy} \mathbf{T}_R^{\uparrow\downarrow} \right\} + \right. \\ &\quad \left. \Phi_{(2)}^{\alpha\beta} \left\{ (y - x)^2 \mathbf{p}_R^\downarrow \mathbf{p}_{R'}^\downarrow + \sqrt{xy} (y - x) (\mathbf{p}_R^\downarrow \mathbf{T}_{R'}^{\uparrow\downarrow} + \mathbf{p}_{R'}^\downarrow \mathbf{T}_R^{\uparrow\downarrow}) + xy \mathbf{T}_R^{\uparrow\downarrow} \mathbf{T}_{R'}^{\uparrow\downarrow} \right\} \right] \otimes \mathbf{T}_{RR'} \\ &= \sum_{RR'} \Psi_{RR'}^{\alpha\beta} \otimes \mathbf{T}_{RR'}. \end{aligned} \quad (3.8)$$

The sum rule,

$$\Phi_{RR}^{\alpha\beta} = - \sum_{R' \neq R} \Phi_{RR'}^{\alpha\beta}$$

gives the diagonal element of the dynamical matrix :

$$\widetilde{\Phi}_{dia}^{\alpha\beta} = - \sum_R \left\{ \sum_{R' \neq R} \Psi_{RR'}^{\alpha\beta} \right\} \otimes \mathbf{P}_R. \quad (3.9)$$

The total dynamical matrix in the augmented space is :

$$\widetilde{\mathbf{D}} = - \sum_R \left\{ \sum_{R' \neq R} \Psi_{RR'}^{\alpha\beta} \right\} \otimes \mathbf{P}_R + \sum_{RR'} \Psi_{RR'}^{\alpha\beta} \otimes \mathbf{T}_{RR'}. \quad (3.10)$$

The augmented space theorem [Mookerjee 1973] now states that the configuration averaged Green function $\ll G(\mathbf{k}, w^2) \gg$ may be written as :

$$\begin{aligned} \ll G(\mathbf{k}, \omega^2) \gg &= \int G(\mathbf{k}, \omega^2, \{n_R\}) \prod p(n_R) dn_R \\ &= \langle \mathbf{k} \otimes \{\emptyset\} | \widetilde{\mathbf{G}}(\mathbf{k}, \omega^2, \{\mathbf{N}_R\}) | \mathbf{k} \otimes \{\emptyset\} \rangle \\ &= \langle \mathbf{k} \otimes \{\emptyset\} | \widetilde{\mathbf{M}}^{-1/2} (\omega^2 \widetilde{I} - \widetilde{\mathbf{M}}^{-1/2} \widetilde{\mathbf{D}} \widetilde{\mathbf{M}}^{-1/2})^{-1} \widetilde{\mathbf{M}}^{-1/2} | \mathbf{k} \otimes \{\emptyset\} \rangle \end{aligned} \quad (3.11)$$

where $\widetilde{\mathbf{M}}^{-1/2}$ and $\widetilde{\mathbf{D}}$ are the operators which are constructed out of $\mathbf{M}^{-1/2}$ and \mathbf{D} by replacing all the random variables n_R (or $n_{R'}$) by the corresponding operators N^R (or $N^{R'}$) as given by equation (3.7) and (3.10). These are the operators in the augmented space $\Omega = \mathcal{H} \otimes \Phi$. The state $|\mathbf{k} \otimes \{\emptyset\}\rangle$ is actually an augmented space state which is the direct product of the Hilbert space basis and the configuration space basis. The average configuration $\{\emptyset\}$ refers to a null cardinality sequence i.e. one in which we have $|\uparrow\rangle$ at all sites.

Using the operator representation for $\widetilde{\mathbf{M}}^{-1/2}$ we get :

$$\widetilde{\mathbf{M}}^{-1/2} |\mathbf{k} \otimes \{\emptyset\}\rangle = m_1^{-1/2} \|\{\emptyset\}\rangle + m_3^{-1/2} \|\{R\}\rangle = |1\rangle$$

where a configuration state is denoted by its *cardinality sequence* $\{C\}$. We have also used the short hand notation :

$$\|\{C\}\rangle \equiv \frac{1}{\sqrt{N}} \sum_R \exp(-i \mathbf{k} \cdot R) |R \otimes \{C\}\rangle.$$

The ket $|1\rangle$ is not normalized. A normalized ket $|1\rangle$ is given by

$$|1\rangle = \frac{|1\rangle}{\sqrt{\{1|1\}}} = \left(\frac{m_1}{\widehat{m}}\right)^{-1/2} \|\{\emptyset\}\rangle + \left(\frac{m_3}{\widehat{m}}\right)^{-1/2} \|\{R\}\rangle$$

With the definitions :

$$\ll (1/m) \gg^{-1} = \widehat{m}$$

$$\tilde{\mathbf{J}} = \left(\frac{m_1}{\widehat{m}}\right)^{-1/2} \mathbf{I} \otimes \mathbf{I} + \left(\frac{m_2}{\widehat{m}}\right)^{-1/2} \sum_R \mathbf{P}_R \otimes \mathbf{p}_R^\dagger + \left(\frac{m_3}{\widehat{m}}\right)^{-1/2} \sum_R \mathbf{P}_R \otimes \mathbf{T}_R^{\dagger\downarrow}$$

we may rewrite equation (3.11) as :

$$\ll G(\mathbf{k}, \omega^2) \gg = \langle 1 | (\omega'^2 \tilde{\mathbf{I}} - \widetilde{\mathbf{D}}_{eff})^{-1} | 1 \rangle \quad (3.12)$$

where, $\omega'^2 = \widehat{m}\omega^2$ and $\widetilde{\mathbf{D}}_{eff} = \tilde{\mathbf{J}} \widetilde{\mathbf{D}} \tilde{\mathbf{J}}$. This equation is now exactly in the form in which recursion method may be applied. At this point we note that the above expression for the averaged $\ll G(\mathbf{k}, \omega'^2) \gg$ is exact. The recursion transforms the basis through a three term recurrence relation as :

$$\begin{aligned} |\phi_1\rangle &= |1\rangle \quad ; \quad |\phi_0\rangle = 0 \\ |\phi_{n+1}\rangle &= \widetilde{\mathbf{D}}_{eff} |\phi_n\rangle - a_n |\phi_n\rangle - b_n^2 |\phi_{n-1}\rangle \end{aligned} \quad (3.13)$$

The averaged Green's function can then be written as a continued fraction :

$$\ll G(\mathbf{k}, \omega^2) \gg = \frac{b_1^2}{\omega'^2 - a_1 - \frac{b_2^2}{\omega'^2 - a_2 - \frac{b_3^2}{\omega'^2 - a_3 - \dots - \frac{\Gamma(\mathbf{k}, \omega'^2)}{\omega'^2 - a_N - \Gamma(\mathbf{k}, \omega'^2)}}}}$$

where $\Gamma(\mathbf{k}, \omega'^2)$ is the asymptotic part of the continued fraction, and

$$\begin{aligned} a_n(\mathbf{k}) &= \frac{\langle \phi_n | \widetilde{\mathbf{D}}_{eff} | \phi_n \rangle}{\langle \phi_n | \phi_n \rangle} \quad \text{and} \\ b_n^2(\mathbf{k}) &= \frac{\langle \phi_n | \phi_n \rangle}{\langle \phi_{n-1} | \phi_{n-1} \rangle} \quad ; \quad b_1^2 = 1 \end{aligned}$$

To implement the above recursion, we require to know the effect of the operator $\widetilde{\mathbf{D}}_{eff}$ on a general state in augmented reciprocal space [Biswas *et al* 1995]. Some of the main operations are shown in Appendix 1.

So far the expression for the averaged Green function is *exact*. Approximations are introduced at this stage for its actual numerical evaluation. The mean-field theories essentially obtain the self-energies because of disorder scattering, self-consistently and approximately and then calculate the averaged Green function either from the Green

function without disorder or the virtual crystal Green function. The Coherent potential approximation (CPA) proposed by Soven 1967, the cluster CPA proposed by Mookerjee and Singh 1985 and Mookerjee and Singh 1988, the traveling cluster approximation (TCA) proposed by Mills and Ratnavararaksha 1978 and Kaplan *et al* 1980 and the itinerant CPA (ICPA) proposed by Ghosh *et al* 2002 basically all belong to this category. The latest work referenced represent the most sophisticated version of the mean-field theories. We shall propose an approximation that will start from the infinite continued fraction and approximate its asymptotic part by an analytic termination procedure. The coefficients a_n, b_n are calculated exactly up to a finite number of steps and the asymptotic part is then replaced by a terminator : $\Gamma(\mathbf{k}, \omega'^2) \simeq T(\mathbf{k}, \omega'^2)$. The terminator ensures that the approximate Green function has Herglotz analytic properties.

In the absence of disorder in the problem, the Green function for a given mode is of the form :

$$G_0(\mathbf{k}, \omega'^2) = \frac{1}{\omega'^2 - \omega_0^2(\mathbf{k})}$$

The spectral function $A_0(\mathbf{k}, \omega'^2)$ is a delta function of the form $\delta(\omega'^2 - \omega_0^2(\mathbf{k}))$. If we write

$$\begin{aligned} \Sigma(\mathbf{k}, \omega'^2) &= a_1(\mathbf{k}) - \omega_0^2(\mathbf{k}) + \frac{b_2^2(\mathbf{k})}{\omega'^2 - a_2(\mathbf{k}) - \frac{b_3^2(\mathbf{k})}{\ddots}} \\ &= a_1(\mathbf{k}) - \omega_0^2(\mathbf{k}) + \sigma(\mathbf{k}, \omega'^2) \end{aligned} \quad (3.14)$$

Then,

$$\ll G(\mathbf{k}, \omega'^2) \gg = G_0(\mathbf{k}, \omega'^2 - \Sigma(\mathbf{k}, \omega'^2))$$

Obviously from above $\Sigma(\mathbf{k}, \omega'^2)$ is the disorder induced self-energy. Damped vibrations occur with reduced frequencies at $\omega'_0(\mathbf{k})$ which are the solutions of the implicit equation :

$$\omega'_0{}^2(\mathbf{k}) - a_1(\mathbf{k}) - \Re \sigma(\mathbf{k}, \omega'_0{}^2(\mathbf{k})) = 0$$

and their disorder induced widths are :

$$\mathcal{W}(\mathbf{k}, \omega'_0{}^2(\mathbf{k})) = -\frac{1}{\pi} \Im \sigma(\mathbf{k}, \omega'_0{}^2(\mathbf{k})) \quad (3.15)$$

The average spectral function $\ll A_\lambda(\mathbf{k}, \omega'^2) \gg$ for a mode labelled λ is related to the averaged Green function in reciprocal space as :

$$\ll A_\lambda(\mathbf{k}, \omega'^2) \gg = -\frac{1}{\pi} \lim_{\delta \rightarrow 0^+} \left[\Im \left\{ \ll G_\lambda(\mathbf{k}, \omega'^2 - i\delta) \gg \right\} \right] \quad (3.16)$$

The averaged density of states is given by :

$$\ll n(\omega') \gg = \frac{2\omega'}{3} \sum_{\lambda} \int_{BZ} \frac{d^3\mathbf{k}}{8\pi^3} \ll A_{\lambda}(\mathbf{k}, \omega'^2) \gg$$

Here λ labels the particular normal mode branch and BZ is the Brillouin zone.

The dispersion curves for different modes are then obtained by numerically calculating the peak frequencies of the spectral function. This averaged spectral function gives, in principle, a proper description of the dynamics but it does not involve any weighting by scattering lengths. The dispersion curves so obtained are nearly the same as those obtained experimentally from the peak frequencies of the coherent structure factors S_{coh} . This is because the coherent structure factors are nothing but the averaged Green functions weighted by the coherent scattering lengths. The intensities and the line shapes measured from S_{coh} and the imaginary part of Green function may differ significantly, but the peak positions will generally differ little.

3.3 Dispersion Relations and disorder induced line-widths

Experimental determination of the phonon dispersion and line-widths are deduced from the averaged coherent scattering structure factors. The expression for these can be written as :

$$\ll S_{coh}(\mathbf{k}, \omega^2) \gg = -\frac{1}{\pi} \Im m \ll \mathbf{b} \mathbf{G}(\mathbf{q}, \omega^2) \mathbf{b} \gg \quad (3.17)$$

here, thermal neutrons with wave-vector \mathbf{k} gets scattered to final state of wave-vector \mathbf{k}' , $\mathbf{q} = \mathbf{k} - \mathbf{k}' + \mathbf{Q}$ with \mathbf{Q} being a reciprocal lattice vector. The energy lost by the incoming neutrons are taken up by the phonons : $(\hbar^2/2M_n)(k^2 - k'^2) = \hbar \omega$. $f(\omega)$ is the Bose distribution function and

$$\mathbf{b} = \sum_R b_R \delta_{\alpha\beta} \mathbf{P}_R$$

where b_R is the scattering length of the nucleus occupying the site R . This is a random variable taking two values b_A or b_B depending on which kind of atom sits at the site labelled R . For comparison with experiment we have to calculate $-(1/\pi) \Im m \ll (\mathbf{b} \mathbf{G}(\mathbf{q}, \omega) \mathbf{b})^{\alpha\alpha} \gg$, rather than the spectral function. For ordered materials the two are proportional, but if the scattering lengths are themselves random then although this has very little effect

on the dispersion curves, it does affect the line-shapes and line widths. We can easily implement such an average within the ASF :

$$\ll \mathbf{b} \mathbf{G}(\mathbf{q}, \omega^2) \mathbf{b} \gg = \langle \mathbf{q} \otimes \{\emptyset\} | \tilde{\mathbf{b}} \left(\tilde{\mathbf{M}}\omega^2 - \tilde{\mathbf{D}} \right)^{-1} \tilde{\mathbf{b}} | \mathbf{q} \otimes \{\emptyset\} \rangle$$

where

$$\tilde{\mathbf{b}} = \ll \mathbf{b} \gg \mathbf{I} \otimes \mathbf{I} + (y - x)(b_B - b_A) \sum_R \mathbf{P}_R^\dagger \otimes \mathbf{P}_R + \sqrt{xy}(b_B - b_A) \sum_R \mathbf{T}_R^{\uparrow\downarrow} \otimes \mathbf{P}_R$$

Carrying out algebra similar to the one for the averaged Green function, we obtain :

$$\ll \mathbf{b} G(\mathbf{q}, \omega^2) \mathbf{b} \gg = \langle 1_b | \left(\omega_b^2 \tilde{\mathbf{I}} - \tilde{\mathbf{D}}_{eff}^b \right)^{-1} | 1_b \rangle \quad (3.18)$$

where,

$$|1_b\rangle = \left(\frac{X_1}{\hat{X}} \right)^{-1/2} \| \{\emptyset\} \rangle + \left(\frac{X_3}{\hat{X}} \right)^{-1/2} \| \{R\} \rangle$$

with,

$$\begin{aligned} X_1^{-1/2} &= x m_A^{-1/2} b_A + y m_B^{-1/2} b_B \\ X_2^{-1/2} &= (y - x) \left(m_A^{-1/2} b_A - m_B^{-1/2} b_B \right) \\ X_3^{-1/2} &= \sqrt{xy} \left(m_A^{-1/2} b_A - m_B^{-1/2} b_B \right) \\ \hat{X} &= \ll \frac{b^2}{m} \gg = x \frac{b_A^2}{m_A} + y \frac{b_B^2}{m_B} \end{aligned} \quad (3.19)$$

Also

$$\omega_b'^2 = \hat{X} \omega^2 \quad \text{and} \quad \tilde{\mathbf{D}}_{eff}^b = \tilde{\mathbf{W}} \tilde{\mathbf{D}} \tilde{\mathbf{W}}$$

where,

$$\tilde{\mathbf{W}} = \left(\frac{m_1}{\hat{X}} \right)^{-1/2} \mathbf{I} \otimes \mathbf{I} + \left(\frac{m_2}{\hat{X}} \right)^{-1/2} \sum_R \mathbf{P}_R \otimes \mathbf{P}_R^\dagger + \left(\frac{m_3}{\hat{X}} \right)^{-1/2} \sum_R \mathbf{P}_R \otimes \mathbf{T}_R^{\uparrow\downarrow} \quad (3.20)$$

The subsequent recursion calculation follows the identical steps as for the averaged spectral functions. We have chosen a second neighbour force constant model, with dynamical matrices fitted to reproduce the dispersion curves. The disorder induced widths are the quantities which are more sensitive to the effect of randomness as compared to the frequencies (i.e. dispersion curves), and as such will be one of the focus of this work. In order to extract the full width at half maxima (FWHM), we have fitted the coherent structure

factors to Lorentzians exactly as the experimentalists do to extract the same. The advantage of including the scattering length fluctuation will be clear when we will show the nature of the line widths for $Ni_{55}Pd_{45}$ alloy with and without inclusion of the scattering length fluctuation (i.e. Calculating the widths once by fitting the spectral functions to Lorentzians and then the structure factors to Lorentzians). Our aim in this chapter is to propose the augmented space recursion as a useful technique to study effects of diagonal, off-diagonal and environmental disorder.

In the following three subsections, we present our calculations on $Ni_{55}Pd_{45}$, $Ni_{88}Cr_{12}$ and $Ni_{50}Pt_{50}$ alloys. The choice is not arbitrary. Mass disorder dominates in NiPd alloys while force constant disorder is large in NiCr alloys. NiPt alloys have large disorder *both* in mass and force constants. Since in the phonon problem we have both kinds of disorder, it would be interesting to note the interplay between them in this series of alloys. The concentrations are chosen so that we may compare our results with existing work.

3.4 $Ni_{55}Pd_{45}$ face-centered cubic binary alloy (Strong Mass Disorder)

If we look at Table (4.1), it immediately shows us that for NiPd alloys, Mass disorder is much larger than the force constant disorder. The mass ration $\frac{m_{Pd}}{m_{Ni}}$ is 1.812 whereas the Pd-force constants are only 15 % larger than those of Ni. We shall choose $Ni_{55}Pd_{45}$ alloy for application of our formalism developed in Section (3.2). This particular alloy has already been studied within the ICPA by Ghosh *et al* 2002, CCPA by Mookerjee and Singh 1988 and experimentally by inelastic neutron scattering [Kamitakahara and Brockhouse, 1974]. In the numerical calculation, we have used 500 ω -points. The dispersion relation is calculated for 25 \mathbf{k} -points along each of the three highest symmetry directions.

In Fig. 3.1 we display the coherent scattering structure factors obtained from our recursion calculation along the highest symmetry directions ($[\zeta 00]$, $[\zeta \zeta 0]$, $[\zeta \zeta \zeta]$), $\zeta = |\vec{k}|/|\vec{k}_{max}|$ for different branches. For a particular direction and branch the different curves indicates the spectral functions for various ζ points starting from the lowest value (i.e. $\zeta = 0$) to the edge of the Brillouin zone (i.e. $\zeta = 1$ in units of $2\pi/a$). The first thing to note is that the structure factors are (in contrast to Lorentzian shape) often

	Ni	Pd	Pt	Cr
Atomic number	28	46	78	24
Atomic mass (amu)	58.71	106.4	195.09	51.996
Free atom valence config.	$3d^84s^2$	$4d^{10}$	$5d^96s^1$	$3d^54s^1$
Lattice constant (fcc)	3.524	3.8904	3.924	3.68(fcc) 2.89(bcc)
Elastic constants at $296^\circ K$ ($10^{12}dyne/cm$)				
C_{11}	2.461	2.270	3.467	3.5
C_{12}	1.501	1.759	2.507	0.678
C_{44}	1.220	0.717	0.765	1.010
n-n force constants (in units of dyne/cm)				
1XX	17319	19337	26358	37483
1XY	19100	22423	30317	17453
1ZZ	-436	-2832	-7040	-13229
n-n-n force constants (in units of dyne/cm)				
2XX	1044	1424	4926	-
2YY	-780	210	-537	-

Table 3.1: General properties of fcc Ni, Pd, Pt and Cr. The force constants for Ni, Pd and Pt are taken from Dutton *et al* 1972 and that for Cr is taken from Mookerjee and Singh 1988

asymmetric near the resonances. The asymmetries can be described as a tendency of more scattering to occur near the resonance frequencies. In other words the shape of a mode with a frequency slightly lower or higher than that of a resonance tends to have a second peak or wide tail over the resonance region. In fact if one looks at the $[\zeta\zeta 0]$ L or T1 (doubly degenerate) and $[\zeta\zeta\zeta]$ L or T1 or T2 (3-fold degenerate) branches, the shape of a doubly peaked structure factor is much more clear. Out of these two peaks, one peak corresponds to the dispersion curve for the longitudinal mode (L) and the other peak to the transverse mode (T). Experimentally, for some neutron groups corresponding to transverse phonons with frequencies just below the lower resonance, definite asymmetry to the right was observed. Such asymmetries are clearly observed for the $[\zeta 00]$ T and

[$\zeta\zeta 0$]T1 branches. It is important to note that the structure factors have a pronounced \mathbf{k} and branch dependence.

In Fig. 3.2 we display the dispersion curves, which were constructed by numerically determining the peaks in the coherent scattering structure factor. In this chapter our main focus is the development of the augmented space recursion method. Accurate determination of the force constants shall be left for the future. Ghosh *et al* 2002 have attempted much more detailed determination of the force constants. For the time being we have used the same parametrization of the force constants as they did. These dispersion curves (solid lines) are compared with the experimental results Kamitakahara and Brockhouse, 1974 (filled circles). The dotted lines span the calculated FWHM's. The procedure of calculating FWHM's has already been discussed. The asymmetry in the widths is again clearly observed in the two transverse branches quoted above. The results are in good agreement with the experiment for all the three symmetry directions and for each branch. Agreement can be achieved by varying only one parameter in the force constant matrix. This suggests that the force constant disorder is weak and the system is dominated by the mass disorder, as is clear from the numerical values of the parameters given in Table 4.1 . If one looks at the previous results for the dispersion curves (i.e. VCA, CPA and ICPA curves) Ghosh *et al* 2002, it will be clear that in the low wave vector regime, there is no distinction between these results and ours, Because the self averaging of both mass and force constants over a single wavelength reduces the CPA, ICPA and the ASR results to become close to the VCA. However as we move toward high wave vectors, the VCA curve deviates from the experimentally observed one and lies lower in frequency as compared to the ICPA and the ASR results. The reason is that VCA uses an averaged mass. In contrast to this, for those theories which capture the effect of mass fluctuation (as do the ICPA and the ASR), the lighter atoms (Ni in this case) dominate in the high wave vector region and push the frequencies up. That is why our results agree very well across the Brillouin zone.

The FWHM's are much more sensitive to approximations as compared to the frequencies. These are shown in figure (3.3). The FWHM's shown in the left are those which have been calculated without including any scattering length fluctuation, while in the right are those where the fluctuation has been included. The circles along with the error

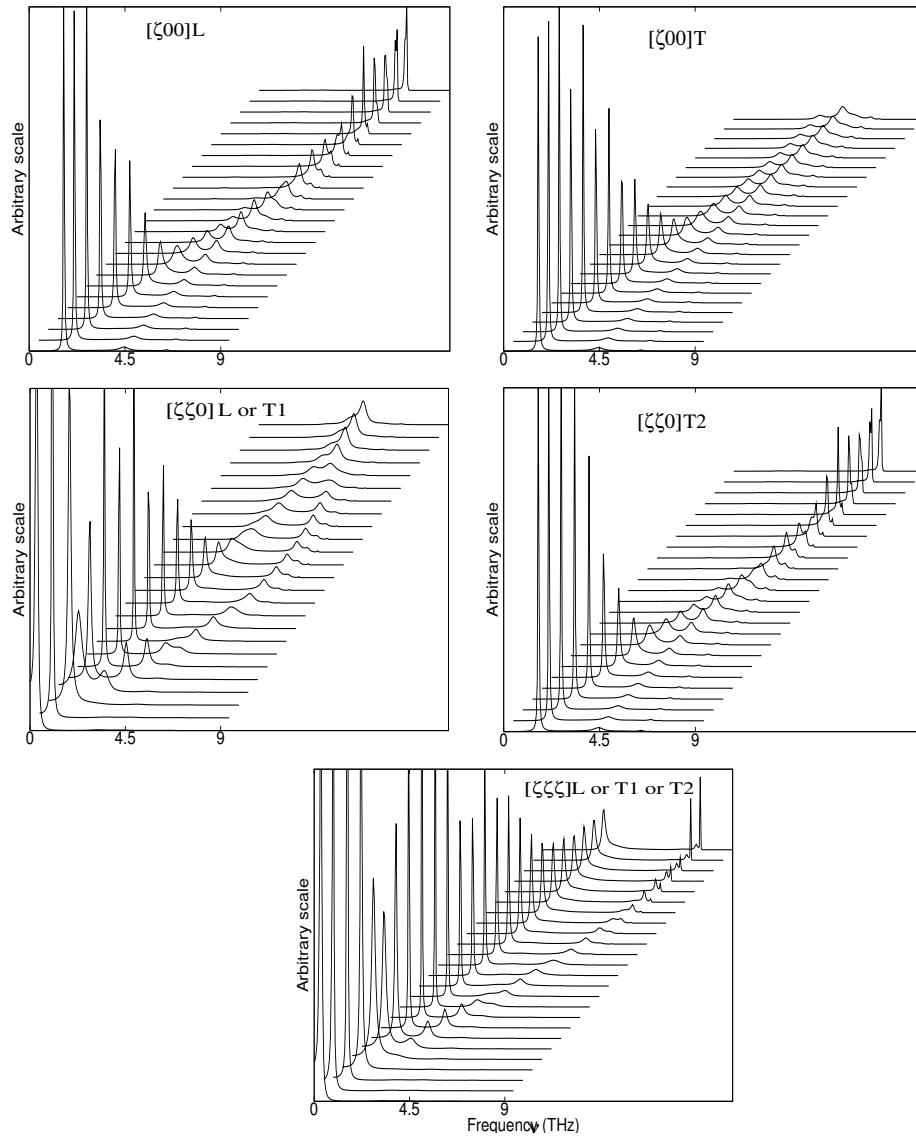


Figure 3.1: Total coherent structure factors in different directions with different branches for $\text{Ni}_{55}\text{Pd}_{45}$. In each of the different directions and branches, the various curves indicate the total structure factors for various ζ values starting from the lowest value to the edge of the Brillouin zone. In $[\zeta 0 0]$ direction T1 and T2 modes are degenerate, in $[\zeta \zeta 0]$ direction L and T1 modes are degenerate and in $[\zeta \zeta \zeta]$ direction all the three modes are degenerate. The y-axis is in an arbitrary scale with heights scaled to the maximum height. Different curves for different ζ values are shifted along the x-axis in order to facilitate vision.

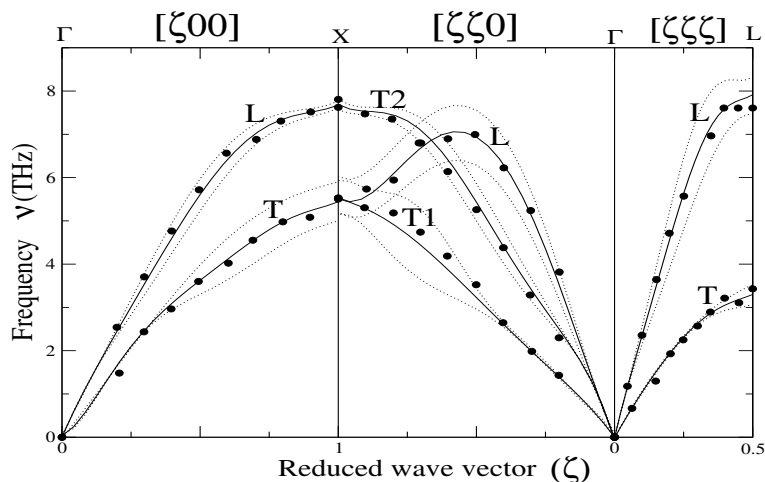


Figure 3.2: Dispersion Curves (frequency ν vs. reduced wave vector ζ) for $\text{Ni}_{55}\text{Pd}_{45}$ calculated from recursion (solid line). The force constants used are given in the text. The filled circles are the experimental data [Kamitakahara and Brockhouse, 1974] . In all the three panels the thin dotted lines span the FWHM's .

bars are the experimental data [Kamitakahara and Brockhouse, 1974]. It is obvious that the nature of the line widths are not the same in the two cases, rather the one including scattering length fluctuation is matching more closely with the experimental data than the one without including the fluctuation. That should be obvious because the experimentalists do include this fluctuation. Our results show very strong branch and wave-vector dependent widths and in good agreement with the experimental results of Kamitakahara and Brockhouse except in the $[\zeta\zeta\zeta]L$ mode. The reason for this may be because of the highly asymmetric line shapes in the $[\zeta\zeta\zeta]L$ mode. The single site CPA yields branch and \mathbf{k} independent widths. It cannot capture the essentially off-diagonal disorder of the problem. The ICPA and the ASR manages to capture this feature. One should note that the structure factors are often asymmetric in shape and the usual Lorentzian fits carried out by most people may not be valid.

3.5 $\text{Ni}_{88}\text{Cr}_{12}$ binary alloy (Strong Force constant disorder)

We shall choose this alloy as being the nearest to that studied experimentally by Bosi *et al* 1978. Determination of the force constant matrices for this alloy becomes difficult,

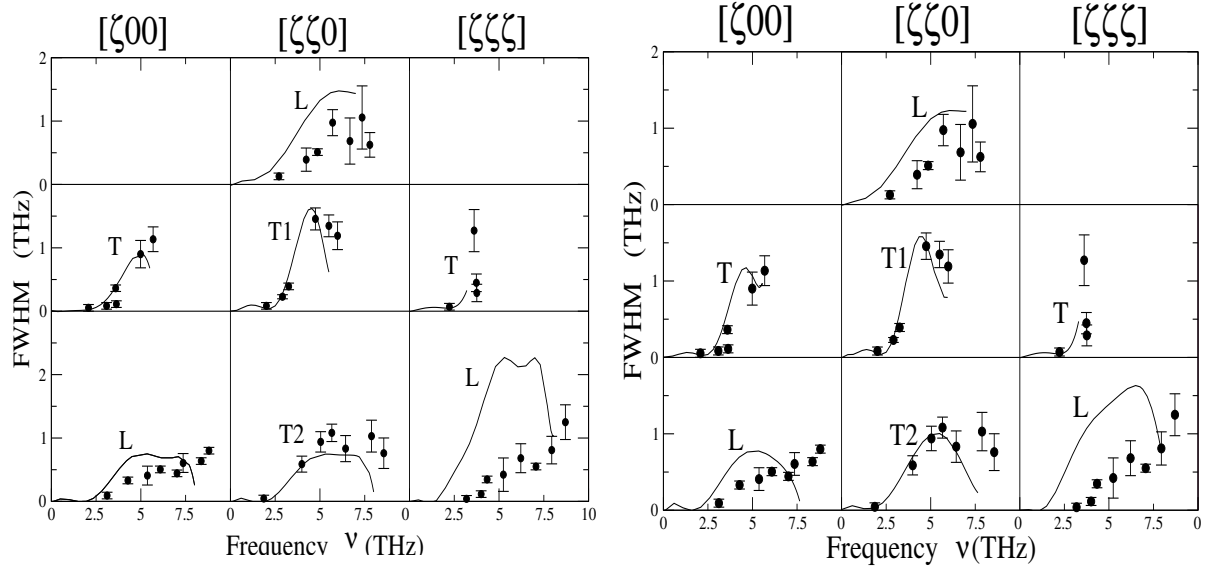


Figure 3.3: Full widths at half-maximum for the NiPd alloy as function of frequency for different directions in k-space and different modes without (left) and with (right) the inclusion of the scattering length fluctuation. The filled circles along with the error bars are the experimental data [Kamitakahara and Brockhouse, 1974]

because pure Cr is body centered cubic, but alloyed with Ni, up to 30% Cr it forms face centered cubic alloys. The force constants of pure Cr may be nothing like those of Cr in this alloy. Until we are able to determine these from a more first-principles type approach, our determination of the force-constants for this alloy will remain tentative. We shall consider a hypothetical fcc Cr, whose force constants are related to the elastic constants of bcc Cr via :

$$\begin{aligned}
 C_{11} + C_{12} &= 4(f_l - f_{\nu} - f_t)/a \\
 C_{11} - C_{12} &= (f_l + 5f_{\nu} + f_t)/a \\
 C_{44} &= (f_l + f_{\nu} + 2f_t)/a
 \end{aligned}$$

The values of C_{11} , C_{12} and C_{44} are taken from Leibfried *et al* (given in Table I). It has been observed that the spectral functions and the structure factors for $\text{Ni}_{88}\text{Cr}_{12}$ has strong evidence of branch dependent widths as also asymmetry in certain directions. This lends credence to our belief that force-constant disorder leads to both asymmetry and strong

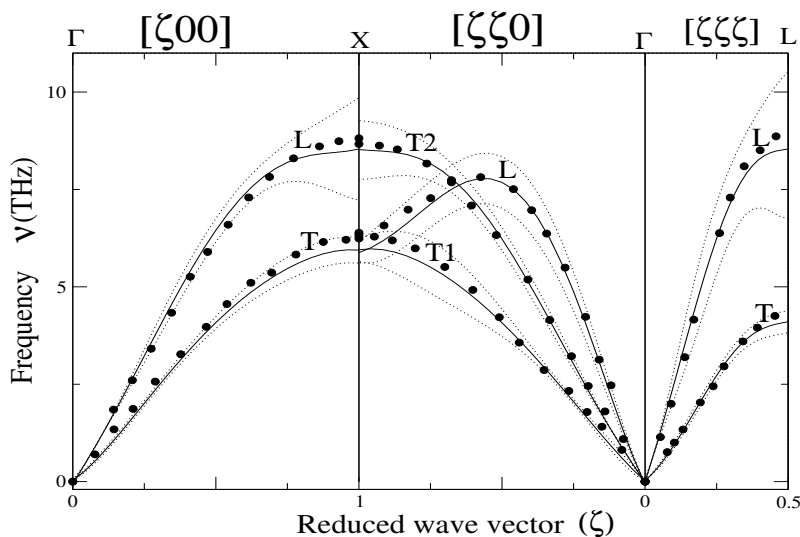


Figure 3.4: Dispersion Curves (frequency ν vs. reduced wave vector ζ) for $\text{Ni}_{88}\text{Cr}_{12}$ calculated from recursion (solid line). The force constants used are given in the text. The filled circles are the 2 CPA results of R.P.Singh's thesis 1982 . In all the three panels the thin dotted lines span the FWHM's .

wave-vector and frequency dependence of the line-shapes.

The influence of force constant disorder may be demonstrated more prominently in the dispersion curves and widths. In Fig. 3.4, we display the dispersion curves along with the FWHM's using the force constants of Table 4.1. The procedure has already been discussed in the previous section. These dispersion curves compare well with the experimental results [Bosi *et al* 1978] as well as the 2 CPA results of R.P.Singh's thesis 1982 (filled circles). The dotted lines span the calculate FWHM's. It should be noted that in the low frequency region, the widths are small but start to become significant as the phonon frequency increases. The widths are comparatively larger in the $[\zeta 00]$ L, $[\zeta \zeta \zeta]$ L and $[\zeta \zeta 0]$ T2 branches for high ζ -values. Looking at the dispersion curves, one should notice that the behaviour of the natural widths were somehow complemented in the behaviour of the frequencies. There is little evidence of resonances. This is expected, since clear cut resonances are characteristics of large mass disorders only.

In Fig. 3.5 we show the FWHM as a function of frequency. It is clear that there is strong evidence of mode and k -dependence. The FWHMs are very large and asymmetric

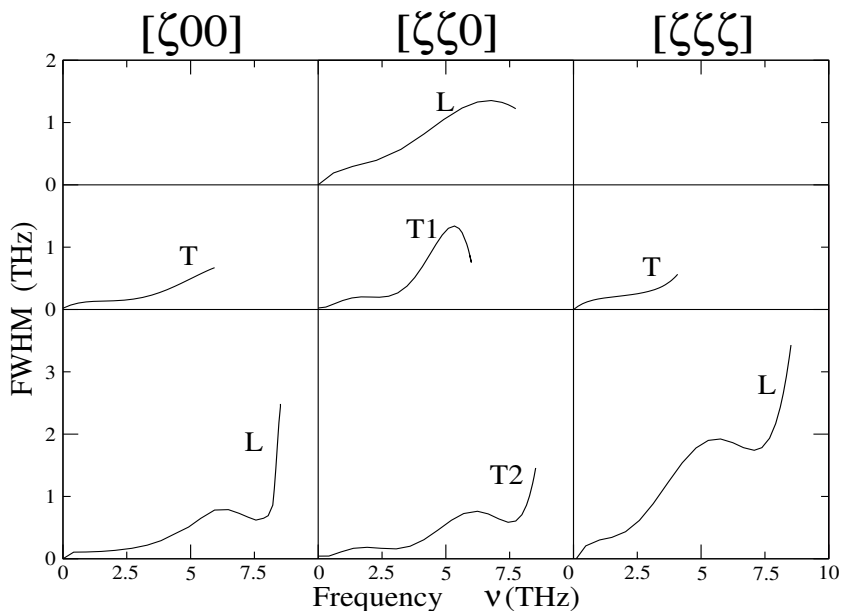


Figure 3.5: Full widths at half-maximum for the NiCr alloy as function of frequency for different directions in k-space and different modes.

for the longitudinal modes near the band edge frequencies.

It is obvious from the above discussions that the force constant disorder plays a significant role in $\text{Ni}_{88}\text{Cr}_{12}$; and a theory capturing only mass disorder effect (e.g. like CPA) fails to provide various essential features.

3.6 $\text{Ni}_{50}\text{Pt}_{50}$ alloy (Strong Mass and Force constant disorder)

Being encouraged by the right trend of theoretical results toward the experimental results in the $\text{Ni}_{55}\text{Pd}_{45}$ and $\text{Ni}_{88}\text{Cr}_{12}$ alloys, where either of the two disorders – diagonal and off-diagonal dominates, we now apply our formulation to NiPt alloys where both disorders are predominant. The mass ratio $m_{\text{Pt}}/m_{\text{Ni}}$ is 3.3 (quite large compared to previous alloys) and the nearest neighbour force constants of Pt are on an average 55% larger than those in Ni. Tsunoda *et al* 1979 have studied this system thoroughly covering a wide range of concentration ($x=0.05$, $x=0.3$, $x=0.5$) by inelastic neutron scattering. In our case, we have considered $x=0.5$ where we expect the disorder induced scattering to have the

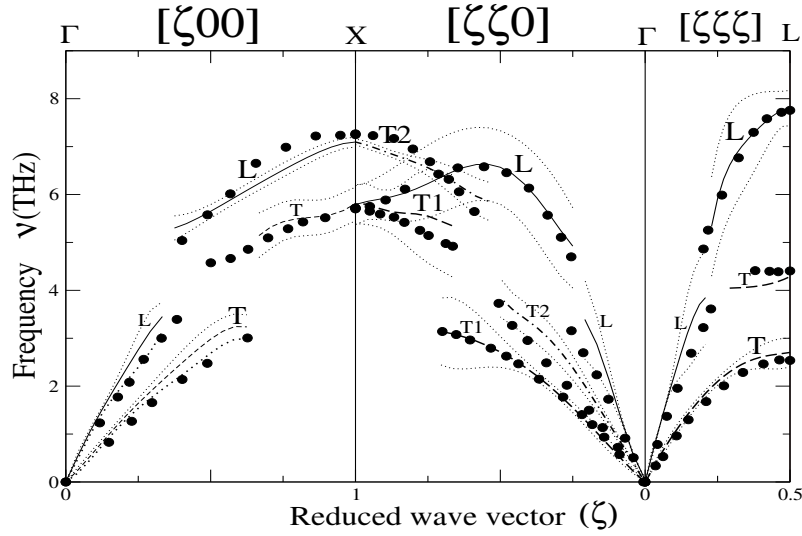


Figure 3.6: Dispersion Curves (frequency ν vs. reduced wave vector ζ) for $\text{Ni}_{50}\text{Pt}_{50}$ calculated from recursion . The force constants used are given in the text. The solid lines are the L-branch in all the three panels, the dashed lines are the T-branch in the left and right panels. In the $[\zeta \zeta 0]$ direction the dashed line indicate the T1 branch while the dot-dashed line indicate the T2 branch. The filled circles are the ICPA results [Ghosh *et al* 2002]. In all the three panels the thin dotted lines span the FWHM's.

strongest effect.

In this case, the spectral functions as well as the structure factors show few extra features : Even in $[\zeta 0 0]L$, $[\zeta 0 0]T$ and $[\zeta \zeta 0]T2$ modes, unlike the previous two cases both the functions have one usual well defined peak (observed more clearly in the middle-regime of the Brillouin zone) along with a weakly defined peak with no gap in between. The occurrence of such a weakly defined peak is due to the inclusion of force constant disorder. Ghosh *et al* 2002 have argued that it is entirely because of the off-diagonal disorder in the force constants. We refer the reader to their paper for the detailed arguments. Here we note that the feature is equally well reproduced in our augmented space recursive technique as well. why this should be so ? The effect of force constant disorder can be understood more clearly by looking at the dispersion curves and widths.

In figures (3.6) and (3.7) we display the dispersion curves and widths respectively obtained in the recursion using the force constants as given in the text. The solid lines are the L-branch in all the three panels, the dashed lines are the T-branch in the left

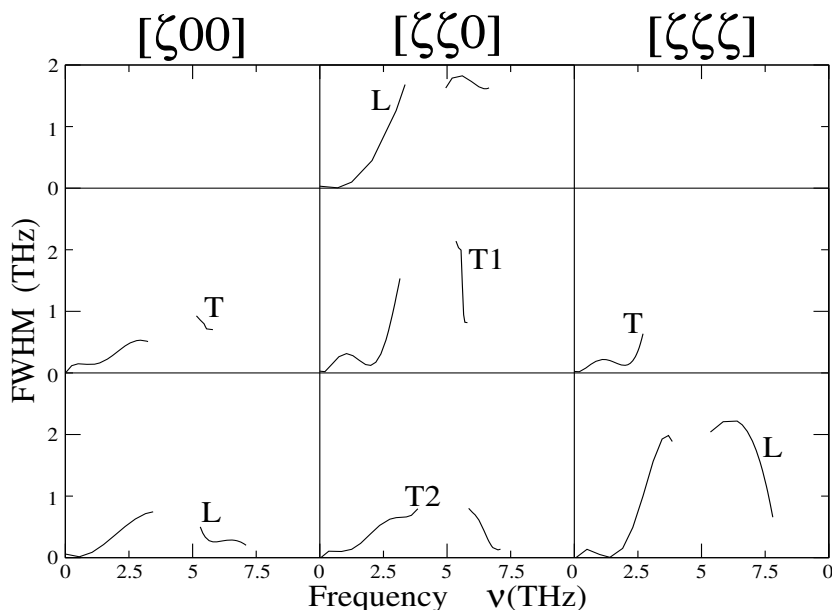


Figure 3.7: Full widths at half-maximum for the NiPt alloy as function of frequency for different directions in k-space and different modes including the scattering length fluctuation.

and right panels, In the middle panel the dashed line indicate the T1-branch while the dot-dashed line indicate the T2-branch. We have used the same parametrization of the force constants as used by Ghosh *et al* 2002. These dispersion curves (solid lines) are compared with that calculated in the ICPA (filled circles) by Ghosh *et al* 2002. The aim of this work was to establish the ASR as a computationally fast and accurate method for phonon calculations for random alloys.

For all the three panels the thin dotted lines indicate the FWHM's. Unlike the previous two cases, the dispersion curves in this case have very different characteristic features. The splitting of the curves in all the three symmetry directions is the main feature. This is due to strong resonances, a feature of large mass disorder. Also as one can see that near the resonances (around 4 THz) the FWHM becomes very large. Tsunoda finds this resonance near 3.8 THz, while the CPA gives a rather lower value of 3 THz. In addition to these features, It has been observed that around 7 THz, the structure factor has a third small peak split from the main branch. This evidence of a weak resonance was also speculated by Mookerjee and Singh 1985. The overall agreement of our dispersion curves with those

calculated in the ICPA is good .

In sum, the force constant disorder plays a significant role in $\text{Ni}_{50}\text{Pt}_{50}$, and a theory with mass disorder only fails both qualitatively and quantitatively in such cases. On the other hand, ASR successfully explains the effects of force constant disorder through its effect on the coherent structure factor, and demonstrates the relative importance of the contributions of various atomic species to the dispersion curves and disorder induced line-widths which the CPA can not. The ASR and the $\text{Ni}_{50}\text{Pt}_{50}$ alloy system therefore provide a proper test case for force constant disorder and show that the ASR can form a basis for understanding the lattice dynamics of other binary alloys.

3.7 Concluding Remarks

We have presented in this chapter the application of the augmented space recursion for a reciprocal space study of phonon dispersion, disorder induced line-widths and line shapes for random binary alloys. We have demonstrated how this multiple scattering based formalism captures the effects of off-diagonal and environmental disorder. The approximation involving termination of continued fraction expansions of the Green function retains the essential Herglotz analytic properties. We have applied the method to three classes of alloys : NiPd where mass disorder dominates, and hence the CPA consequently does a rather good job , NiCr where force constant disorder dominates and NiPt which demonstrates the prominence of force constant disorder even in a case where the mass ratio is $\simeq 3.3$. Wherever possible we have compared our results with neutron scattering data as well as the most sophisticated mean field theory recently proposed by Ghosh *et al* 2002. Both qualitatively and quantitatively our results agree well with the available data. We propose the augmented space technique as a computationally efficient method for the study of phonons in disordered systems. Our approach in this chapter made no attempt to obtain the force constant themselves from first principles, but rather resorted, as others did earlier, to fitting them from experimental data on the constituent metals. In the next chapter, we shall rectify this, and attempt to obtain the dynamical matrix itself from a more microscopic theory : the so called Density Functional Perturbation theory.

Chapter 4

The Itinerant CPA and Augmented Space Recursion

4.1 Introduction

The last thirty years have seen numerous attempts at setting up a quantitatively accurate theory of phonons in disordered alloys. One of the earliest successful approximations was the coherent potential approximation Taylor 1967 (CPA). This approximation was a considerable improvement on the existing theories and, in examples of homogeneous disorder, was shown to yield configuration averaged Green functions which maintained lattice translational symmetry and the herglotz analytical properties essential for physical interpretation. Despite its success, particularly in the electronic problem, the CPA was a single-site, mean-field approximation and could deal with only diagonal (or mass, in the case of phonons) disorder. The phonon problem is specifically difficult because, in it, diagonal and off-diagonal disorders are impossible to separate. Moreover, the sum rule satisfied between the diagonal and off-diagonal parts of the force-constants leads to environmental disorder. In the electron problem too, whenever there was off-diagonal disorder, as in the case of alloys with large size difference between its constituents leading to local lattice distortions [Dasgupta *et al* 1996] or environmental disorder as in the case of alloys with short-range order [Mookerjee and Prasad 1993, Durga *et al* 2004], the CPA was found to be inadequate.

The hunt for adequate extensions of the CPA was quite rigorous during the seventies

⁰The contents of this chapter has been communicated to *Phys. Rev. B* :

1. Aftab Alam, Subhradip Ghosh and A Mookerjee, *Phys. Rev. B* (2006) : cond-mat/0610391

and eighties [Gonis and Garland 1978, H. Shiba 1968]. Most of these generalizations were valid for very special types of off-diagonal disorder, which were mostly unphysical, or violated translational symmetry and herglotz properties. Eventually, three approaches emerged as the most successful. Two of them were based on the augmented space theorem of Mookerjee² 1973 : the itinerant coherent-potential approximation (ICPA) of Ghosh *et al* 2002 and the augmented space recursion (ASR) of [Saha *et al* PRB 1994 and Alam and Mookerjee 2004]. The former was an extension of the ideas of Mills and Ratnavararaksha 1978 and Kaplan *et al* 1980 and the latter combined the augmented space technique with the recursion method of Haydock *et al* 1972. The third was a very different and rather striking approach developed by Rowlands *et al* 2005 and Biava *et al* 2005 (the non-local CPA or NL-CPA) using the idea of *coarse graining* in reciprocal space originally proposed by Jarrel and Krishnamurthy 2001.

More importantly a first principles ab-initio theory of phonons in disordered alloys is still lacking. Such a theory is needed in order to gain a microscopic understanding of the interplay of force constants in the complex phenomenon of phonon excitations. We have collaborated with the group who developed Itinerant coherent-coherent potential approximation (ICPA) for the study of phonon excitations in disordered alloys.

Our aim in this chapter is twofold : First, we shall discuss the similarities and differences between the two methods (ICPA and ASR) based on the augmented space theorem. We shall apply both the techniques to identical models of an alloy system, FePd, and discuss the comparison between their results. Secondly, we shall estimate the dynamical matrices from a first-principles approach to the parent ordered alloys and compare the ICPA and ASR results with experiment. We shall argue that first-principles estimates of the dynamical matrices on ordered versions do not yield quantitatively accurate results (in comparison with experiment) for the disordered alloys. We shall propose that we need to go beyond and estimate the dynamical matrices from a model of embedded atoms in a fully disordered background.

4.2 The Itinerant CPA and Augmented space recursion

The augmented space theorem described in chapter (2) is an *exact* statement. It is a clever book keeping technique to include the effects of disorder fluctuations in the model of phonons in our random alloy. However, it is *not* an algorithm for the approximate calculations of spectral and other physical properties of phonons in disordered alloys. For that we have to turn to either mean-field approximations like the CPA and ICPA or alternatively to the ASR. The coherent potential like mean-field approximations begin with a *partition* of the augmented space into a part which is spanned by the *reference* or *null cardinality* state $|\{\emptyset\}\rangle$ which we shall call the *average* configuration state and the remaining part $\Psi - |\{\emptyset\}\rangle\langle\{\emptyset\}|$ spanned by *fluctuation* states : $\{|\{\mathcal{C}\}\rangle\}$. With this partition, any operator can be written in a block representation :

$$\mathbf{A} = \begin{pmatrix} \mathbf{A}_1 & \mathbf{A}' \\ \mathbf{A}'^\dagger & \mathbf{A}_2 \end{pmatrix}$$

The partition or downfolding theorem then allows us to invert this operator in the subspace spanned by the *average* configurations alone. By the augmented space theorem this is the configuration average. If we define the operator \mathbf{K} as $(\mathbf{m}\omega^2 - \Phi)$, then using the above partition :

$\mathbf{K}_1 = (\ll \mathbf{m} \gg \omega^2 - \ll \Phi \gg)$. The downfolding theorem and augmented space theorem together give us :

$$\begin{aligned} \ll \mathbf{G}(\omega^2) \gg &= (\mathbf{K}_1 - \mathbf{K}'^\dagger \mathbf{F} \mathbf{K}')^{-P_1} \\ &= (\mathbf{G}_{VCA}^{-1}(\omega^2) - \Sigma(\omega^2))^{-P_1} \\ \mathbf{F} &= \mathbf{K}_2^{-P_2} \quad \text{is the itinerator} \end{aligned} \quad (4.1)$$

$$\Sigma = \mathbf{K}'^\dagger \mathbf{F} \mathbf{K}' \quad \text{is the self-energy} \quad (4.2)$$

Here \mathbf{A}^{-P_1} and \mathbf{A}^{-P_2} refer to the inverses of the operator \mathbf{A} in the subspaces labelled by 1 and 2. This is exactly the partitioning idea introduced by Srivastava *et al* 1982. Ghosh *et al* 2002 next confined themselves to *single fluctuation* states of the type $|\{R\}\rangle$ and went ahead to self-consistently evaluate the self-energy in this approximation. Adopting their notation $\langle\{R\}|\mathbf{A}|\{R'\}\rangle = A^{(R)(R')}$, they used translational symmetry in augmented space

[Ghosh *et al.* 1999] and approximated the self-energy and *itinerator* \mathbf{F} within the single fluctuation states :

$$\Sigma = \sum_{RR'} \mathbf{K}'^{\dagger(R)} \mathbf{F}^{(R)(R')} \mathbf{K}'^{(R')} \quad (4.3)$$

$$\mathbf{F}^{(R)(R')} = \mathbf{G}^{(R)} \left[\delta_{RR'} + \sum_{R''} \mathbf{V}^{(R)(R'')} \mathbf{F}^{(R'')(R')} \right] \quad (4.4)$$

In going from the equation (7.1) to (7.3) all contributions to the self-energy of configuration states with more than one fluctuations in more than one site have been neglected. Similarly in going from equation (7.2) to (7.4), matrix elements of the *itinerator* \mathbf{F} between configuration states with more than one fluctuation present at a time, which corresponds to coherent scattering from more than one site have been neglected and such states do not contribute to \mathbf{F} and hence to the self-energy Σ within this approximation. The second equation is a Dyson equation within the subspace spanned by only single fluctuation states. Self-consistency is achieved through :

$$\begin{aligned} \mathbf{G}^{(R)} &= \left(\mathbf{G}_{VCA}^{-1} - \Sigma^{(R)} \right)^{-1} \\ \Sigma^{(R)} &= \sum_{R' R'' \neq R} \mathbf{K}'^{(R')} \mathbf{F}^{(R')(R'')} \mathbf{K}'^{(R'')} \end{aligned}$$

The above argument shows that unlike the usual CPA where only a single fluctuation at a site is considered, multiple fluctuations coming from multiple-scattering is present in the *itinerator* \mathbf{F} and therefore contribute to the self-energy Σ . However, the approximation described above means that correlated fluctuations between more than one site are present in neither the *itinerator* nor the self-energy. This is the main approximation involved in the ICPA.

We note that the ICPA is a self-consistent mean-field approximation for the self-energy which relates the configuration averaged Green function to the virtual crystal one. It is an approximation which maintains both the translational symmetry of the configuration average and its herglotz analytic properties. The ASR is an alternative technique for doing the same thing, namely obtaining an approximation to the self-energy maintaining the necessary properties of the exact case.

The recursion method addresses inversions of infinite matrices [Haydock 1980]. The average Green function in the augmented space formalism can be written as [Alam and

Mookerjee 2004] :

$$\ll \mathbf{G} \gg = \{1 | (\omega'^2 \hat{\mathbf{I}} - \widetilde{\mathbf{D}}_{eff})^{-1} | 1\}$$

Here

$$\begin{aligned} \omega'^2 &= \widehat{m} \omega^2 \\ \widetilde{\mathbf{D}}_{eff} &= (\widetilde{\mathbf{M}}^{-1/2} \widehat{m}^{1/2}) \widetilde{\mathbf{D}} (\widetilde{\mathbf{M}}^{-1/2} \widehat{m}^{1/2}) \\ |1\rangle &= (m_1^{-1/2} \widehat{m}^{1/2}) |\{\emptyset\}\rangle + (m_3^{-1/2} \widehat{m}^{1/2}) |\{R\}\rangle. \end{aligned}$$

Where $\widehat{m} = \ll m^{-1} \gg^{-1}$, $m_1^{-1/2} = \ll m^{-1/2} \gg$ and $m_3^{-1/2} = \sqrt{xy}((m_A^{-1/2} - m_B^{-1/2}))$. $\widetilde{\mathbf{M}}^{-1/2}$ and $\widetilde{\mathbf{D}}$ are given by Eqns. (3.7) and (3.10) of chapter (3).

Once a sparse representation of an operator in a Hilbert space, $\widetilde{\mathbf{D}}_{eff}$, is known in a countable basis, the recursion method obtains an alternative basis in which the operator becomes tridiagonal. This basis and the representations of the operator in it are found recursively through a three-term recurrence relation :

$$|u_{n+1}\rangle = \widetilde{\mathbf{D}}_{eff} |u_n\rangle - \alpha_n(\mathbf{k}) |u_n\rangle - \beta_n^2(\mathbf{k}) |u_{n-1}\rangle. \quad (4.5)$$

with the initial choice $|u_1\rangle = |\mathbf{k} \otimes \{1\}\rangle$ or and $\beta_1^2 = 1$. The recursion coefficients α_n and β_n are real and are obtained by imposing the ortho-normalizability condition of the new basis set as :

$$\begin{aligned} \alpha_n(\mathbf{k}) &= \frac{\{u_n | \widetilde{\mathbf{D}}_{eff} | u_n\}}{\{u_n | u_n\}} ; \quad \beta_{n+1}^2(\mathbf{k}) = \frac{\{u_n | \widetilde{\mathbf{D}}_{eff} | u_{n+1}\}}{\{u_n | u_n\}} \\ \text{and also } \{u_m | u_n\} &= 0 \text{ for } m \neq n, n \pm 1 \end{aligned}$$

Now, we use the augmented space theorem and repeated applications of the downfolding theorem on the tri-diagonal representation gives :

$$\begin{aligned} \ll \mathbf{G}(\mathbf{k}, \omega'^2) \gg &= \frac{1}{\omega'^2 - \alpha_1(\mathbf{k}) - \frac{\beta_2^2(\mathbf{k})}{\omega'^2 - \alpha_2(\mathbf{k}) - \frac{\beta_3^2(\mathbf{k})}{\ddots \frac{\beta_N^2(\mathbf{k})}{\omega'^2 - \alpha_N(\mathbf{k}) - \Gamma(\mathbf{k}, \omega'^2)}}}} \\ &= \frac{1}{\omega'^2 - \alpha_1(\mathbf{k}) - \Sigma'(\mathbf{k}, \omega'^2)} \end{aligned} \quad (4.6)$$

From the definition of the self-energy given earlier, it has been argued by us in an earlier communication that the disorder scattering induced lifetimes come entirely from the imaginary part of $\Sigma'(\mathbf{k}, \omega'^2)$. Here $\Gamma(\mathbf{k}, \omega'^2)$ is the asymptotic part of the continued fraction. The *approximation* involved has to do with the termination of this continued fraction. The method of such approximation has already been discussed in section (1.4) of chapter (1).

Both the ICPA and the ASR involve approximations of the self-energy. We have already discussed that in the ICPA, contributions of configurations involving correlated fluctuations in more than one site to the self-energy are ignored in the present case but it is capable of incorporating them. If we use the form of $\widetilde{\mathbf{D}}_{eff}$ in the recursion equations (4.5), it is immediately obvious that in the ASR, contributions of such correlated fluctuation states to the self-energy are present. We had earlier shown that such contributions occur first at β_4^2 for diagonal disorder and in α_2 in case of off-diagonal disorder. Ignoring such contributions will make all moments greater than or equal to eight to be non-exact for diagonal and three for off-diagonal disorder. The ICPA achieves accuracy through self-consistency in the subspace of single fluctuations in its present version, while the ASR achieves accuracy by increasing the number of recursions in the *full* augmented space and estimating the terminator to mimic the asymptotic part of the continued fraction as closely as possible. The two are very different algorithms. Both can take care of off-diagonal disorder and short-ranged order, but in those situations where clustering, either chemical or statistical, is important, the ASR, which takes into account correlated scattering from clusters, should be preferable over the single-fluctuation only version of the ICPA.

4.3 First principles calculations of force constants in alloys

As is clear from the above discussions that the crucial component in both the ASR and the ICPA is the alloy force constants. Due to the random chemical environment around each atom in a substitutionally disordered alloy, the force constants corresponding to A-A, B-B and A-B pairs in a A_xB_{1-x} alloy are different and in no way resembles the force constants in a completely ordered environment. In order to have significant accuracy in

calculated phonon properties one should, therefore, have accurate information on force constants corresponding to various pairs of chemical species. The only trustworthy source of force constant data is the first-principles calculation. To this end, we have employed first-principles Density functional perturbation theory (DFPT) to obtain force constants. The details about the DFPT and our approach to use it to extract random alloy force constants is discussed below.

4.3.1 Density functional perturbation theory

Density functional perturbation theory (DFPT) [Baroni *et al.* 2001] is a density functional theory (DFT) based linear response method to obtain the electronic and lattice dynamical properties in condensed matter systems. The dynamical matrix which provides information on lattice dynamics of the system can be obtained from the ground-state electron charge density and its linear response to a distortion of the nuclear geometry. In DFPT, this linear response is obtained within the framework of DFT. One of the greatest advantages of DFPT-as compared to other nonperturbative methods for calculating lattice dynamical properties of crystalline solids (such as the frozen-phonon or molecular dynamics spectral analysis methods) -is that within DFPT the responses to perturbations of different wavelengths are decoupled. This feature allows one to calculate phonon frequencies at arbitrary wavevectors avoiding the use of supercells and with a workload that is independent of the phonon wavelength.

4.3.2 Random alloy force constants from DFPT

Since there is no first-principles theory for lattice dynamics in random alloys available we took recourse to calculate force constants for ordered structures which can suitably mimic the random alloy using DFPT. However, for a proper representation for the random alloy, one needs to work with a large supercell which prohibits the use of DFPT from a practical point of view. The other approach would have been to construct a set of ordered structures having the same composition of the alloy under investigation, run first-principles calculation on each of them and average the data appropriately. As a first approximation to this approach, here we have done DFPT calculations on a single

ordered structure and used the resultant force constants as approximate random alloy force constants as inputs to the ICPA and the ASR. The alloy chosen is FePd. The reason for choosing the FePd system is twofold: first, the ICPA and the ASR were applied only for the NiPt and NiPd alloys where the constituents of the alloys have face-centred cubic structure in their elemental phases. In case of FePd, although the alloy in the disordered phase is face centred cubic but Fe is body centred cubic in its elemental phase. It was therefore interesting to test the suitability of both the approximations in case of such a system where one of the constituents forming the alloy has a different structure than the alloy itself in its elemental phase. Second, inelastic neutron scattering data was available for Fe₅₀Pd₅₀ alloy [Mahaddene *et al* 2004]. It would therefore have been possible to compare the ICPA and the ASR results with the experimental data directly enabling the understanding of the nature of interactions between various pairs of species in the random phase. Since the Fe₅₀Pd₅₀ forms a face centred cubic (fcc) solid solution, we have chosen the prototype tetragonal L1₀ structure with c/a ratio equal to unity to be used for first-principles calculations.

4.3.3 Details of first-principles calculations

We use DFPT within the local-density-approximation (LDA) to compute the force constants for the FePd equiatomic composition single ordered structure mentioned above. The experimental lattice constant $a = 7.24$ a.u. is used in the calculations. We employ a plane-wave pseudopotential implementation of the DFPT with Perdew-Zunger parametrization of the LDA [Perdew and Zunger 1981] as done in the Quantum-Espresso package. Ultrasoft pseudopotentials [Vanderbilt 1990] with non-linear core correction [Louie *et al* 1982] are used for Fe and Pd. The kinetic energy cut-off is taken to be 35 Ry. The Brillouin-zone integrations are carried out with Methfessel-Paxton smearing [Methfessel and Paxton 1989] using a $10 \times 7 \times 7$ \mathbf{k} -point mesh, which corresponds to 120 \mathbf{k} -points in the irreducible wedge. The value of the smearing parameter is 0.1 Ry. These parameters are found to yield phonon frequencies converged to within 5 cm^{-1} .

Once adequate convergence is achieved for the electronic structure, the phonon force constants are obtained using the linear response. Within DFPT, the force constants are

conveniently computed in reciprocal space on a finite \mathbf{q} -point grid and Fourier transformation is employed to obtain the real-space force constants. The number of unique real-space force constants and their accuracy depend upon the density of the \mathbf{q} -point grids: the closer the \mathbf{q} -points are spaced, the accurate the force constants are. In this work, the dynamical matrix is computed on a $6 \times 6 \times 4$ \mathbf{q} -point mesh commensurate with the \mathbf{k} -point mesh.

4.4 Results and Discussions

In Table 4.1 we report the nearest-neighbor force constants for the artificial ordered structure A-B obtained from first-principles as described above. Subsequently, we use these

Table 4.1: Real-space nearest neighbor force constants for $\text{Fe}_{50}\text{Pd}_{50}$ obtained by DFPT calculations on the artificial ordered structure. The units are dyn cm^{-1} .

Pair	Force constant	Direction
Fe-Fe	-9458	$1xx$
Fe-Pd	-9458	$1xx$
Pd-Pd	-28974	$1xx$
Fe-Fe	-6005	$1xy$
Fe-Pd	-10755	$1xy$
Pd-Pd	-30372	$1xy$
Fe-Fe	1800	$1zz$
Fe-Pd	-114	$1zz$
Pd-Pd	3555	$1zz$

force constants as inputs to the ICPA and the ASR calculations. Figure (4.1) shows the corresponding dispersion curves. The results clearly show that the force constants for the artificial ordered structure are not adequate to describe the lattice dynamics for the disordered $\text{Fe}_{50}\text{Pd}_{50}$ system. In both the ICPA and the ASR, the high frequency phonons are poorly represented for all three symmetry directions. On top of that, the high frequency branches suffer a split for large q values, a feature not observed in the experiments. All these features point to the fact that the force constants used in the ICPA and the ASR calculations completely fail to capture the complexities of the force-constant disorder in

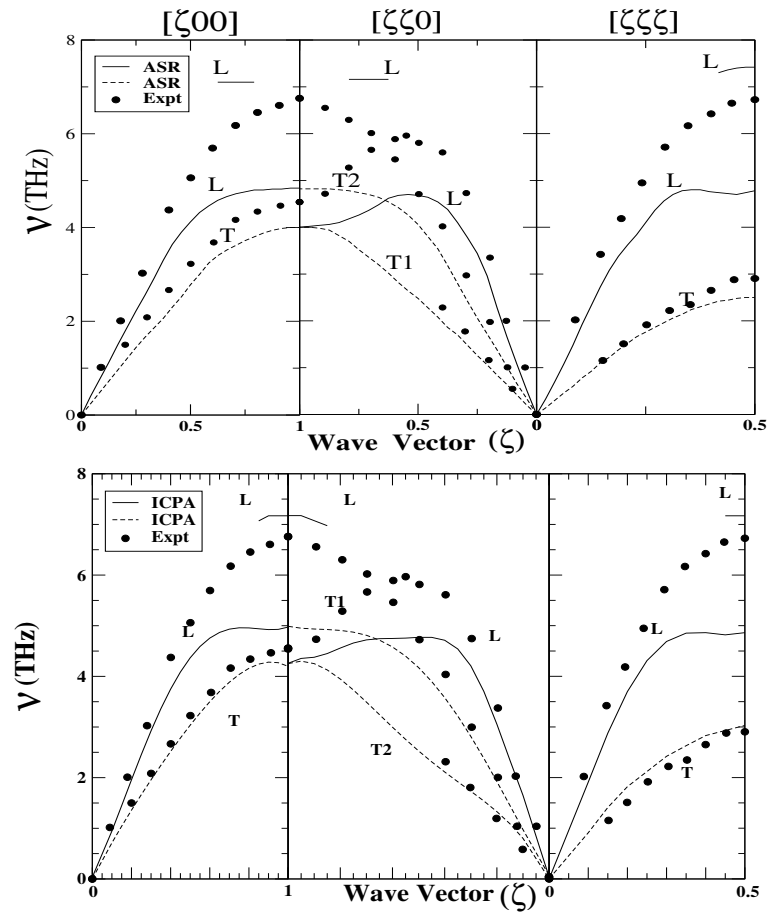


Figure 4.1: Dispersion Curves (frequency ν vs. reduced wave vector ζ) for $\text{Fe}_{50}\text{Pd}_{50}$ alloy. The upper panel corresponds to the ASR results however the lower panel to the ICPA results. The filled circles are the experimental data Mahaddene *et al* 2004. The force constants used are given in Table 4.1.

a random environment. This is quite understandable as we have used a crude approximation for the force constants in random environment. One single ordered structure, in no way, can mimic the randomness in the environment around a given chemical species. The fact that the force constants obtained on this artificial structure are responsible for the disagreement with the experiment is corroborated by the coherent structure factors, particularly at high q values as demonstrated in Figure (4.2) where coherent structure factors for certain high q values, obtained by the ICPA, are displayed. The curves clearly show that the spurious high frequency peak is due to the Pd-Pd pairs and to a smaller

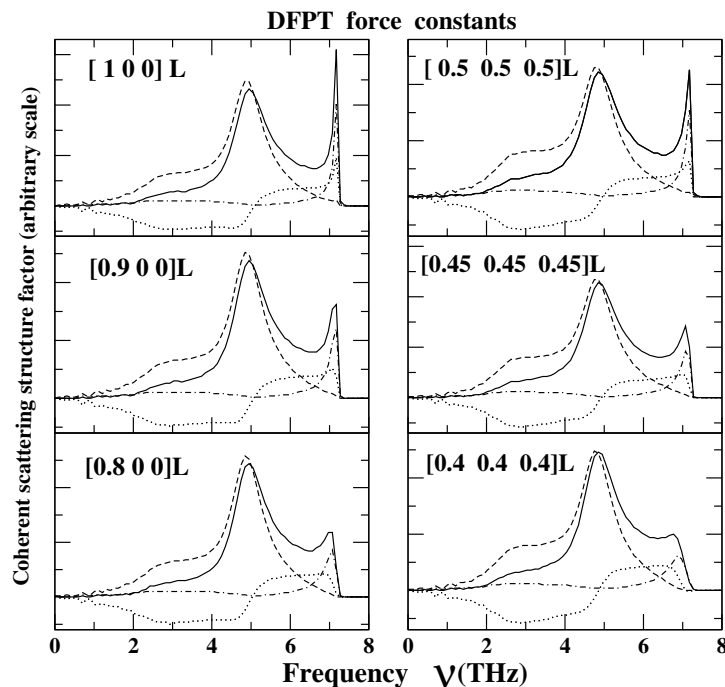


Figure 4.2: Partial and total structure factors calculated in the ICPA for various ζ -values along the $[\zeta, 0, 0]$ and $[\zeta, \zeta, \zeta]$ directions in $\text{Fe}_{50}\text{Pd}_{50}$ alloy. The solid line are the total contribution, the dotted lines are the Fe-Pd spectra, the long-dashed lines are the Fe-Fe spectra, and the dot-dashed lines are the Pd-Pd contributions. The type of mode is labelled along a particular symmetry direction. The force constants used are given in Table 4.1. The details are given in the text.

extent due to Fe-Pd pairs. As is seen from Table 4.1, the Fe-Fe and Pd-Pd force constants differ by about 70 %, thereby representing a situation of very strong disorder as is seen in the case of $\text{Ni}_{50}\text{Pt}_{50}$ [Ghosh *et al* 2002]. The splitting of the high frequency branch is a manifestation of this strong force-constant disorder, albeit wrong in the present case.

In the pursuit of the correct set of force constants for the system so that the suitability of the ICPA and the ASR can be properly tested, we then used the force constant data as reported in the experiment [Mahaddene *et al* 2004]. However, the force constant data reported in the experiment was obtained by fitting the frequencies to a Born-Von-Karman force constant model. Also, the frequencies were obtained from neutron-scattering data on ordered L10 structure at 860K, very close to the order-disorder transition temperature 950K. The reason behind using the experimental force constants obtained from an ordered

L10 structure for disordered calculations were twofold: first, the L10 force constants should be a better approximation for random alloy force constants than the artificial cubic structure ones because the L10 structure allows structural relaxation and therefore a variation in the bond distances between different chemical species pairs although in a restricted way. Nevertheless, this restricted degree of relaxation could be crucial in capturing the nature of forces between various chemical species as has been seen in case of NiPt alloys [Ghosh *et al* 2004]. Second, since the L10 data was taken at 860K and the disordered fcc data was taken at 1020K, both of them lie very close to the order-disorder transition temperature. At a first-order order-disorder transformation at finite temperatures, the ordered phase is only partially ordered and the disordered phase is in equilibrium with, has short-range order. Examination of the correlation functions has shown that ordered and disordered states rather show similar atomic arrangement in the vicinity of the order-disorder transformation. It is therefore expected that in the present case, the L10 force constants at 860K would not change significantly in the disordered phase at 1020K. These intuitive arguments are well supported by the dispersion curves presented in Figure (4.3). Both the ICPA and the ASR results agree reasonably well with the experimental data. The spurious splitting obtained earlier disappears. This disappearance can be understood better if we look at the force constants used for this calculation. Table 4.2 lists the experimental force constants used as inputs for the ICPA and the ASR calculations. In comparison with DFPT values, the Pd-Pd force constants are a lot softer and the Fe-Pd force constants harden. The fact that the force constants and their behavior is indeed the deciding factor is again exemplified by the coherent structure factors for the selected high q vectors as shown in Figure (4.4). The figures show that the single high frequency peak is now mostly because of the Fe-Fe and Fe-Pd contributions, rather than the Pd-Pd contribution. This points to the fact that the Pd-Pd contribution was overestimated and the Fe-Fe and the Fe-Pd contributions were grossly underestimated by the DFPT calculations on the artificial cubic structure because of the lack of relaxation in such structure. This in turn can be understood by looking at the bond distances between various pairs of species. In the cubic structure, the Fe-Fe, Pd-Pd and the Fe-Pd distances were same and in the present case was taken to be 5.12 a.u. The L10 structure at 860 K, on the other hand, had Fe-Fe and Pd-Pd distances to be 5.25

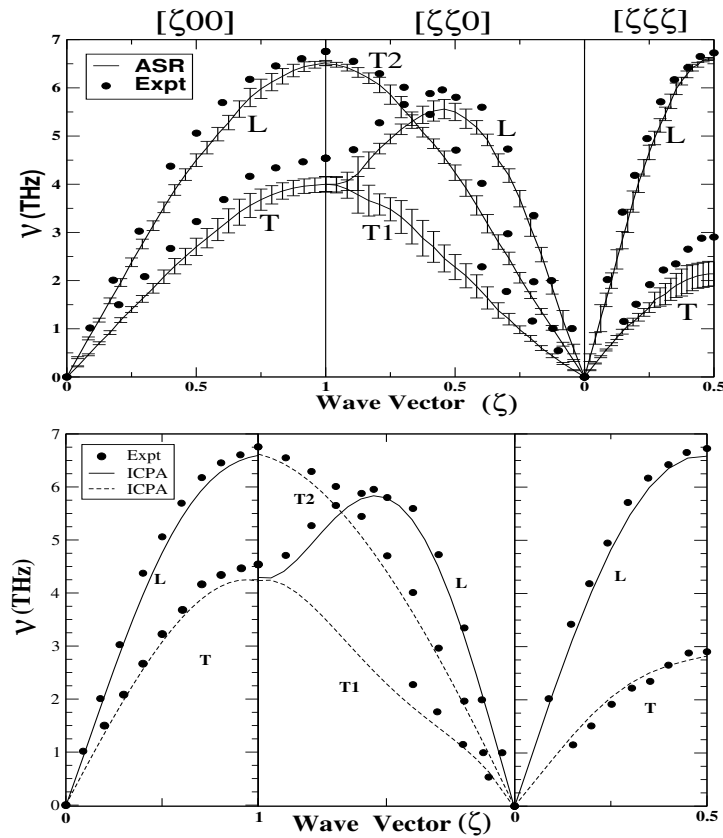


Figure 4.3: Dispersion Curves (frequency ν vs. reduced wave vector ζ) for $\text{Fe}_{50}\text{Pd}_{50}$ alloy. The upper panel corresponds to the ASR results however the lower panel to the ICPA results. The filled circles are the experimental data Mahaddene *et al* 2004. The error bar in the ASR result basically represents the full widths at half maxima (FWHM) at various ζ values. The force constants used are given in Table 4.2.

a.u. and the Fe-Pd distances to be 5.08 a.u. Thus, the Pd atoms, in the artificial cubic structures, were made to vibrate in a smaller volume and because of the smaller distance between two like atoms, the Pd-Pd force constants became harder.

Figure (4.5) compares the ICPA and the ASR results for the phonon densities of states. Both the approximations produce identical features. The peaks and the band edges have quantitative agreement among themselves and with the experimental results [Mahaddene *et al* 2004].

Figure (4.6) displays the Full width at half maxima (FWHM) data associated with the finite lifetimes of phonons due to disordered scattering. The upper three panels show the

Table 4.2: Real-space nearest neighbor force constants for $\text{Fe}_{50}\text{Pd}_{50}$ obtained from experimental data Mahaddene *et al* 2004 on L10 structure at 860K. The units are dyn cm^{-1} .

Pair	Force constant	Direction
Fe-Fe	-5650	$1xx$
Fe-Pd	-14050	$1xx$
Pd-Pd	-19450	$1xx$
Fe-Fe	-9750	$1xy$
Fe-Pd	-16550	$1xy$
Pd-Pd	-22350	$1xy$
Fe-Fe	4100	$1zz$
Fe-Pd	2500	$1zz$
Pd-Pd	2900	$1zz$

widths as a function of wave vector (ζ) along the three symmetry directions extracted from the ASR method, however the lower three panels show the ICPA results. The FWHM is a more sensitive test for the underlying approximation than the dispersion curves. The ICPA and the ASR have reasonable agreement regarding FWHM's although quantitative agreement is not there because of the different nature of the two approximations. Unfortunately, the experimental group didn't perform a phonon life-time measurement so that the FWHM's calculated theoretically could be compared with the experiments.

In Fig. (4.7), we have shown the total coherent structure factors at various ζ values along the three symmetry directions with various modes of vibrations. The upper box shows ASR result however the lower ICPA result. In both the cases, the different curves for different ζ values are shifted along the x-axis in order to facilitate vision. One can easily notice the difference in the nature of curves arising out of two different methodologies. In ASR result, we have found three classes of degenerate modes, these are (1) T1 and T2 modes along $[\zeta 00]$ directions (2) L and T1 modes along $[\zeta \zeta 0]$ directions and (3) all the three modes along $[\zeta \zeta \zeta]$ directions. However in ICPA case, all the modes along different directions are non-degenerate. The difference in the two kinds of results are due to the different structure and way of calculations in the two methodologies. However the ultimate

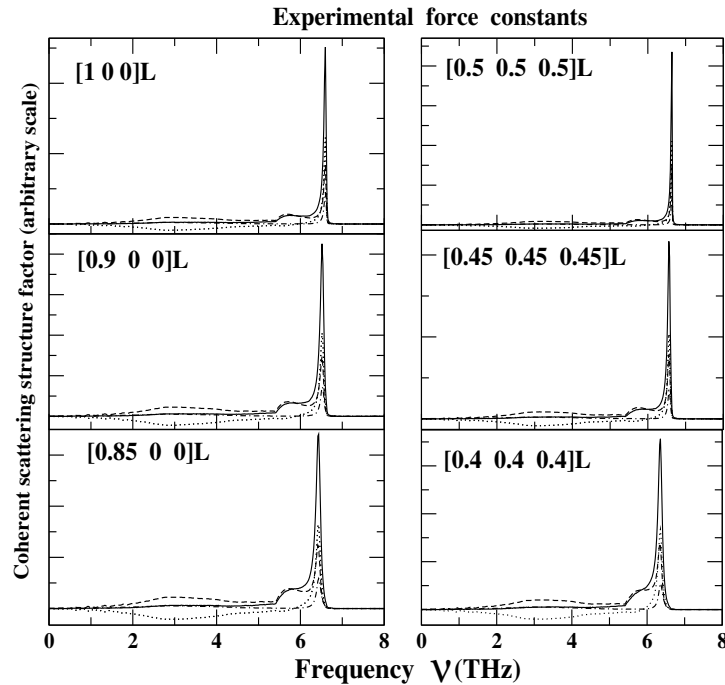


Figure 4.4: Same as Fig. 4.2 but with the force constants of Table 4.2. Other details are given in the text.

dispersion curves and FWHM's came out from two different methodologies are reasonably well comparable, which are the actual vibrational quantities to look at in any disordered alloy.

4.5 CONCLUSIONS

This chapter has continued the development of the Augmented space recursion for studying the vibrational properties of disordered metallic alloys. A brief description of the method combined with a first-principles calculation (the so called DFPT) of the dynamical matrices has been reported. The power of the approach has been illustrated by explicit calculations for the $\text{Fe}_{50}\text{Pd}_{50}$ system.

In addition, we have shown in this chapter that the two theories ICPA and ASR are unique and systematic in the sense that they produce almost identical results for a particular system. Both the theories can explicitly take into account the fluctuations in masses,

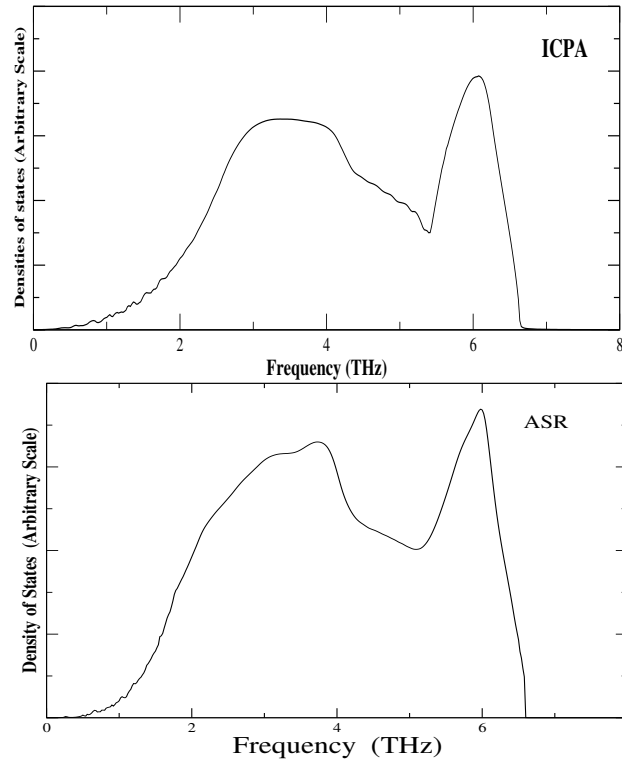


Figure 4.5: Phonon density of states for $\text{Fe}_{50}\text{Pd}_{50}$ alloy. The upper and lower panel shows ICPA and ASR results respectively. The force constants used are that of experiment given in Table 4.2.

force constants and scattering lengths. We propose the methods as computationally fast and accurate techniques for the study of lattice dynamics of disordered alloys. A correct quantitative trend (compareable to the experimental result) of the phonon dispersion and the phonon density of states has been predicted by both the methodologies when the experimental force constants has been used in the calculation. Off-course there is a fairly obvious general comment to be made with regard to the self consistency of the procedure. This is precisely the reason that a first-principles estimate of the dynamical matrices on parent ordered alloys do not yield quantitatively accurate results (in comparison with the experiment) for the disordered alloy. We shall propose that we need to go beyond and estimate the dynamical matrices from a model of embedded atoms in a fully disordered back ground.

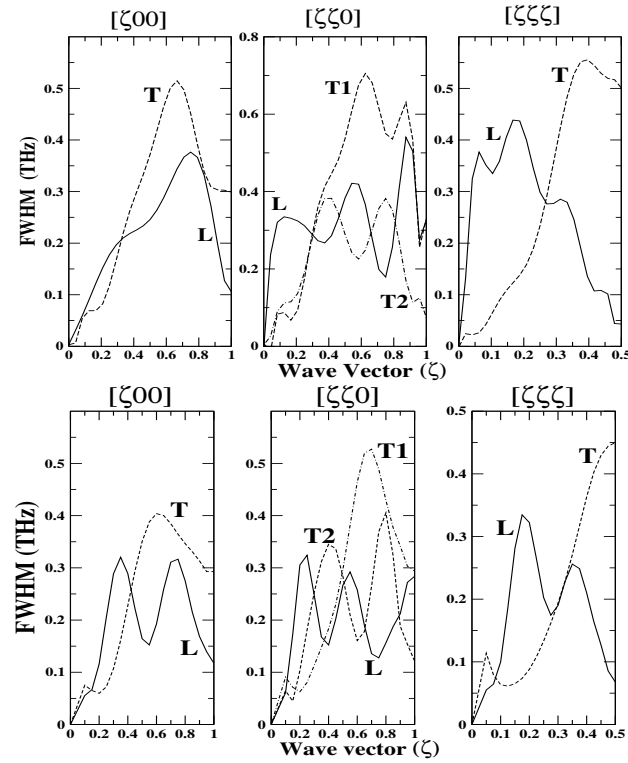


Figure 4.6: Disorder-induced FWHM's vs wave vector (ζ) for $\text{Fe}_{50}\text{Pd}_{50}$ alloy. The upper and lower panels show ASR and ICPA results respectively. The force constants used are given in Table 4.2.

Chapter 5

Inelastic neutron scattering in random binary alloys

5.1 Introduction

In the last chapter we have set up a methodology for the calculation of configurationally averaged density of states for phonons in disordered binary alloys and have applied it to three carefully chosen alloy systems to illustrate the interplay between diagonal and off-diagonal disorder. All the physical quantities discussed in that chapter like the dispersion relations and line widths for phonons can be measured directly through *coherent inelastic neutron scattering*. Information about the phonon density of states can be extracted from the *incoherent inelastic neutron scattering cross sections*. Over the past few years, numerous experimental studies [Tsunoda *et al* 1979, Svensson *et al* . 1967, Nicklow *et al* . 1968 and others, Kamitakahara and Brockhouse, 1974, R. M. Nicklow 1983] of the lattice dynamics of disordered systems have been carried out providing insight into the nature of their elementary excitations. However the theoretical counter part is still unsatisfactory. The theory of scattering of thermal neutrons with disordered alloys is not a trivial problem in the sense that it requires two basic inputs : first is the formulation of the problem and the second it's actual numerical implementation in realistic situations. As far as the formulation part is concerned, several authors have attempted the problem with different approaches. However their actual numerical implementation in realistic systems still remains sketchy beyond the simple single site mean field theories. Quite some time ago, Nowak and Dederichs 1982 discussed the separation of the coher-

⁰The contents of this chapter has been published in the paper : Aftab Alam and A Mookerjee, *Phys. Rev. B* **71**, 094210 (2005).

ent and incoherent parts of the total inelastic scattering intensity by using the scattering diagrammatic technique within the single site coherent potential approximation (CPA). According to their approach the incoherent part of the total scattering intensity is the sum of all irreducible diagrams containing only short ranged correlations. The coherent part on the other hand may be expressed as a product of the usual configuration averaged Green function and the square of an effective scattering length, which is itself given by the irreducible diagrams closely related to those for the self energy. It has been known for some time that the single site CPA cannot adequately deal with intrinsic off-diagonal disorder of the force constants in the problem of phonon excitations in random alloys. This was evidenced in the inability of the single site CPA to explain experimental lifetime data on NiPt [Tsunoda *et al* 1979]. Nor can it adequately deal with the correlated diagonal and off-diagonal disorder induced by the force constant sum rule. Several successful attempts have been made to go beyond the CPA. These include, among others, approximations based on the augmented space formalism (Mookerjee 1973) : the traveling cluster approximation (TCA) [Kaplan and Mostoller 1974, Kaplan and Gray 1981, Mills and Ratnavararaksha 1978, Kaplan *et al* 1980], the Cluster-CPA [Srivastava *et al* 1982, Mookerjee *et al* 1983], the itinerant cluster approximation (ICPA) Ghosh *et al* 2002 and the augmented space recursion (ASR) Alam and Mookerjee 2004.

In this chapter we shall tackle a two-fold problem : one of formulation and the other of implementation in real alloy systems. We shall use a scattering diagram technique also based on the augmented space formalism [Mookerjee 1975, Mookerjee 1976] to suggest how to separate the coherent and incoherent parts of the total inelastic scattering cross-section for a disordered binary alloy in a way mirroring the ideas of Nowak and Dederichs, but this will be done without taking any recourse to mean-field like approximations. For implementation in real alloy systems, we shall suggest the ASR for the evaluation of scattering cross sections. But instead of doing an ordinary recursion, we shall perform a *Block recursion* in order to calculate the off diagonal entries of the Green matrix, since the expressions for the scattering cross sections in our formalism require the contribution of off-diagonal Green's function. The approximation introduced within this formalism will maintain the essential analytic properties of the Green function, deal with off-diagonal disorder and the sum rule without any further simplifications or assumptions

and encompass environmental effects over an extended neighbourhood. This is the major contribution of this particular work.

5.2 The Formulation

In the previous chapter (3), we had derived an expression for the configuration averaged Green matrix [Eqn. (3.11)] as :

$$\ll \mathbf{G}(R, R', \omega^2) \gg = \langle \{\emptyset\} \otimes R | (\widetilde{\mathbf{M}} \omega^2 - \widetilde{\mathbf{D}})^{-1} | \{\emptyset\} \otimes R' \rangle. \quad (5.1)$$

The above expression is in terms of the real space basis, where

$$\begin{aligned} \widetilde{\mathbf{M}} &= \mathbf{A}(\mathbf{m}) \mathbf{I} \otimes \mathbf{I} + \mathbf{B}(\mathbf{m}) \sum_R \mathbf{p}_R^\downarrow \otimes \mathbf{P}_R + \mathbf{F}(\mathbf{m}) \sum_R \mathbf{T}_R^{\uparrow\downarrow} \otimes \mathbf{P}_R \\ &= \ll \widetilde{\mathbf{M}} \gg + \widetilde{\mathbf{M}}'. \end{aligned} \quad (5.2)$$

$$\begin{aligned} \widetilde{\mathbf{D}} &= - \sum_R \left\{ \sum_{R' \neq R} \Psi_{RR'}^{\alpha\beta} \right\} \otimes \mathbf{P}_R + \sum_{RR'} \Psi_{RR'}^{\alpha\beta} \otimes \mathbf{T}_{RR'} \\ &= \ll \widetilde{\mathbf{D}} \gg - \sum_R \left\{ \sum_{R' \neq R} \Lambda_{RR'}^{\alpha\beta} \right\} \otimes \mathbf{P}_R - \sum_{RR'} \Lambda_{RR'}^{\alpha\beta} \otimes \mathbf{T}_{RR'} \\ &= \ll \widetilde{\mathbf{D}} \gg + \widetilde{\mathbf{D}}' \end{aligned} \quad (5.3)$$

with

$$\begin{aligned} \Lambda_{RR'} &= \mathbf{D}_{RR'}^{(1)} (\mathbf{p}_R^\downarrow + \mathbf{p}_{R'}^\downarrow) + \mathbf{D}_{RR'}^{(2)} (\mathbf{T}_R^{\uparrow\downarrow} + \mathbf{T}_{R'}^{\uparrow\downarrow}) + \mathbf{D}_{RR'}^{(3)} \mathbf{p}_R^\downarrow \mathbf{p}_{R'}^\downarrow \\ &\quad + \mathbf{D}_{RR'}^{(4)} (\mathbf{p}_R^\downarrow \mathbf{T}_{R'}^{\uparrow\downarrow} + \mathbf{T}_R^{\uparrow\downarrow} \mathbf{p}_{R'}^\downarrow) + \mathbf{D}_{RR'}^{(5)} \mathbf{T}_R^{\uparrow\downarrow} \mathbf{T}_{R'}^{\uparrow\downarrow} \end{aligned} \quad (5.4)$$

where

$$\begin{aligned} \mathbf{D}^{(1)} &= (y - x) \Phi_{(1)}, \\ \mathbf{D}^{(2)} &= \sqrt{xy} \Phi_{(1)}, \\ \mathbf{D}^{(3)} &= (y - x)^2 \Phi_{(2)}, \\ \mathbf{D}^{(4)} &= \sqrt{xy} (y - x) \Phi_{(2)}, \\ \mathbf{D}^{(5)} &= xy \Phi_{(2)}. \end{aligned}$$

and

$$\begin{aligned}\Phi_{(1)}^{\alpha\beta} &= x \Phi_{AA}^{\alpha\beta} - y \Phi_{BB}^{\alpha\beta} + (y - x) \Phi_{AB}^{\alpha\beta} \\ \Phi_{(2)}^{\alpha\beta} &= \Phi_{AA}^{\alpha\beta} + \Phi_{BB}^{\alpha\beta} - 2\Phi_{AB}^{\alpha\beta}\end{aligned}$$

The *virtual crystal* (VCA) Green matrix is

$$\mathbf{g}(R, R', \omega^2) = \langle \{\emptyset\} \otimes R | (\ll \tilde{\mathbf{M}} \gg \omega^2 - \ll \tilde{\mathbf{D}} \gg)^{-1} | \{\emptyset\} \otimes R' \rangle$$

where

$$\ll \tilde{\mathbf{M}} \gg = \ll m \gg \mathbf{I} \otimes \mathbf{I}.$$

Using Eqs. (5.2) and (5.4), we get

$$\begin{aligned}\ll \mathbf{G}(R, R', \omega^2) \gg &= \langle \{\emptyset\} \otimes R | (\ll \tilde{\mathbf{M}} \gg \omega^2 - \ll \tilde{\mathbf{D}} \gg + \tilde{\mathbf{M}}' \omega^2 - \tilde{\mathbf{D}}')^{-1} | \{\emptyset\} \otimes R' \rangle \\ &= \langle \{\emptyset\} \otimes R | (\mathbf{g}^{-1} - \tilde{\mathbf{D}}_1)^{-1} | \{\emptyset\} \otimes R' \rangle\end{aligned}\quad (5.5)$$

where we define

$$\tilde{\mathbf{D}}_1 = \sum_R \left\{ -\mathbf{\Upsilon}_R - \sum_{R' \neq R} \mathbf{\Lambda}_{RR'} \right\} \otimes \mathbf{P}_R + \sum_R \sum_{R' \neq R} \mathbf{\Lambda}_{RR'} \otimes \mathbf{T}_{RR'}$$

with

$$\mathbf{\Upsilon}_R = \mathbf{B}(\mathbf{m}) \omega^2 \mathbf{p}_R^\downarrow + \mathbf{F}(\mathbf{m}) \omega^2 \mathbf{T}_R^{\uparrow\downarrow}.$$

Let us discuss in brief the superiority of our approach as compared to the previous theories. The coherent potential approximation has been one of the most successful approximations for the calculation of the configuration averaged Green functions for disordered alloys. However, it is a single site approximation and is unable to deal with the intrinsic off-diagonal disorder in phonon problems. In the early 70s there had been several attempts to generalize the single site CPA to the so-called bond CPAs (W Shiba 1971, Brouers *et al.* 1973). These bond CPAs have serious drawbacks in the sense that they did not reproduce the dilute limit accurately. This has been discussed by Elliot *et al.* 1974. For example, when a B atom sits on a site in a randomly occupied lattice, all the bonds that emanate from it are correlated in the sense that they can either be of the type BA or BB depending upon the occupation of the site at the other end of the bond. These

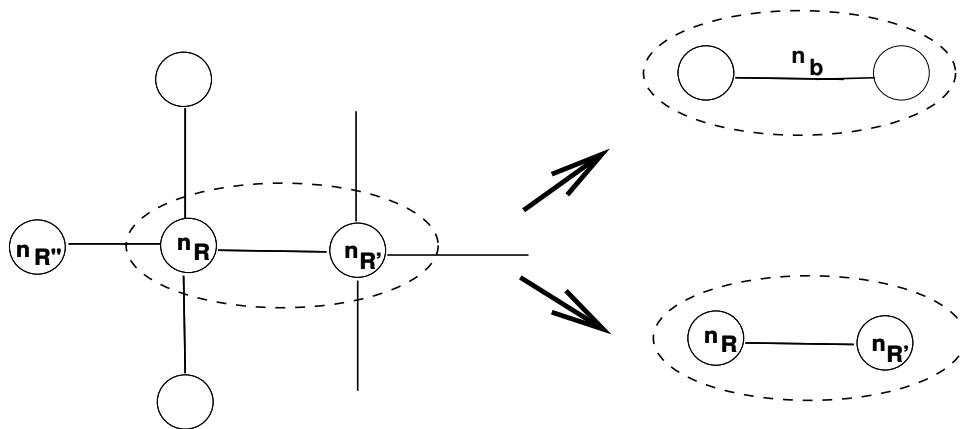


Figure 5.1: Bond coherent potential approximations

correlations between bonds emanating from a site are important at all concentrations. Let us see what a bond CPA does :

The left hand side of Fig. (5.1) shows a lattice whose sites are randomly occupied. The various bond CPAs fall into two categories :

- (1) The first category concentrates on one bond, replaces the randomness of the end-points by a binary “bond occupation” variable n_b . It replaces the rest of the solid by an average medium obtained self-consistently by requiring that the scattering from this bond is zero on the average.
- (2) The second category again isolates a single bond and considers it to have a trimodal distribution V_{AA}, V_{BB} or V_{AB} . It also replaces the rest of the solid by an average medium which is obtained through a similar CPA-like argument.

In both these approaches, the single bond is taken out of all the bonds emanating from a site. The correlations between this and the other bonds which share a corner with it gets lost in the approximation. Either of these approaches have the serious drawback discussed by the review article by Elliot *et al* . 1974.

Our approach for calculating the configuration averaged Green function is quite different. We start with the exact expression of equation (5.5) and carry out recursion (Haydock *et al* 1972) starting from an initial state. Our model may be schematically shown in figure (5.2). The correlations between bonds ending at a site is *explicit*. In

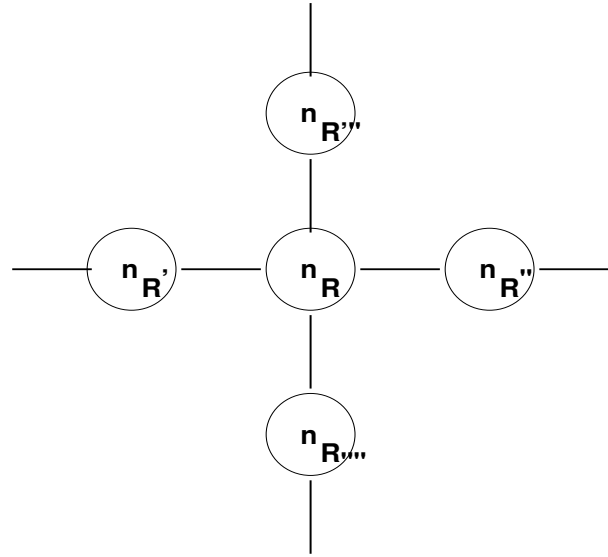


Figure 5.2: Our model, where the correlation between bonds arises because of the common vertex which is random

addition the correlation between the diagonal element of the dynamical matrix and the off-diagonal elements is also explicitly taken. As we carry out the recursion step by step, we include joint fluctuations of the bonds terminating at the central site. The action of the Hamiltonian on a recursion “state” in augmented k-space is as follows :

- (a) Flipping configuration from \uparrow to \downarrow or vice versa at the central site or one of its neighbours.
- (b) Flipping configurations from \uparrow to \downarrow or vice versa one at the central site and one at one of its neighbours.
- (c) Translating the configuration pattern by a lattice vector.

We start with a “average” state with \uparrow at all sites. As the recursion steps proceed, configuration fluctuations are generated on various sites. All configurations of the central site and its neighbours are generated as we carry out the recursion step by step. Consequently, from the way we have set up our random dynamical matrix, all the correlated configurations of the bonds emanating from the central site are taken into account.

The asymptotic part of the continued fraction is replaced by an analytic terminator (either that proposed by Luchini and Nex or Beer and Pettifor). This terminator is deduced from the initial recursion coefficients. *This is the approximation made on the exact expression of equation (5.5).* If we carry on recursion exactly up to 8 steps, 16 moments of the density of states are exactly reproduced and the analytic terminator also ensures that the asymptotic moments are accurate. This is certainly way beyond the accuracy of the bond CPAs of the type introduced by Brouers *et al.* 1973.

5.3 A generalized multiple scattering diagram approach

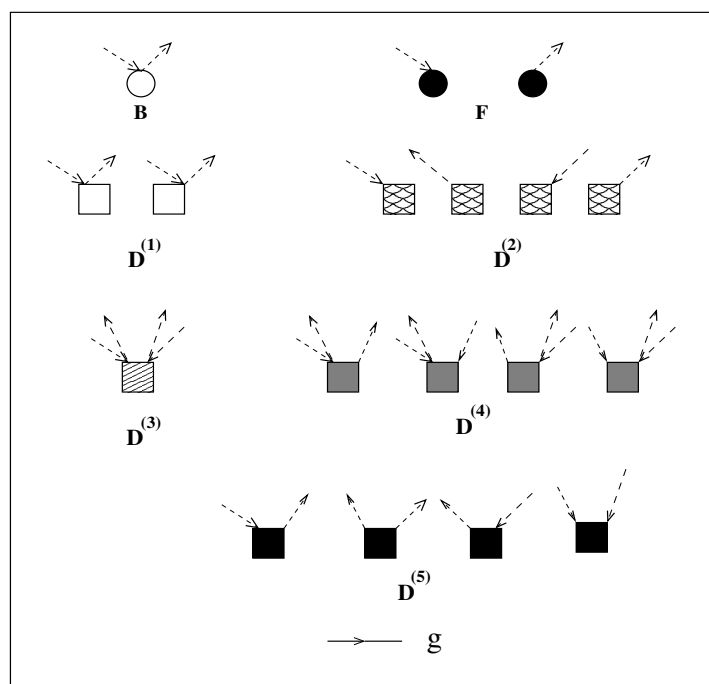


Figure 5.3: The scattering vertices for the averaged Green function

In this section we shall start from Eqn. (5.5) and develop a multiple scattering picture based on this. The idea is very similar to that of Edwards and Langer [Edwards 1958, Langer 1960] in the context of purely diagonal disorder. We shall first expand Eqn.(5.5) as follows :

$$\ll \mathbf{G}(R, R', w^2) \gg = \langle \{\emptyset\} \otimes R | \left(\mathbf{g} + \mathbf{g} \widetilde{\mathbf{D}}_1 \mathbf{g} + \mathbf{g} \widetilde{\mathbf{D}}_1 \mathbf{g} \widetilde{\mathbf{D}}_1 \mathbf{g} + \dots \right) | \{\emptyset\} \otimes R' \rangle \quad (5.6)$$

Let us discuss very briefly how one generates the scattering diagrams. The first term in Equation (5.6) gives :

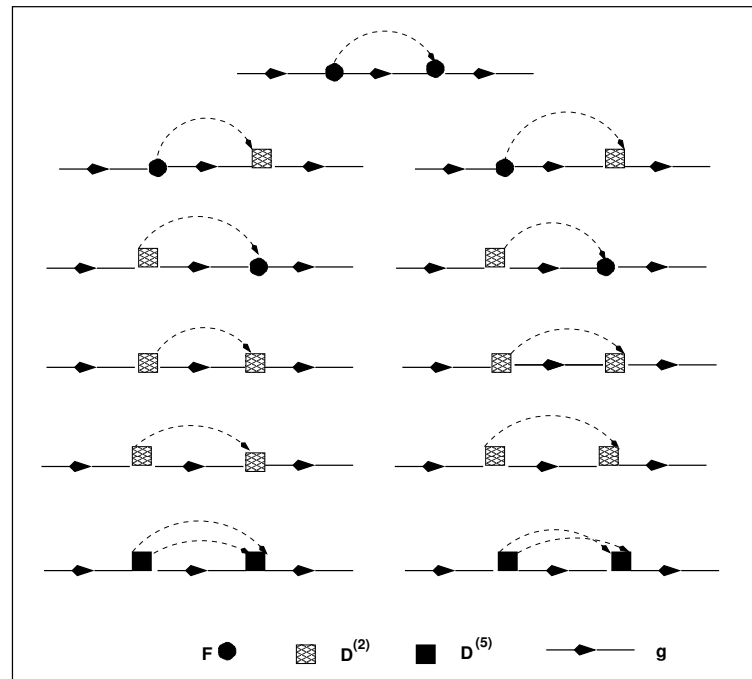
$$\langle \{\emptyset\} \otimes R | \mathbf{g} | \{\emptyset\} \otimes R' \rangle = \mathbf{g}(R, R', \omega^2) \quad (5.7)$$

The second term yields zero since $\langle \{\emptyset\} \otimes R | \widetilde{\mathbf{D}}_1 | \{\emptyset\} \otimes R' \rangle = 0$. The third term gives :

$$\begin{aligned} & \sum_{S' S''} \sum_{S''' S''''} \sum_{\{C\}} \sum_{\{C'\}} \langle \{\emptyset\} \otimes R | \mathbf{g} | \{\emptyset\} \otimes S' \rangle \langle \{\emptyset\} \otimes S' | \widetilde{\mathbf{D}}_1 | \{C\} \otimes S'' \rangle \\ & \langle \{C\} \otimes S'' | \mathbf{g} | \{C'\} \otimes S''' \rangle \langle \{C'\} \otimes S''' | \widetilde{\mathbf{D}}_1 | \{\emptyset\} \otimes S'''' \rangle \langle \{\emptyset\} \otimes S'''' | \mathbf{g} | \{\emptyset\} \otimes R' \rangle \end{aligned}$$

A little algebra yields the following contribution :

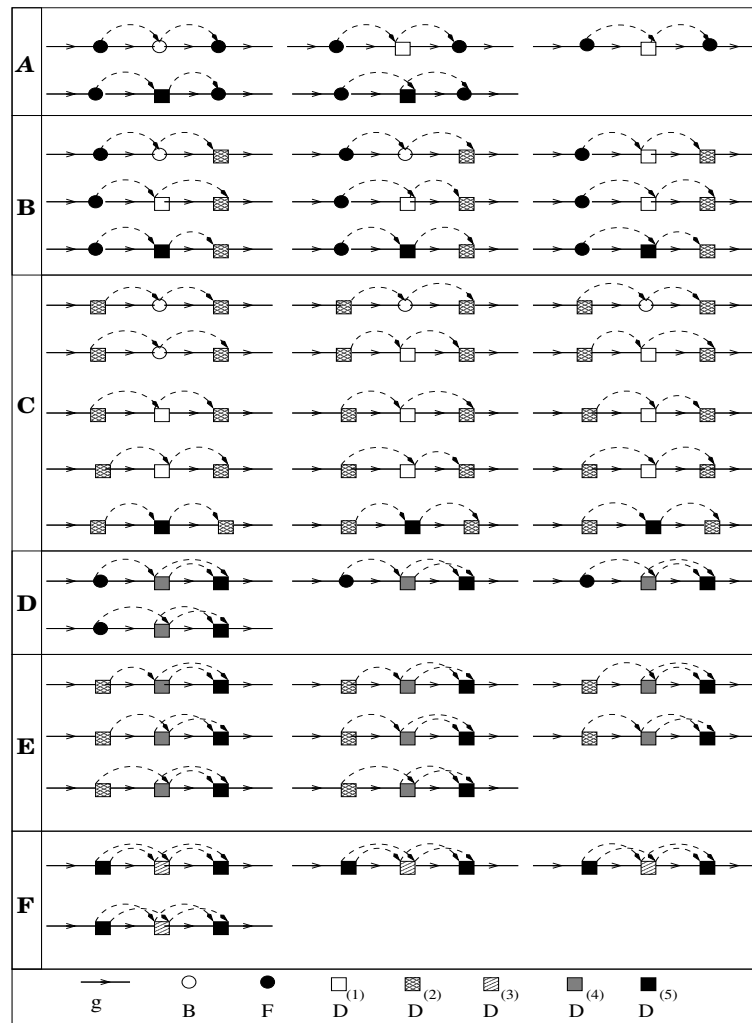
$$\begin{aligned} & \langle \{\emptyset\} \otimes R | \mathbf{g} \widetilde{\mathbf{D}}_1 \mathbf{g} \widetilde{\mathbf{D}}_1 \mathbf{g} | \{\emptyset\} \otimes R' \rangle = \\ & \sum_{S_1 S_2} \mathbf{g}(R, S_1, w^2) (\mathbf{F}w^2) \mathbf{g}(S_1, S_2, w^2) \delta(S_1 - S_2) (\mathbf{F}w^2) \mathbf{g}(S_2, R', w^2) + \\ & \sum_{S_1} \sum_{S_3 S_4} \mathbf{g}(R, S_1, w^2) (\mathbf{F}w^2) \mathbf{g}(S_1, S_3, w^2) \delta(S_1 - S_3) \Delta_{S_3 S_4}^{(2)} \mathbf{g}(S_4, R', w^2) + \\ & \sum_{S_1} \sum_{S_3 S_4} \mathbf{g}(R, S_1, w^2) (\mathbf{F}w^2) \mathbf{g}(S_1, S_3, w^2) \delta(S_1 - S_4) \Delta_{S_3 S_4}^{(2)} \mathbf{g}(S_4, R', w^2) + \\ & \sum_{S_1} \sum_{S_2 S_4} \mathbf{g}(R, S_1, w^2) \Delta_{S_1 S_2}^{(2)} \mathbf{g}(S_2, S_4, w^2) \delta(S_1 - S_4) (\mathbf{F}w^2) \mathbf{g}(S_4, R', w^2) + \\ & \sum_{S_1} \sum_{S_2 S_4} \mathbf{g}(R, S_1, w^2) \Delta_{S_1 S_2}^{(2)} \mathbf{g}(S_2, S_4, w^2) \delta(S_2 - S_4) (\mathbf{F}w^2) \mathbf{g}(S_4, R', w^2) + \\ & \sum_{S_1 S_2} \sum_{S_3 S_4} \mathbf{g}(R, S_1, w^2) \Delta_{S_1 S_2}^{(2)} \mathbf{g}(S_2, S_3, w^2) \delta(S_1 - S_3) \Delta_{S_3 S_4}^{(2)} \mathbf{g}(S_4, R', w^2) + \\ & \sum_{S_1 S_2} \sum_{S_3 S_4} \mathbf{g}(R, S_1, w^2) \Delta_{S_1 S_2}^{(2)} \mathbf{g}(S_2, S_3, w^2) \delta(S_1 - S_4) \Delta_{S_3 S_4}^{(2)} \mathbf{g}(S_4, R', w^2) + \\ & \sum_{S_1 S_2} \sum_{S_3 S_4} \mathbf{g}(R, S_1, w^2) \Delta_{S_1 S_2}^{(2)} \mathbf{g}(S_2, S_3, w^2) \delta(S_2 - S_3) \Delta_{S_3 S_4}^{(2)} \mathbf{g}(S_4, R', w^2) + \\ & \sum_{S_1 S_2} \sum_{S_3 S_4} \mathbf{g}(R, S_1, w^2) \Delta_{S_1 S_2}^{(2)} \mathbf{g}(S_2, S_3, w^2) \delta(S_2 - S_4) \Delta_{S_3 S_4}^{(2)} \mathbf{g}(S_4, R', w^2) + \\ & \sum_{S_1 S_2} \sum_{S_3 S_4} \mathbf{g}(R, S_1, w^2) \Delta_{S_1 S_2}^{(5)} \mathbf{g}(S_2, S_3, w^2) \delta(S_2 - S_4) \delta(S_1 - S_3) \Delta_{S_3 S_4}^{(5)} \mathbf{g}(S_4, R', w^2) + \\ & \sum_{S_1 S_2} \sum_{S_3 S_4} \mathbf{g}(R, S_1, w^2) \Delta_{S_1 S_2}^{(5)} \mathbf{g}(S_2, S_3, w^2) \delta(S_1 - S_4) \delta(S_2 - S_3) \Delta_{S_3 S_4}^{(5)} \mathbf{g}(S_4, R', w^2) \quad (5.8) \end{aligned}$$

Figure 5.4: The scattering diagrams for $n=2$.

Referring to Eqns. (5.7) and (5.8) we shall now build up the scattering diagrams. First we shall associate scattering vertices with the terms in $\tilde{\mathbf{M}}'$ and $\tilde{\mathbf{D}}'$. The Fig. (5.3) shows the seven different type of scattering vertices. The dashed lines are associated with the delta functions. With each factor \mathbf{g} we shall associate a propagator represented by a horizontal arrow. The connected diagrams to order n are then built up by stringing together $(n+1)$ propagators connected by n vertices with all dashed *fluctuation lines* connected in pairs. The algebraic terms in Eqn. (5.8) are then represented by the diagram shown in Fig. (5.4). The Edwards-Langer diagrams were originally developed only for diagonal disorder. The diagrams shown in Fig. (5.4) involve off-diagonal scattering terms and the associated diagrams are generalized scattering diagrams.

Fig. (5.5) shows all the topologically distinct classes of scattering diagrams for $n=3$. Note that it involves terms with contributions from $\mathbf{D}^{(1)}$, $\mathbf{D}^{(3)}$ and $\mathbf{D}^{(4)}$. These scattering vertices cannot sit either in the leftmost or in the rightmost positions, because one of the associated pseudo-fermion Green function line vanishes.

For $n=4$, there are various classes of diagrams as shown in Fig. (5.6). In this figure,

Figure 5.5: The topologically distinct scattering diagrams for $n=3$.

(i) the diagram of the type shown in the left most corner of the first row of (A) indicates a separable double tent diagram¹. The second tent goes to renormalize the rightmost phonon Green function from $\mathbf{g}(x, y)$ to $\ll \mathbf{G}(x, y) \gg$. (ii) the diagram of the type shown in the middle of the first row of (A) indicates a double tent non-separable diagram and (iii) the diagram of the type shown in the right most corner of the third row of (A) indicates a non-separable crossed-tent diagram. Of these, the inner tent in the double tent diagram (ii) goes on to renormalize the interior Green function. As such, the crossed tent diagram

¹a separable diagram is one that can be broken into two along a electron line without also breaking a pseudo-fermion line

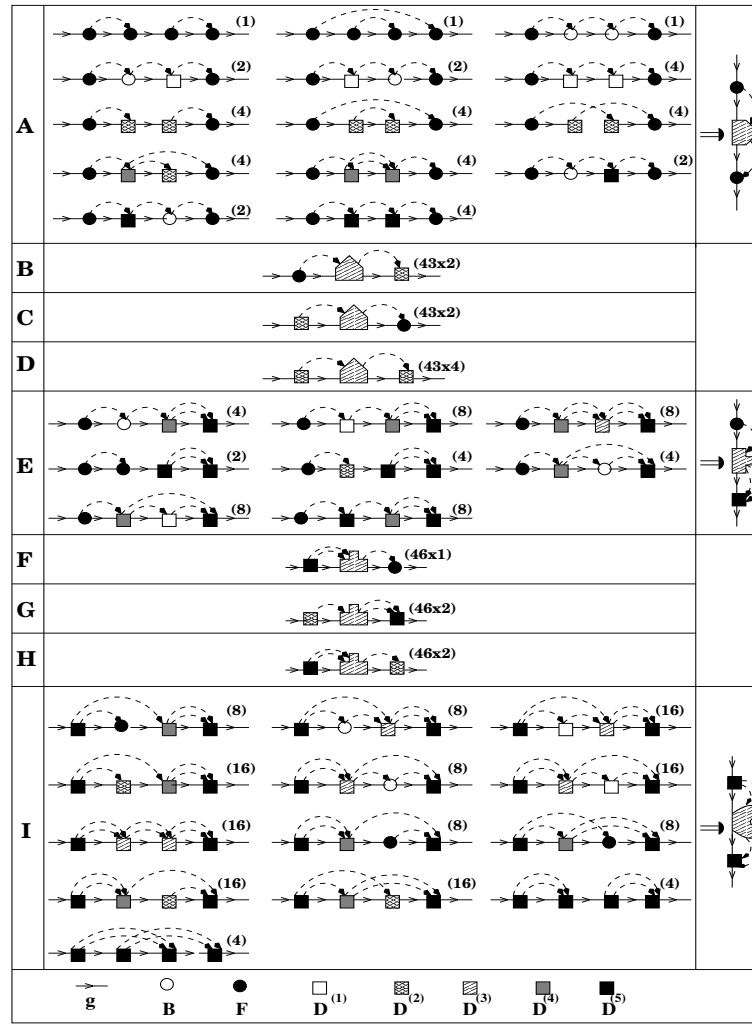


Figure 5.6: The topologically distinct classes of scattering diagrams for $n=4$.

(iii) is a *skeleton* diagram of this class. The kinds of diagrams other than these are few examples of skeleton diagrams in this order involving various types of vertices.

If we club together the contribution of *all* the skeleton diagrams calling this the self-energy, and allow *all* phonon Green functions except the left-most to be renormalized by the separable and non-separable, non-skeleton diagrams, we get the Dyson equation :

$$\ll G \gg = g + g \Sigma \ll G \gg$$

For homogeneous disorder we have shown earlier that we have translational symmetry in the full augmented space [Ghosh *et al* . 1999]. We can then take Fourier transform of the

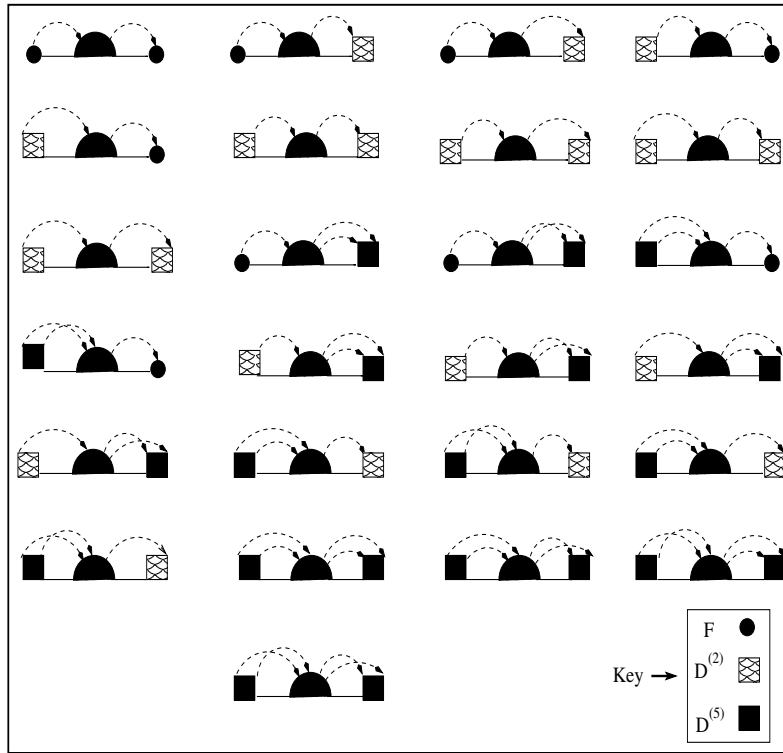


Figure 5.7: Structure of skeleton diagrams for the self-energy

above equation to get :

$$\ll \mathbf{G}(\mathbf{q}, \mathbf{E}) \gg = \mathbf{g}(\mathbf{q}, \mathbf{E}) + \mathbf{g}(\mathbf{q}, \mathbf{E}) \Sigma(\mathbf{q}, \mathbf{E}) \ll \mathbf{G}(\mathbf{q}, \mathbf{E}) \gg$$

The diagrams for the self-energy are skeleton diagrams *all* of which have the structure as shown in Fig. (5.7).

Let us now examine some specific Edwards-Langer scattering diagrams, in some detail, in order to understand their physical significance and relation to mean-field approximations. The first three diagrams on the first row of Fig. (5.8) arise because of purely diagonal disorder in mass. Of these the first two diagrams describe self-energy corrections to the VCA propagator because of configurations fluctuations at a single site. These diagrams are closely related to the diagrammatic treatment discussed by Leath [Leath 1968]. Referring to that earlier work, we note that these diagrams are explicitly included in the 1CPA. The self-energy arising out of such diagrams is site-diagonal, or k -independent in reciprocal space. The third diagram is the smallest order diagram of this type which de-

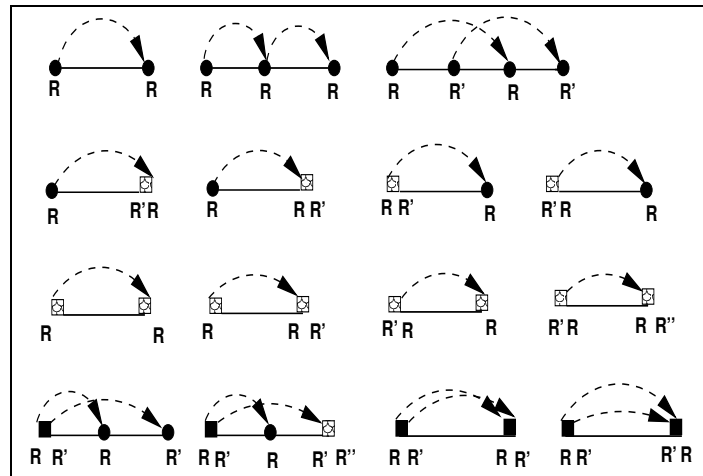


Figure 5.8: Details of some skeleton diagrams for the self-energy

scribes joint configuration fluctuations of two distinct sites. These type of diagrams take us beyond the 1CPA. For the 1CPA we ignore these *fourth order* diagrams, and all higher order diagrams, to all orders, describing joint configuration fluctuations of more than two sites. Within this approximation, the first inaccurate moment of the density of states is of order eight. If we include diagrams to all orders which describe joint configuration fluctuations of two sites we are lead to the 2CPA. This has been described in detail in the work of Aiyer *et al* . 1969 and Nickel and Krummhansl 1971.

The diagrams in the second row of Fig. (5.8) describe self-energy corrections due to configuration fluctuations at a single site for both diagonal (mass) and off-diagonal (force-constant) disorders. The first and the third diagrams lead to a diagonal self-energy, while the second and fourth diagrams lead to an off-diagonal contribution to the self-energy in real space. For off-diagonal disorder even these second order diagrams can lead to off-diagonal (real space) or k-dependent (reciprocal space) self-energy. Ignoring these contributions (to all orders) will lead to a 1CPA type approximation where even the fourth moment of the density of states will be inaccurate. This had been noted earlier for 1CPA in off-diagonal disorder problems. The diagrams in row three of Fig. (5.8) are very similar contributions from configuration fluctuations at a single site but arising out of pure off-diagonal disorder.

The diagrams on the last row of Fig. (5.8) describe self-energy contributions coming

from joint fluctuations of two sites arising out of off-diagonal disorder. All such diagrams take us beyond the 1CPA and some of them contribute to a self-energy which is off-diagonal (real space) or k -dependent (reciprocal space).

The formal summing up, to infinite order, of diagrams which involve configuration fluctuations involving single sites has been discussed by Leath 1968. This leads to the 1CPA and within this approximation the first inaccuracy occurs in the eighth moment of the averaged density of states. Nickel and Krummhanl 1971 have discussed in detail how to sum up, to infinite order, diagrams which also include joint configuration fluctuations of two sites. It is clear from this discussion that any generalization of a purely diagrammatic treatment of joint multi-site configuration fluctuations is a very difficult task indeed. However, a recursion based calculation of the self-energy, as proposed by us in our previous chapter (3), includes the contribution of such diagrams. Therefore, we propose the augmented space recursion as an alternative method for the calculation of averaged Green functions including effects of joint multi-site configuration fluctuations.

5.4 Coherent and Incoherent Inelastic scattering cross sections

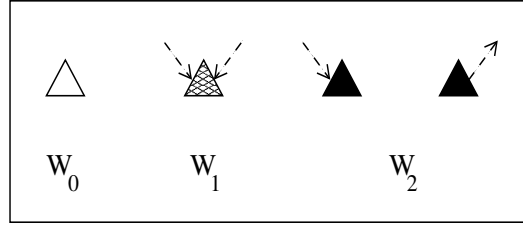
The calculation of inelastic scattering cross-sections has had a long history. For random alloys mention must be made of the work of Elliot and Taylor 1964 reviewed by Elliott *et al.* [Elliot *et al.* 1974]. Our arguments here are based on the ideas proposed by Nowak and Dederichs for the various kinds of scattering diagrams. It turns out that the numerical evaluation of these quantities require the entire configuration averaged Green matrices $\ll \mathbf{G}(\mathbf{q}, w) \gg$ and self energy matrices $\Sigma(\mathbf{q}, w)$ in the reciprocal space representation.

The formal expression for the inelastic cross-section for the scattering of thermal neutrons from an initial state labelled by \mathbf{k} to a final state \mathbf{k}' with a change of energy,

$$E = \hbar w = \frac{\hbar^2}{2M_n}(k^2 - k'^2)$$

and a change of wave-vector $\mathbf{q} = \mathbf{k} - \mathbf{k}' + \mathbf{Q}$, where \mathbf{Q} is a reciprocal lattice vector is :

$$\frac{d^2\sigma}{d\Omega dE} = \frac{1}{2N\hbar} \frac{k'}{k} \sum_R \sum_{R'} \sum_{\alpha\beta} q^\alpha q^\beta \left(W_R \Im m G_{RR'}^{\alpha\beta}(w) W_{R'} \right) n(w) \exp \{i\mathbf{q} \cdot (R - R')\} \quad (5.9)$$

Figure 5.9: The scattering vertices related to the fluctuations in W

here : $W_R = w_R \{ \exp[-(1/2)\langle (\mathbf{q} \cdot \mathbf{u}_R)^2 \rangle_{th}] \}$: w_R is the scattering length of the nucleus of the atom sitting at R , its equilibrium position, and $\mathbf{u}_R(t)$ is its deviation from equilibrium at the time t . $n(w)$ is the Bose distribution function. For a random alloy, w_R , the Debye-Waller factor, the atomic mass and the force constants are all random variables and dependent on one another via the random occupation variables $\{n_R\}$. Carrying out averaging over nuclear spins as well as over all the random configurations :

$$\left[\frac{d^2\sigma}{d\Omega dE} \right]_{av} = \frac{1}{2N\hbar} \frac{k'}{k} \sum_R \sum_{R'} \sum_{\alpha\beta} q^\alpha q^\beta \Im m \left[W_R G_{RR'}^{\alpha\beta}(w) W_{R'} \right]_{av} n(w) \exp \{ i\mathbf{q} \cdot (R - R') \} \quad (5.10)$$

Given homogeneity of disorder, we may rewrite the above configuration-average as :

$$\left[\frac{d^2\sigma}{d\Omega dE} \right]_{av} = \frac{1}{2\hbar} \frac{k'}{k} \sum_{\alpha\beta} q^\alpha q^\beta \Im m \mathcal{G}^{\alpha\beta}(\mathbf{q}, w) n(w) \quad (5.11)$$

$$\begin{aligned} \left[W_R G_{RR'}^{\alpha\beta}(w) W_{R'} \right]_{av} &= \mathcal{G}^{\alpha\beta}(R - R', w) \\ \mathcal{G}^{\alpha\beta}(\mathbf{q}, w) &= \sum_R \mathcal{G}^{\alpha\beta}(R, w) \exp \{ i\mathbf{q} \cdot R \} \end{aligned} \quad (5.12)$$

Since W_R is a random variable taking two values W_A and W_B depending on which kind of atom sits at the site labeled 'R', So we can write $W_R = W_A n_R + W_B (1 - n_R)$. Augmented space theorem then leads to the W factor being replaced by an operator in configuration-space as :

$$\begin{aligned} \widetilde{\mathbf{W}} &= \mathbf{A}(W) \mathbf{I} \otimes \mathbf{I} + \mathbf{B}(W) \sum_R \mathbf{P}_R \otimes \mathbf{p}_R^\downarrow + \mathbf{F}(W) \sum_R \mathbf{P}_R \otimes \mathbf{T}_R^{\uparrow\downarrow} \\ &= \mathbf{W}_0 \tilde{I} \otimes I + \mathbf{W}_1 \sum_R P_R \otimes p_R^\downarrow + \mathbf{W}_2 \sum_R P_R \otimes \mathcal{T}_R^{\uparrow\downarrow} \end{aligned} \quad (5.13)$$

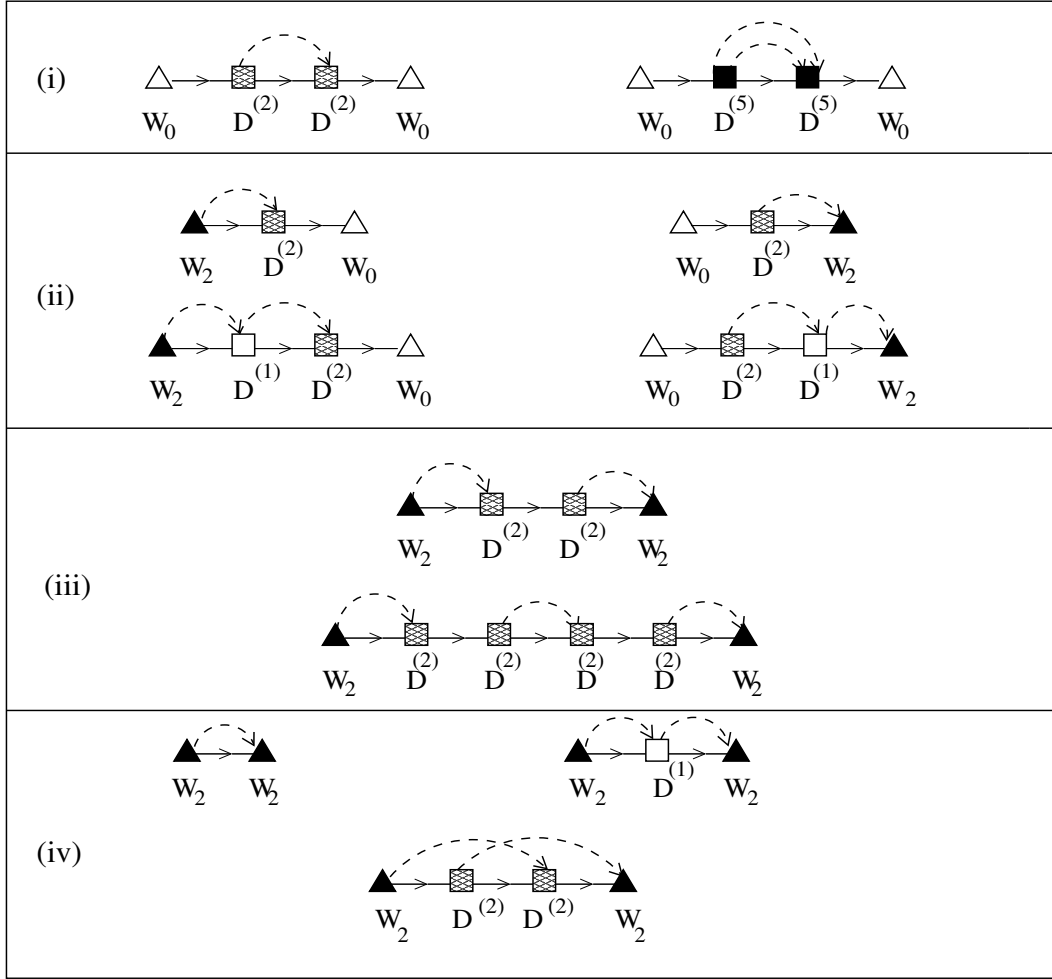


Figure 5.10: The scattering diagrams for the inelastic scattering cross-section

Since, like the mass, W is a scalar, mode independent quantity, $\mathbf{A}(W) = A(W) \delta_{\alpha\beta}$, $\mathbf{B}(W) = B(W) \delta_{\alpha\beta}$, $\mathbf{F}(W) = F(W) \delta_{\alpha\beta}$ and $\widetilde{\mathbf{W}} = \widetilde{W} \delta_{\alpha\beta}$. The scattering vertices arising out of Eqn. (5.13) are shown in Fig. (5.9). The augmented space theorem then gives :

$$\ll \mathbf{W}_R \mathbf{G}_{RR'} \mathbf{W}_{R'} \gg = \langle R \otimes \{\emptyset\} | \widetilde{\mathbf{W}} \left(\mathbf{g} + \mathbf{g} \widetilde{\mathbf{D}}_1 \mathbf{g} + \mathbf{g} \widetilde{\mathbf{D}}_1 \mathbf{g} \widetilde{\mathbf{D}}_1 \mathbf{g} + \dots \right) \widetilde{\mathbf{W}} | R' \otimes \{\emptyset\} \rangle \quad (5.14)$$

Fig. (5.10) shows few of the scattering diagrams produced from Eqn. (5.14) for the scattering cross-section. We have grouped them into four categories :

1. In the category (i) are reducible diagrams whose end vertices are \mathbf{W}_0 or the aver-

aged value $\ll W \gg \delta_{\alpha\beta}$. The central decorations are all the diagrams we have already seen for the configuration-averaged Green function. The contribution of these diagrams are therefore :

$$\mathbf{W}_0 \ll \mathbf{G}(\omega) \gg \mathbf{W}_0$$

2. The second set of diagrams (ii) are also reducible diagrams. Inspection of the diagrams immediately show us that their contribution may be written as :

$$\mathbf{W}'(\omega) \ll \mathbf{G}(\omega) \gg \mathbf{W}_0 + \mathbf{W}_0 \ll \mathbf{G}(\omega) \gg \mathbf{W}''(\omega)$$

The contribution of the 'vertex' $\mathbf{W}'(\omega)$ and $\mathbf{W}''(\omega)$ are closely related to the self-energy, with the initial and final vertices being different : \mathbf{W}_2 rather than \mathbf{D}_2 or \mathbf{D}_5 . We shall discuss this relationship subsequently.

3. The third set of diagrams (iii) are reducible diagrams with contribution :

$$\mathbf{W}'(\omega) \ll \mathbf{G}(\omega) \gg \mathbf{W}''(\omega)$$

The contribution of these three sets of reducible diagrams may be added together to give :

$$\mathbf{W}_{eff}(\omega) \ll \mathbf{G}(\omega) \gg \widehat{\mathbf{W}}_{eff}(\omega)$$

where

$$\mathbf{W}_{eff}(\omega) = \mathbf{W}_0 + \mathbf{W}'(\omega)$$

and

$$\widehat{\mathbf{W}}_{eff}(\omega) = \mathbf{W}_0 + \mathbf{W}''(\omega)$$

4. The last class of diagrams (iv) are irreducible diagrams. Their contribution is also related to the self-energy with both the initial and final vertices being \mathbf{W}_2 rather than $\mathbf{D}^{(2)}$ or $\mathbf{D}^{(5)}$. We shall discuss these diagrams in detail subsequently.

Because of the disorder renormalization, the \mathbf{W}_{eff} is diagonal neither in real nor mode space and becomes frequency dependent and complex. The reducible diagrams contributes to an expression :

$$\mathcal{G}_{red}^{\alpha\beta}(\mathbf{q}, \omega) = \sum_{\mu\nu} W_{eff}^{\alpha\mu}(\mathbf{q}, \omega) \ll G^{\mu\nu}(\mathbf{q}, \omega) \gg \widehat{W}_{eff}^{\nu\beta}(\mathbf{q}, \omega) \quad (5.15)$$

If we now examine the structure of the self-energy diagrams in Fig. (5.7), we note that the vertex $\mathbf{D}^{(2)}$ creates one configuration fluctuation at a site if it is an initial vertex and annihilates a configuration fluctuation if it is a final vertex. On the other hand, the $\mathbf{D}^{(2)}$ vertex creates *two* configuration fluctuations at two sites if it is an initial vertex and annihilates *two* configuration fluctuations at two sites if it is a final vertex. The diagrams for both $\mathbf{W}_{eff}(\omega)$ and the irreducible diagrams in Fig. (5.10) have vertices which create or annihilate only one configuration fluctuation at both the initial and final vertices. If we denote the part of the self-energy contributed by the diagrams in the first two lines of Fig. (5.7) by $\Sigma(w)$, then it follows that :

$$\begin{aligned}\mathbf{W}_{eff}(\mathbf{q}, \omega) &= \mathbf{W}_0 + \mathbf{W}_2 [\Delta(\mathbf{q})]^{-1} \Sigma(\mathbf{q}, \omega) \\ \widehat{\mathbf{W}}_{eff}(\mathbf{q}, \omega) &= \mathbf{W}_0 + \Sigma(\mathbf{q}, \omega) [\Delta(\mathbf{q})]^{-1} \mathbf{W}_2\end{aligned}\quad (5.16)$$

where

$$\Delta(\mathbf{q}) = \mathbf{F}(\mathbf{m}) \omega^2 + \mathbf{D}^{(2)}(\mathbf{q}) + \mathbf{D}^{(5)}(\mathbf{q})$$

The expression (5.15) is long-ranged in real-space. Following the argument of Nowak and Dederichs 1982 within the CPA and Mookerjee and Yussouff 1986 in a more general context of a cluster-CPA, we identify contribution of the reducible part as the coherent part of the inelastic scattering :

$$\left[\frac{d^2\sigma}{d\Omega dE} \right]_{av}^{coh} = \frac{1}{2\hbar} \frac{k'}{k} \sum_{\alpha\beta} q^\alpha q^\beta \Im m \left[\mathbf{W}_{eff}(\mathbf{q}, \omega) \ll \mathbf{G}(\mathbf{q}, \omega) \gg \widehat{\mathbf{W}}_{eff}(\mathbf{q}, \omega) \right]^{\alpha\beta} n(\omega)\quad (5.17)$$

If we now look back at the irreducible diagrams in class (iv) of Fig. (5.10), we note that the diagrams in the top row of (iv) are both short ranged : the leftmost one is totally diagonal in real-space and the rightmost one has the same range as the dynamical matrices, which are reasonably short ranged. The bottom diagram is longer ranged. However, this and *all* long ranged diagrams in this class involve crossed-tent diagrams. If we look at the diagrams for the self-energy exactly the same kind of structure is seen. The only diagrams which can lead to a long-ranged self-energy are the crossed-tent diagrams. One out of many such diagrams is the right most corner diagram of the third row of Fig. 4.4(A). These diagrams belong to correlated scattering from configuration fluctuations at

different sites. The contributions of such diagrams are dominated by those which are short-ranged. Within the single site coherent potential approximation (CPA) such diagrams are neglected altogether and the self-energy (and therefore the irreducible diagrams for the cross-section) is diagonal in real-space. Beyond the CPA, dominant contributions arise from correlated scattering of the smaller clusters and the contribution of the irreducible diagrams is also short-ranged : being between sites within the smaller clusters. The range of the self-energy and the irreducible diagrams are therefore as large as the size of the largest cluster whose correlated scattering is significant. The *Locality principle* of Heine [Heine 1980] convinces us that electronic structure is insensitive of far-off environment and, although the self-energy is not diagonal in real-space (except in the single-site CP approximation), its range is nevertheless short. This is behind the reasonable success of the CPA in any cases. Again, following the arguments of Nowak and Dederichs 1982 and Mookerjee and Yussouff 1986, this contribution can be related to the incoherent part of the inelastic scattering. The incoherent intensity is given by :

$$\left[\frac{d^2\sigma}{d\Omega dE} \right]_{av}^{incoh} = \frac{1}{2\hbar} \frac{k'}{k} \sum_{\alpha\beta} q^\alpha q^\beta \Im m \left[\mathbf{\Gamma}(\mathbf{q}, \omega) \right]^{\alpha\beta} n(\omega) \quad (5.18)$$

where

$$\mathbf{\Gamma}(\mathbf{q}, \omega) = \mathbf{W}_2 [\mathbf{\Delta}(\mathbf{q}, \omega)]^{-1} \mathbf{\Sigma}(\mathbf{q}, \omega) [\mathbf{\Delta}(\mathbf{q}, \omega)]^{-1} \mathbf{W}_2 \quad (5.19)$$

5.5 RESULTS AND DISCUSSION

In the next two sub-subsections, we explore the relative importance of mass and force constant disorder in the inelastic neutron scattering for two specific random alloys $Ni_{55}Pd_{45}$ and $Ni_{50}Pt_{50}$. In the previous two chapters, we have already studied the advantages of Augmented space recursion (ASR) over the simple CPA for understanding the dispersion and life time of phonons in random binary alloys. The present work is an extension of that work from the implementation point of view, since now we need to apply the Block recursion technique [discussed in section (Godin and Haydock 1988, Godin and Haydock 1992) of chapter 2] to calculate the full green matrix and self energy matrix.

5.5.1 $\text{Ni}_{55}\text{Pd}_{45}$ Alloy

We refer the reader to Table-3.1 of the chapter (3) for some of the basic properties of face-centered cubic Ni and Pd, which is relevant for our present calculation. The properties associated with the neutron scattering of Ni and Pd are reasonably favorable. The incoherent scattering cross section of Ni is fairly high, which was at first thought to be a potentially serious disadvantage, but in practice, this did not turn out to be much of a problem. It has been found that the scattered neutron distributions are always dominated by the coherent scattering even for high frequency mode with large widths. Experimental investigation shows that significant difference between the coherent scattering lengths of Ni and Pd (The coherent scattering length for Ni is 1.03 while that of Pd is 0.6 in units of 10^{-12}cm) produces additional incoherent scattering in $\text{Ni}_{55}\text{Pd}_{45}$, but this is much smaller than the incoherence produced by the Ni-atom itself in the alloy.

In Fig. (5.11), we display the inelastic coherent scattering cross sections [calculated from Eqn. (5.17)] obtained from our Block recursion calculation along the highest symmetry directions ($[\zeta 00]$, $[\zeta \zeta 0]$, $[\zeta \zeta \zeta]$, $\zeta = |\vec{q}|/|\vec{q}_{max}|$). For a particular direction, different curves indicate the cross sections at various ζ -points starting from the lowest value ($\zeta = 0$) to the edge of the Brillouin zone ($\zeta = 1$ in units of $2\pi/a$). The first thing to note is that the scattering cross sections are often asymmetric near the resonances. This property was also reflected in the phonon line shapes shown in the chapter (3). However the amount of asymmetries in the cross section is more than that in the usual Lorentzian shaped phonon line. That should be obvious because if we see the paper of Nowak and Dederichs 1982, there they have derived an expression for the coherent scattering cross section in the single site CPA framework, this expression contains in addition to the usual Lorentzian phonon line contribution [obtained from $\Im m \ll G(\mathbf{q}, w) \gg$], a second term which will have zero contribution only if the scattering length do not fluctuate (which is not the case in our formulation). They have also argued that this extra term leads to an asymmetry (rather small contribution) of the phonon line. One can also notice that the nature of asymmetry in the cross section is not the same as in the line shapes. This is due to the contribution of off-diagonal elements of the Green's matrix and self energy matrix in the coherent scattering cross section [as obvious from expression (5.17)]. This difference in the nature of asymmetry is more pronounced in the $[\zeta \zeta 0]$ and $[\zeta \zeta \zeta]$ symmetry directions, because the

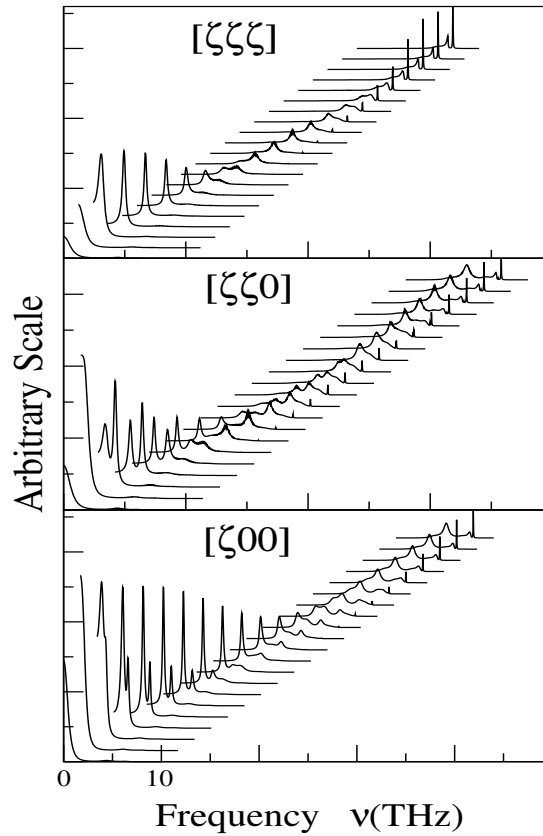


Figure 5.11: The coherent scattering cross section in different directions for $Ni_{55}Pd_{45}$. In each of the different directions, the various curves indicate the cross sections for various ζ values starting from the lowest value to the edge of the Brillouin zone. The y-axis is in an arbitrary scale with heights scaled to the maximum height. Different curves for different ζ values are shifted along the x-axis in order to facilitate vision.

Green's matrix [and self energy matrix] comes out to be completely diagonal in the $[\zeta 00]$ direction. The occurrence of such a structure of the cross section may also be due to the calculation in the mixed mode frame work. One should notice from the Block recursion technique described in section (Godin and Haydock 1988, Godin and Haydock 1992) of chapter 2 that, unlike the ordinary recursion where one extracts results for specific modes, the Block recursion requires a mixed mode starting state. For a real-space calculations on a lattice with Z-nearest neighbours, we start the recursion with :

$$\Phi_{J,\alpha\beta}^{(1)} = U_{\alpha\beta}^{(1)} \delta_{J,1} + U_{\alpha\beta}^{(2)} \delta_{J,Z+1}$$

while for a reciprocal space calculation we start with :

$$\Phi_{J,\alpha\beta}^{(1)} = U_{\alpha\beta}^{(1)} \delta_{J,1} + U_{\alpha\beta}^{(2)} \delta_{J,2}$$

where

$$U_{\alpha\beta}^{(1)} = \frac{A(m^{-1/2})}{[A(m^{-1})]^{1/2}} \delta_{\alpha\beta} \quad ; \quad U_{\alpha\beta}^{(2)} = \frac{F(m^{-1/2})}{[A(m^{-1})]^{1/2}} \delta_{\alpha\beta}$$

The asymmetries can be described as a tendency of more scattering to occur near the resonance frequencies. It is important to note that the coherent scattering cross sections have a pronounced \mathbf{q} -dependence in all the three symmetry directions. Because of the short range properties, the self energy (and $[\Delta(\mathbf{q})]^{-1}$) depends only rather weakly on \mathbf{q} and does not show any strong structure as a function of the same. The same applies for the effective scattering length \mathbf{W}_{eff} . Thus the only strong \mathbf{q} -dependence in the coherent cross section arises from the average Green's matrix $\ll \mathbf{G}(\mathbf{q}, \mathbf{w}) \gg$ which is a long range matrix due to it's dependence on reducible diagrams.

In Fig. (5.12) we display the incoherent scattering cross sections [calculated from Eqn.(5.18)] along the highest symmetry directions. In a particular direction, the different curves indicate the cross sections for various ζ -points starting from $\zeta = 0$ to $\zeta = 1$ (in units of $2\pi/a$). A look at fig. (5.12) immediately shows that the incoherent cross sections are very weakly dependent on \mathbf{q} . It is the " $q^\alpha q^\beta$ " factor in Eqn. (5.18) which weights up the cross sections as we go on increasing \mathbf{q} -points. These results are in accordance with the arguments of Nowak and Dederichs 1982 and Mookerjee and Yussouff 1986. They have also mentioned in their paper that, the weak \mathbf{q} -dependence of incoherent scattering cross section arises because of it's strong similarities with the self energy diagram which is itself a short range matrix due to it's dependence on irreducible diagrams and hence vary rather weakly with \mathbf{q} . Kamitakahara and Brockhouse also found a similar qualitative features for the coherent and incoherent cross sections in their Inelastic neutron scattering measurement.

5.5.2 $\text{Ni}_{50}\text{Pt}_{50}$ Alloy

This section will be devoted for the application of our formulation to NiPt alloys where both kinds of disorders are predominant. For a list of general properties of face-centered

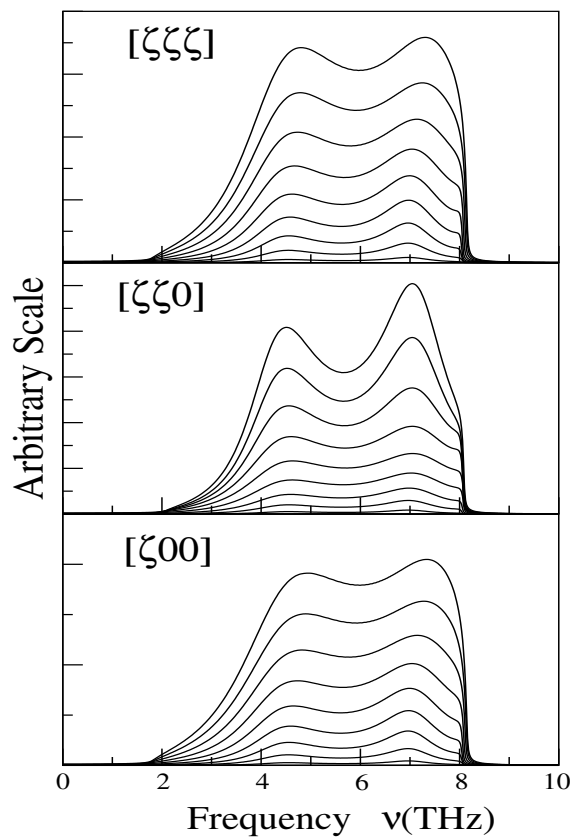


Figure 5.12: The incoherent scattering cross sections in different directions for $Ni_{55}Pd_{45}$ alloy with $\Phi_{Ni-Pd} = 0.7 \Phi_{Ni-Ni}$. In each of the different directions, the various curves indicate the cross sections for various ζ values starting from the lowest value to the edge of the Brillouin zone.

cubic Ni and Pt we refer the reader to the reference by Alam and Mookerjee 2004. Tsunoda *et al* 1979 investigated $Ni_{1-x}Pt_x$ by inelastic neutron scattering and compare their observations with the CPA. Here for illustrations, we have considered $x=0.5$ only because that makes it a concentrated alloy and the failure of CPA is qualitatively more prominent at this concentration.

In Fig. (5.13), we display the inelastic coherent scattering cross sections along the highest symmetry direction. As before, In a particular direction the different curves indicate the cross sections for various ζ -values. For the sake of simplicity, we have used the same parametrization of masses and force constants as used in the previous chapter (3). In $Ni_{50}Pt_{50}$ alloy, the coherent scattering cross sections show few extra features.

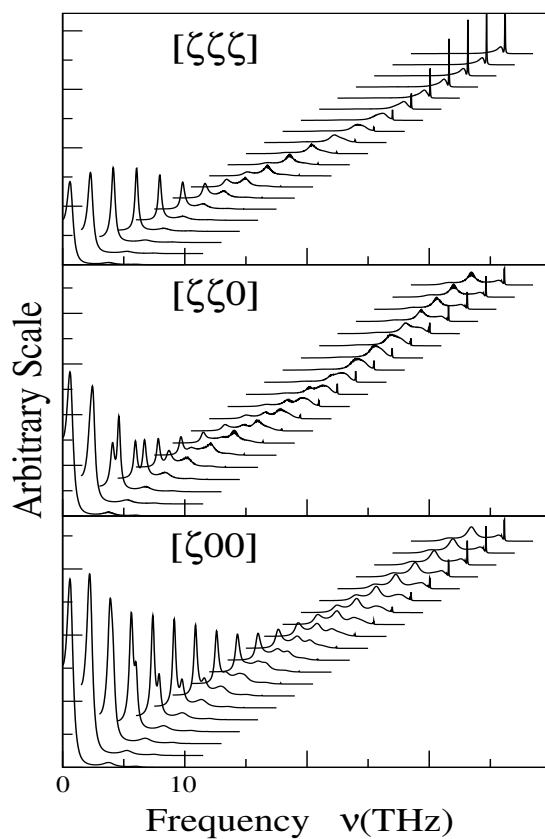


Figure 5.13: Same as Fig. (5.11) but for $Ni_{50}Pt_{50}$ alloy

Even in the $[\zeta 00]$ direction, the cross section becomes well separated double peaks along with weakly defined peak in between in the region from $\zeta = 0.68$ to the zone boundary. The occurrence of such a weakly defined peak is due to the inclusion of force constant disorder explicitly in our formulation. It is also clear from Fig. (5.13) that there exists no appreciable peak intensity below 3.7 THz for $\zeta \geq 0.68$ in all the three symmetry directions. Tsunoda also found the same structure below 3.5 THz for $\zeta \geq 0.7$. However CPA predicted the lower frequency peak to exist for all the ζ -values.

For smaller ζ -values, the lower frequency peaks are sharper than the high frequency ones, but the intensity of former decreases significantly with increasing wave vector however the latter gets sharper, in all the three symmetry directions. The phonon peaks are well defined for smaller ($\zeta \leq 0.38$) and higher ζ -values, but no well defined peaks were observed for intermediate values of ζ , presumably due to extreme line broadening. This

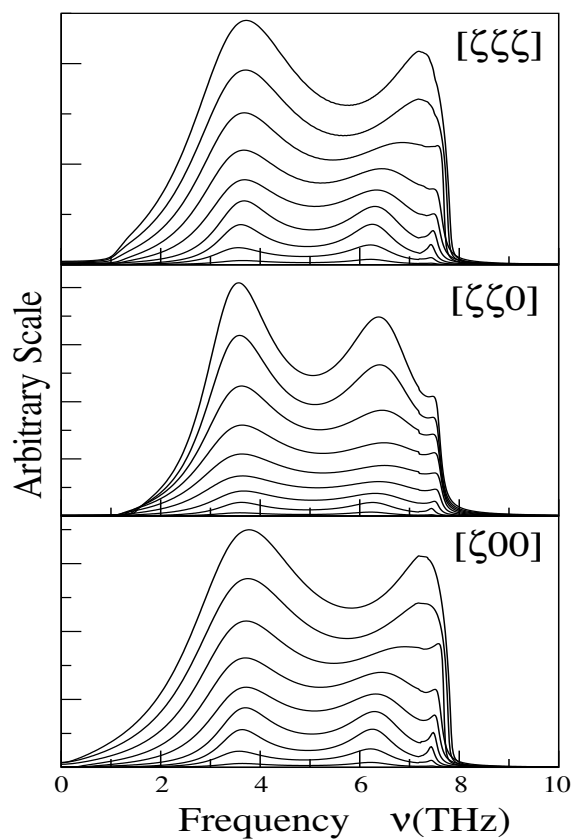


Figure 5.14: Same as Fig. (5.13) but for $Ni_{50}Pt_{50}$ alloy.

kind of qualitative features has also been observed experimentally by Tsunoda *et al* 1979 for longitudinal branches. This feature is more transparent in the $[\zeta\zeta 0]$ direction [Fig. (5.13)] where the low frequency peak gets broadened and becomes more asymmetric in the region between $\zeta = 0.4$ to $\zeta = 0.78$.

The incoherent scattering cross sections [given by Eqn. (5.18)] for $Ni_{50}Pt_{50}$ alloy along the highest symmetry directions are shown in Fig. (5.14). The weak \mathbf{q} -dependence of the cross section is obvious from the figure. The intensities for various \mathbf{q} 's in a particular direction have nearly an approximate q^2 dependence because of the factor ' $q^\alpha q^\beta$ ' in Eqn. (5.18).

In Fig.(5.15), we compare our results for the incoherent scattering cross section with those of the CPA and the experiment by Tsunoda *et al* 1979. Here the left, middle and right panel displays the augmented space block recursion (ASBR) result, experimental

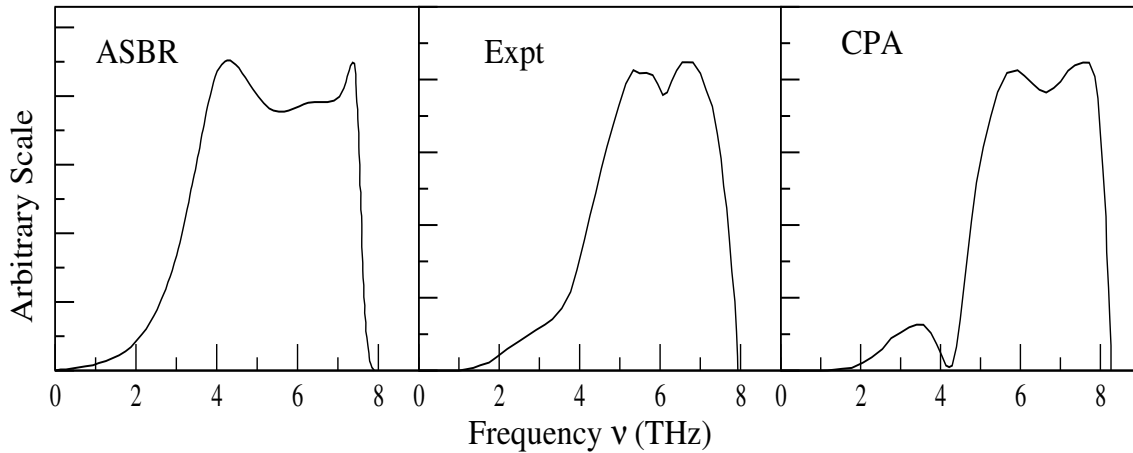


Figure 5.15: The incoherent scattering cross section for $Ni_{50}Pt_{50}$. The left panel, middle panel and right panel display the block recursion result, experimental curve and the CPA result respectively.

curve and the CPA result respectively. In the CPA result we can observe a dip at the frequency corresponding to the phonon band gap observed in the dispersion curves. This suggests a split band behaviour which clearly separates the Pt-contribution in the low frequency region from the Ni-contribution in the high frequency region, because the low frequency region is dominated by the Pt-atom (heavier atom) having much lower incoherent scattering length than Ni [the incoherent scattering length for Pt is 0.1 while that of Ni is 4.5]. This kind of spurious gap however is not observed in the recursion result, because the CPA results are based on the mass fluctuations alone, ignoring the off-diagonal and environmental disorder arising out of the dynamical matrix. On the other hand, by incorporating the force constant disorder as is done in the block recursion, we get rid of this spurious gap and obtain rather a good agreement with the experimental results. The overall qualitative behaviour is similar. In addition the phonon band edges in the recursion results are very close to the experimental ones. The recursion finds the right band-edge at $\simeq 7.90 THz$, Tsunoda finds this band-edge experimentally at $\simeq 7.93 THz$ while the CPA gives a rather higher value of $\simeq 8.267 THz$.

5.6 Concluding Remarks

We have derived a theoretical formulation for the separation of total intensity of thermal neutron scattering from disordered alloys into a coherent and an incoherent part. The use of the augmented space to keep track of the configuration of the system has made the formalism simple yet powerful. In essence, the splitting is identical to that introduced by Nowak and Dederichs 1982 within a scattering diagrammatic technique except that it has been done *exactly* without taking any recourse to mean-field like approximation. Unlike the method proposed by Mookerjee and Yussouff 1986, where the diagram technique was exceedingly difficult to generalize into even a small cluster CPA, the augmented space block recursion proved to be simpler to apply the formalism on realistic random alloys. We have applied the method to NiPd and NiPt alloys. In $Ni_{55}Pd_{45}$, we have demonstrated that mass disorder plays the prominent role. In addition our coherent scattering cross section enable us to understand the effect of small contribution of the off-diagonal elements of Green matrix. The results on $Ni_{50}Pt_{50}$ alloy however demonstrate the prominence of force constant disorder even in a case where the mass ratio is $\simeq 3$. Our results agree well both with the coherent and the incoherent scattering experiments, where as the CPA fails both qualitatively and quantitatively. We propose the technique as a computationally fast and efficient method for the study of inelastic neutron scattering in disordered systems.

Chapter 6

Thermal transport in disordered binary alloys

6.1 Introduction

Lattice thermal conductivity of substitutionally disordered alloys yields valuable information about the interactions of thermal excitations with composition fluctuations on their crystal lattice. In the past few decades, there has been considerable attention toward the experimental studies [Farrell and Greig 1969, Garber *et al* 1963, Bauers *et al* 1991, Srivastava *et al* 1970] of the thermal conductivity of disordered alloys. As far as the theoretical understanding is concerned, it is not so extensive because the presence of disorder results in scattering that not only depends on the impurity concentration but also crucially on both relative masses and size difference between the constituent atoms. For large mass or size differences, the effect of disorder can be quite unusual. Because of this, detailed comparison between theory and experiment on the basis of realistic model has not been very extensive. Most of the theoretical calculations are mostly based on mass disorder, whereas in phonon problems essential off-diagonal disorder in the force constants can not be dealt with single site mean field approximations. Such disorder can not be ignored in a realistic calculation.

⁰The contents of this chapter has been published in three papers :

1. Aftab Alam and A Mookerjee, *Phys. Rev.* **B 72**, 214207 (2005)
2. Aftab Alam and A Mookerjee, *J. Phys.: Condens. Matter* **18**, 4589-4608 (2006)
3. Aftab Alam and A Mookerjee [Accepted for publication in *Int. J. Mod. Phys. B*], (cond-mat/0604373)

Flicker and Leath 1973 first proposed the calculation of lattice thermal conductivity within a single-site coherent potential approximation (CPA) using the appropriate Kubo formula. The single-site CPA is a mean field approximation, capable of dealing with mass disorder alone and is not adequate for treating intrinsic off-diagonal disorder arising out of the force constants. This was evidenced in the inability of the single site CPA to explain experimental life time data on NiPt [Tsunoda *et al* 1979]. Translationally invariant, multiple site, multiple scattering theories based on the augmented space formalism [Mookerjee 1973] have recently been proposed by Ghosh *et al* 2002 as well as by us [Alam and Mookerjee 2004] to describe phonons in a series of random alloy systems : NiPt, NiPd and NiCr. These formalisms explicitly capture the effects of both the diagonal and off-diagonal disorder.

When we come to comparison between theory and experiment, there is a different kind of difficulty. In any experiment, the measured thermal conductivity κ consists of the sum of an electronic component κ_e and a lattice component κ_L and $\kappa = \kappa_e + \kappa_L$. Assuming the thermal analogue of Matthiessen's rule to be valid, the electronic thermal resistivity $W_e = 1/\kappa_e$ is given by the sum of an ideal resistivity and an impurity or residual term. It is often assumed that the ideal resistivity remains unaltered by alloying and can be obtained from the measurements on pure metals. The residual resistivity W_r can be calculated with the help of Widemann-Franz law $W_r = \rho_0(T)/(L_0T)$, where L_0 is the Lorenz number and $\rho_0(T)$ is determined by measuring the electrical resistivity of the alloy at several temperatures. The lattice component κ_L can then be separated out from the observed conductivity κ . Overall what we would like to convey from these details is that a direct measurement of the lattice component of the thermal conductivity is not feasible. There always exists certain assumptions behind the calculation of κ_e and hence it is not possible always to obtain reliable estimates for this quantity which consequently affects the separation of κ_L from the observed conductivity κ .

In this chapter, we shall first introduce a Kubo-Greenwood type formula which relates the thermal conductivity to the (heat) current-current correlation function. The ideas used here are very similar to those proposed by Allen and Feldman 1993 except that the present formulation is done keeping in mind the application to a substitutionally disordered crystal, rather than an amorphous system. For disordered alloys, configuration

averaging over various random atomic arrangements have been carried out using the augmented space formalism (ASF) introduced by the authors [Mookerjee 1973]. The ASF goes beyond the usual mean-field approaches and takes into account configuration fluctuations over a large local environment. We shall combine the augmented space representation for phonons [Alam and Mookerjee 2004] with a scattering diagrammatic technique to get an effective heat current. This effective current consists in addition to the averaged current term, also the terms arising out of the disorder scattering corrections. We will show that these disorder induced corrections to the averaged current terms are directly related either to the disorder scattering induced self-energy matrix in the propagator or to vertex corrections. As far as the vertex corrections are concerned, Leath 1970 had obtained these corrections within the framework of CPA by using diagram summations. In this chapter we shall derive the contribution of these corrections in a more generalized context with the inclusion of diagonal as well as the intrinsic off-diagonal disorder arising out of the dynamical matrix. Since in earlier chapters (1 and 5), we have already shown that the self energy matrix and the Green matrix can be calculated for realistic binary alloys within an augmented space block recursion (ASBR) technique, so the present formulation will form the basis of a subsequent calculation of lattice thermal conductivity in realistic alloys.

6.2 Lattice Thermal Conductivity : A Kubo Greenwood formulation

The Kubo formula which relates the optical conductivity to a current-current correlation function is well established. The Hamiltonian contains a term $\sum_i \mathbf{j}_i \cdot \mathbf{A}(\mathbf{r}, t)$ which drives the electrical current. For thermal conductivity we do not have a similar term in the Hamiltonian which drives a heat current. The derivation of a Kubo formula in this situation requires an additional statistical hypothesis [Allen and Feldman 1993], which states that a system in steady state has a space dependent *local* temperature $T(\mathbf{r}) = [\kappa_B \beta(\mathbf{r})]^{-1}$. The expression for the heat current has been discussed in great detail by Hardy 1963 and Allen and Feldman 1993. The readers are referred to these papers for the details of calculation. The matrix element of the heat current in the basis of the

eigenfunctions of the Hamiltonian is given by :

$$\mathbf{S}_{\gamma\gamma'}^\mu(\mathbf{k}) = \frac{\hbar}{2} (\omega_{\mathbf{k}\gamma} + \omega_{\mathbf{k}\gamma'}) \mathbf{v}_{\gamma\gamma'}^\mu(\mathbf{k}) \quad (6.1)$$

where, the phonon group velocity $\mathbf{v}_{\gamma\gamma'}(\mathbf{k})$ is given by

$$\begin{aligned} \mathbf{v}_{\gamma\gamma'} &= \frac{i}{2\sqrt{\omega_{\mathbf{k}\gamma}\omega_{\mathbf{k}\gamma'}}} \sum_{\mu} \sum_{\nu} \epsilon_{\gamma}^{\mu}(\mathbf{k}) \epsilon_{\gamma'}^{\nu}(\mathbf{k}) \left(\sum_{\mathbf{R}_{ij}} \frac{\Phi^{\mu\nu}(\mathbf{R}_{ij})}{\sqrt{M_i M_j}} \right) \mathbf{R}_{ij} e^{i\mathbf{k}\cdot\mathbf{R}_{ij}} \\ &= \frac{1}{2\sqrt{\omega_{\mathbf{k}\gamma}\omega_{\mathbf{k}\gamma'}}} \sum_{\mu} \sum_{\nu} \epsilon_{\gamma}^{\mu}(\mathbf{k}) \nabla_{\mathbf{k}} D^{\mu\nu}(\mathbf{k}) \epsilon_{\gamma'}^{\nu}(\mathbf{k}) \end{aligned} \quad (6.2)$$

here γ, γ' label the various modes of vibration, $\omega_{\mathbf{k}\gamma}, \omega_{\mathbf{k}\gamma'}$ are their frequencies, $\epsilon_{\gamma}^{\mu}(\mathbf{k}), \epsilon_{\gamma'}^{\nu}(\mathbf{k})$ are the polarization vectors and $D^{\mu\nu}(\mathbf{k})$ is the Fourier transform of mass scaled dynamical matrix. We shall consider the case where the temperature gradient is uniform within the system. The Kubo formula then relates the linear heat current response to the temperature gradient field

$$\langle S^{\mu}(t) \rangle = - \sum_{\nu} \int_{-\infty}^{\infty} dt' \kappa^{\mu\nu}(t-t') \nabla^{\nu} \delta T(t)$$

where

$$\kappa^{\mu\nu}(\tau) = \Theta(\tau) \frac{1}{T} \int_0^{\beta} d\lambda \langle S^{\mu}(-i\hbar\lambda), S^{\nu}(\tau) \rangle.$$

$\Theta(\tau)$ is the Heaviside step function, and

$$S(-i\hbar\lambda) = e^{\lambda H} S e^{-\lambda H}.$$

$\langle \rangle$ on the right-hand side of the above equation denotes thermal averaging over states in the absence of the temperature gradient. The above equation can be rewritten in the form of a Kubo-Greenwood expression

$$\begin{aligned} \kappa^{\mu\nu}(\omega, T) &= \kappa_I^{\mu\nu}(\omega, T) + \kappa_{II}^{\mu\nu}(\omega, T) \\ \kappa_I^{\mu\nu}(\omega, T) &= \frac{\pi}{T} \int \frac{d^3\mathbf{k}}{8\pi^3} \sum_{\gamma} \sum_{\gamma' \neq \gamma} \frac{\langle n_{\mathbf{k}\gamma'} \rangle - \langle n_{\mathbf{k}\gamma} \rangle}{\hbar(\omega_{\mathbf{k}\gamma} - \omega_{\mathbf{k}\gamma'})} \mathbf{S}_{\gamma\gamma'}^{\mu}(\mathbf{k}) \mathbf{S}_{\gamma'\gamma}^{\nu}(\mathbf{k}) \delta(\omega_{\mathbf{k}\gamma} - \omega_{\mathbf{k}\gamma'} - \omega) \end{aligned} \quad (6.3)$$

$$\begin{aligned} \kappa_{II}^{\mu\nu}(\omega, T) &= \frac{1}{\kappa_B T^2} \left[\left\{ \int \frac{d^3\mathbf{k}}{8\pi^3} \sum_{\gamma} \langle n_{\mathbf{k}\gamma} \rangle \mathbf{S}_{\gamma\gamma}^{\mu}(\mathbf{k}) \right\} \left\{ \int \frac{d^3\mathbf{k}}{8\pi^3} \sum_{\gamma} \langle n_{\mathbf{k}\gamma} \rangle \mathbf{S}_{\gamma\gamma}^{\nu}(\mathbf{k}) \right\} \right. \\ &\quad \left. - \kappa_B T \int \frac{d^3\mathbf{k}}{8\pi^3} \sum_{\gamma} \frac{\partial \langle n_{\mathbf{k}\gamma} \rangle}{\partial(\hbar\omega_{\mathbf{k}\gamma})} \mathbf{S}_{\gamma\gamma}^{\mu}(\mathbf{k}) \mathbf{S}_{\gamma\gamma}^{\nu}(\mathbf{k}) \right] \delta(\omega) \end{aligned} \quad (6.4)$$

where $\langle n_{\mathbf{k}\gamma} \rangle = (e^{\beta\hbar\omega_{\mathbf{k}\gamma}} - 1)^{-1}$ is the equilibrium Bose Einstein distribution function and T is the absolute temperature.

The first expression is for inter-band transitions, while the second expression is for intra-band transitions. For an isotropic response, we can rewrite the first expression as

$$\kappa_I(\omega, T) = \frac{\pi}{3T} \sum_{\mu} \int d\omega' \int \frac{d^3\mathbf{k}}{8\pi^3} \sum_{\gamma} \sum_{\gamma'} \widehat{\mathbf{S}}_{\gamma\gamma'}^{\mu}(\mathbf{k}, T) \widehat{\mathbf{S}}_{\gamma'\gamma}^{\mu}(\mathbf{k}, T) \delta(\omega' - \omega_{\mathbf{k}\gamma'}) \delta(\omega' + \omega - \omega_{\mathbf{k}\gamma})$$

where

$$\widehat{\mathbf{S}}_{\gamma\gamma'}^{\mu}(\mathbf{k}, T) = \sqrt{\left| \frac{\langle n_{\mathbf{k}\gamma'} \rangle - \langle n_{\mathbf{k}\gamma} \rangle}{\hbar(\omega_{\mathbf{k}\gamma} - \omega_{\mathbf{k}\gamma'})} \right|} \mathbf{S}_{\gamma\gamma'}^{\mu}(\mathbf{k}).$$

We may rewrite the above equation as

$$\kappa_I(\omega, T) = \frac{1}{3\pi T} \sum_{\mu} \int d\omega' \int \frac{d^3\mathbf{k}}{8\pi^3} \text{Tr} \left[\widehat{\mathbf{S}}^{\mu}(\mathbf{k}, T) \Im m\{\mathbf{G}(\mathbf{k}, \omega')\} \widehat{\mathbf{S}}^{\mu}(\mathbf{k}, T) \Im m\{\mathbf{G}(\mathbf{k}, \omega' + \omega)\} \right].$$

The operator $\mathbf{G}(\omega)$ is the phonon Green operator $(M\omega^2\mathbf{I} - \Phi)^{-1}$. The Trace is invariant in different representations. For crystalline systems, usually the Bloch basis $\{|\mathbf{k}, \gamma\rangle\}$ is used. For disordered systems, prior to configuration averaging, it is more convenient to use the basis $\{|\mathbf{k}, \alpha\rangle\}$, where \mathbf{k} is the reciprocal vector and α represents the coordinate axes directions. We can transform from the mode basis to the coordinate basis by using the transformation matrices $\Upsilon_{\gamma\alpha}(\mathbf{k}) = \epsilon_{\gamma}^{\alpha}(\mathbf{k})$. For example

$$\widehat{\mathbf{S}}_{\alpha\beta}^{\mu}(\mathbf{k}, T) = \Upsilon_{\alpha\gamma}^{-T}(\mathbf{k}) \widehat{\mathbf{S}}_{\gamma\gamma'}^{\mu}(\mathbf{k}, T) \Upsilon_{\gamma'\beta}^{-1}(\mathbf{k}).$$

If we define

$$\kappa(z_1, z_2) = \int \frac{d^3\mathbf{k}}{8\pi^3} \text{Tr} \left[\widehat{\mathbf{S}} \mathbf{G}(\mathbf{k}, z_1) \widehat{\mathbf{S}} \mathbf{G}(\mathbf{k}, z_2) \right]. \quad (6.5)$$

then the above equation becomes,

$$\begin{aligned} \kappa_I(\omega, T) = & \frac{1}{12\pi T} \sum_{\mu} \int d\omega' \left[\kappa^{\mu\mu}(\omega'^-, \omega'^+ + \omega) + \kappa^{\mu\mu}(\omega'^+, \omega'^- + \omega) \right. \\ & \left. - \kappa^{\mu\mu}(\omega'^+, \omega'^+ + \omega) - \kappa^{\mu\mu}(\omega'^-, \omega'^- + \omega) \right] \end{aligned} \quad (6.6)$$

where

$$f(\omega^+) = \lim_{\delta \rightarrow 0} f(\omega + i\delta), \quad f(\omega^-) = \lim_{\delta \rightarrow 0} f(\omega - i\delta).$$

We have used the Herglotz analytic property of the Green operator

$$\mathbf{G}(\omega + i\delta) = \Re[\mathbf{G}(\omega)] - i \operatorname{sgn}(\delta) \Im[\mathbf{G}(\omega)].$$

For disordered materials, we shall be interested in obtaining the configuration averaged response functions. This will require the configuration averaging of quantities like $\kappa(z_1, z_2)$.

6.3 Effects of disorder scattering correction : A scattering diagram approach

Refer to the previous chapter (5), we had derived an expression for the configuration averaged green matrix [Eqn. 5.5] as

$$\ll \mathbf{G}(R, R', \omega^2) \gg = \langle \{\emptyset\} \otimes R | (\mathbf{g}^{-1} - \widetilde{\mathbf{D}}_1)^{-1} | \{\emptyset\} \otimes R' \rangle \quad (6.7)$$

where

$$\mathbf{g} = (\ll \widetilde{\mathbf{M}} \gg \omega^2 - \ll \widetilde{\mathbf{D}} \gg)^{-1} \quad (6.8)$$

with

$$\Upsilon_R = \mathbf{B}(\mathbf{m}) \omega^2 \mathbf{p}_R^\downarrow + \mathbf{F}(\mathbf{m}) \omega^2 \mathbf{T}_R^{\uparrow\downarrow} \quad (6.9)$$

$$\begin{aligned} \Psi_{RR'} = & \mathbf{D}_{RR'}^{(1)} (\mathbf{p}_R^\downarrow + \mathbf{p}_{R'}^\downarrow) + \mathbf{D}_{RR'}^{(2)} (\mathbf{T}_R^{\uparrow\downarrow} + \mathbf{T}_{R'}^{\uparrow\downarrow}) + \mathbf{D}_{RR'}^{(3)} \mathbf{p}_R^\downarrow \mathbf{p}_{R'}^\downarrow + \\ & \mathbf{D}_{RR'}^{(4)} (\mathbf{p}_R^\downarrow \mathbf{T}_{R'}^{\uparrow\downarrow} + \mathbf{T}_R^{\uparrow\downarrow} \mathbf{p}_{R'}^\downarrow) + \mathbf{D}_{RR'}^{(5)} \mathbf{T}_R^{\uparrow\downarrow} \mathbf{T}_{R'}^{\uparrow\downarrow} \end{aligned} \quad (6.10)$$

where

$$\begin{aligned} \mathbf{D}^{(1)} &= (y - x) \Phi_{(1)} \\ \mathbf{D}^{(2)} &= \sqrt{xy} \Phi_{(1)} \\ \mathbf{D}^{(3)} &= (y - x)^2 \Phi_{(2)} \\ \mathbf{D}^{(4)} &= \sqrt{xy} (y - x) \Phi_{(2)} \\ \mathbf{D}^{(5)} &= xy \Phi_{(2)}. \end{aligned}$$

Scattering diagrams are obtained by expanding the Eq. (6.7) as an infinite series and the terms \mathbf{B} , \mathbf{F} and $\mathbf{D}^{(1)}$ to $\mathbf{D}^{(5)}$ are represented as scattering vertices (see Fig. 6.1).

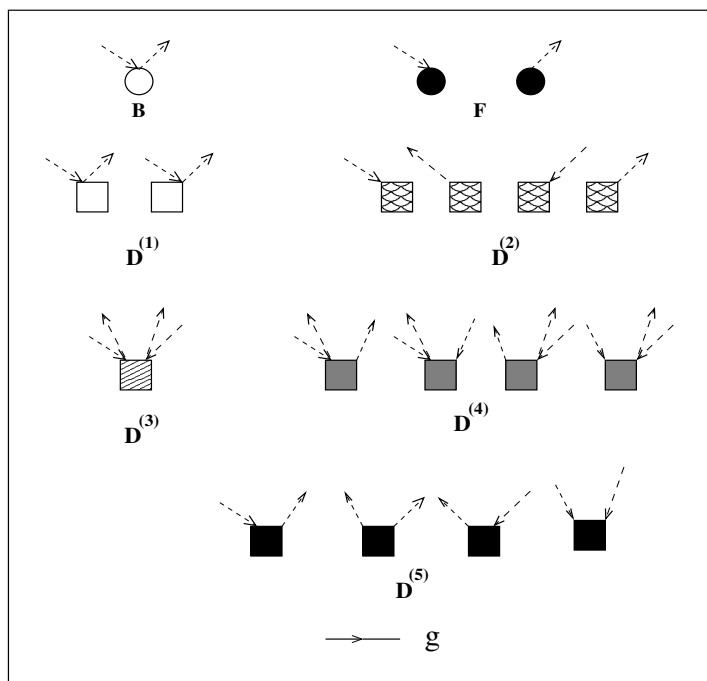


Figure 6.1: The scattering vertices for the averaged Green function

It might be instructive to understand what these scattering vertices represent physically. If we look at Eq. (6.7), we note that the term $\widetilde{\mathbf{D}}_1$ leads to the creation or annihilation of *configuration fluctuations* over and above the virtual crystal description. The vertices \mathbf{F} shown in Fig. (6.1), create and annihilate a configuration fluctuation at a given site because of mass disorder, while the vertex \mathbf{B} counts the number of such fluctuations at a given site. These are the only type of configuration fluctuations we can have if we had single site mass disorder alone. The single-site mean-field approximations like the single-site coherent potential approximation (1CPA) can ideally deal with situations where we ignore the other vertices in Fig. (6.1).

The vertices $\mathbf{D}^{(2)}$ also describe creation and annihilation of configuration fluctuations at single sites. That is, fluctuations at any one end of the two-site dynamical matrix. Similarly, the vertices $\mathbf{D}^{(1)}$ count the number of configuration fluctuations at any one of the two ends of the dynamical matrix. These are also single-site configuration fluctuations but arise due to fluctuations in the two-site dynamical matrix. These may also be treated with some variant of the 1CPA. For example, there are versions of the 1CPA which assume

$2\mathbf{D}^{AB} = \mathbf{D}^{AA} + \mathbf{D}^{BB}$. With such an assumption only the single site configurations fluctuation vertices are non-zero.

The vertices $\mathbf{D}^{(5)}$ describe creation and annihilation of *two* configuration fluctuations, one at either end of the two-site dynamical matrix. The vertex $\mathbf{D}^{(3)}$ counts the number of configuration fluctuations at either end of the dynamical matrix. The vertices $\mathbf{D}^{(4)}$ are mixed types which both create or annihilate a configuration fluctuation at one end of the dynamical matrix *and* count the number of fluctuations at the other end. These last three vertices describe configurations fluctuations which are essentially two-site and cannot be properly described within a single-site mean-field approximation.

The end point of the formulation described in the previous chapter (5) was the derivation of a Dyson equation :

$$\ll \mathbf{G} \gg = \mathbf{g} + \mathbf{g} \Sigma \ll \mathbf{G} \gg .$$

For homogeneous disorder we have shown earlier that we have translational symmetry in the full augmented space [Ghosh *et al* . 1999]. We can then take Fourier transform of the above equation to get

$$\ll \mathbf{G}(\mathbf{k}, E) \gg = \mathbf{g}(\mathbf{k}, E) + \mathbf{g}(\mathbf{k}, E) \Sigma(\mathbf{k}, E) \ll \mathbf{G}(\mathbf{k}, E) \gg .$$

The diagrams for the self-energy are skeleton diagrams¹ which have the structure as shown in Fig. (5.7) of the previous chapter (5). Each of the 25 different diagram starts with any one of \mathbf{F} , $\mathbf{D}^{(2)}$ or $\mathbf{D}^{(5)}$ and the central dark semicircle represents *all* possible arrangements of scattering vertices to *all* orders.

6.3.1 Configuration averaging of lattice thermal conductivity

Let us now go back to Eqn. (6.5) and discuss the configuration averaging of the two-particle green function of the kind $\kappa(z_1, z_2)$. The augmented space theorem immediately implies that

$$\ll \kappa(z_1, z_2) \gg = \int \frac{d^3\mathbf{k}}{8\pi^3} \text{Tr} \left\{ \langle \{\emptyset\} | [\tilde{\mathbf{S}}\tilde{\mathbf{G}}(\mathbf{k}, z_1) \tilde{\mathbf{S}}\tilde{\mathbf{G}}(\mathbf{k}, z_2)] | \{\emptyset\} \rangle \right\} \quad (6.11)$$

¹A skeleton diagram is a non-separable diagram all of whose propagators are fully disorder renormalized propagators.

The first thing to note about Equation. (6.11) is that the right hand side is an average of the product of four random functions whose fluctuations are correlated. The average of the product then involves the product of the averages and other contributions which come from averages taken in pairs, triplets and all four random functions.

In real space the random expression $\widehat{\mathbf{S}}$ for a binary alloy can take the values $\widehat{\mathbf{S}}^{AA}$, $\widehat{\mathbf{S}}^{AB}$, $\widehat{\mathbf{S}}^{BA}$ or $\widehat{\mathbf{S}}^{BB}$ with probabilities x^2 , xy , yx and y^2 respectively. We may rewrite the current $\widehat{\mathbf{S}}_{R\alpha,R'\beta}$ as

$$\begin{aligned}\widehat{\mathbf{S}}_{R\alpha,R'\beta} &= \widehat{\mathbf{S}}_{R\alpha,R'\beta}^{AA} n_R n_{R'} + \widehat{\mathbf{S}}_{R\alpha,R'\beta}^{AB} n_R (1 - n_{R'}) + \widehat{\mathbf{S}}_{R\alpha,R'\beta}^{BA} (1 - n_R) n_{R'} \\ &\quad + \widehat{\mathbf{S}}_{R\alpha,R'\beta}^{BB} (1 - n_R)(1 - n_{R'}).\end{aligned}$$

Following the same procedure as for the single particle Green functions we get

$$\begin{aligned}\widetilde{\mathbf{S}} &= \sum_{R\alpha} \sum_{R'\alpha'} \left[\ll \widehat{\mathbf{S}} \gg_{R\alpha,R'\alpha'} \mathbf{I} \otimes \mathbf{T}_{RR'} + \mathbf{S}_{R\alpha,R'\alpha'}^{(1)} (\mathbf{p}_R^\downarrow + \mathbf{p}_{R'}^\downarrow) \otimes \mathbf{T}_{RR'} \right. \\ &\quad + \mathbf{S}_{R\alpha,R'\alpha'}^{(2)} (\mathbf{T}_R^{\uparrow\downarrow} + \mathbf{T}_{R'}^{\uparrow\downarrow}) \otimes \mathbf{T}_{RR'} + \mathbf{S}_{R\alpha,R'\alpha'}^{(3)} \mathbf{p}_R^\downarrow \otimes \mathbf{p}_{R'}^\downarrow \otimes \mathbf{T}_{RR'} \\ &\quad \left. + \mathbf{S}_{R\alpha,R'\alpha'}^{(4)} (\mathbf{p}_R^\downarrow \otimes \mathbf{T}_{R'}^{\uparrow\downarrow} + \mathbf{p}_{R'}^\downarrow \otimes \mathbf{T}_R^{\uparrow\downarrow}) \otimes \mathbf{T}_{RR'} + \mathbf{S}_{R\alpha,R'\alpha'}^{(5)} \mathbf{T}_R^{\uparrow\downarrow} \otimes \mathbf{T}_{R'}^{\uparrow\downarrow} \otimes \mathbf{T}_{RR'} \right] \end{aligned} \quad (6.12)$$

where

$$\begin{aligned}\mathbf{S}^{(1)} &= (y - x) \widehat{\mathbf{S}}^{(1)}, \quad \mathbf{S}^{(2)} = \sqrt{xy} \widehat{\mathbf{S}}^{(1)}, \\ \mathbf{S}^{(3)} &= (y - x)^2 \widehat{\mathbf{S}}^{(2)}, \quad \mathbf{S}^{(4)} = \sqrt{xy} (y - x) \widehat{\mathbf{S}}^{(2)}, \\ \mathbf{S}^{(5)} &= xy \widehat{\mathbf{S}}^{(2)}.\end{aligned}$$

and

$$\begin{aligned}\widehat{\mathbf{S}}_{R\alpha,R'\beta}^{(1)} &= x (\widehat{\mathbf{S}}_{R\alpha,R'\beta}^{AA} - \widehat{\mathbf{S}}_{R\alpha,R'\beta}^{AB}) - y (\widehat{\mathbf{S}}_{R\alpha,R'\beta}^{BB} - \widehat{\mathbf{S}}_{R\alpha,R'\beta}^{BA}) \\ \widehat{\mathbf{S}}_{R\alpha,R'\beta}^{(2)} &= \widehat{\mathbf{S}}_{R\alpha,R'\beta}^{AA} + \widehat{\mathbf{S}}_{R\alpha,R'\beta}^{BB} - \widehat{\mathbf{S}}_{R\alpha,R'\beta}^{AB} - \widehat{\mathbf{S}}_{R\alpha,R'\beta}^{BA}.\end{aligned}$$

We now start to set up the scattering diagrams for the thermal conductivity. A look at Equation. (6.12) shows us that the first term is the averaged VCA current. This term is absorbed in the unscattered part of the phonon green function and leads to the zero-th

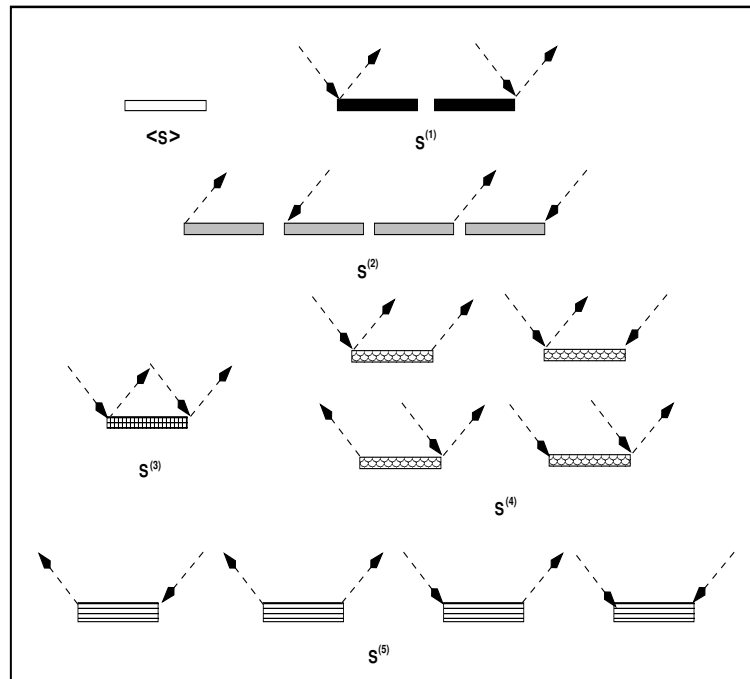


Figure 6.2: The scattering vertices associated with the random current terms

order approximation. Equation. (6.12) looks very similar to Equation. (6.10) from the operator point of view. The only difference is that the former equation arises due to the disorder in heat currents while the latter equation due to the disorder in the dynamical matrix. Exactly as before we can associate scattering vertices with the terms in $\tilde{\mathbf{S}}$. Fig. (6.2) shows sixteen different scattering vertices arising out of the equation (6.12). Let us now discuss how the scattering diagrams are set up and then examine them. The rule for obtaining the diagrams for the correlation function $\ll \kappa(z_1, z_2) \gg$ is as follows : Take any two current diagrams from Fig. (6.2) and two propagators and join them end to end. Now join the configuration fluctuation lines (shown as dashed arrows) in all possible ways. The zero-th order approximation for $\ll \kappa(z_1, z_2) \gg$ can be shown diagrammatically as in Fig. (6.3). The most dominant contribution comes from this particular diagram. Here the two current terms are the averaged current, and all configuration fluctuation decorations renormalize only the two phonon propagators. The bold propagators in this diagram are fully scattering renormalized propagators corresponding to the configuration averaged green function. The contribution of this term to the correlation function $\ll \kappa(z_1, z_2) \gg$

is

$$\int \frac{d^3\mathbf{k}}{8\pi^3} \ll \hat{\mathbf{S}}(\mathbf{k}) \gg \ll \mathbf{G}(\mathbf{k}, z_1) \gg \ll \hat{\mathbf{S}}(\mathbf{k}) \gg \ll \mathbf{G}(\mathbf{k}, z_2) \gg. \quad (6.13)$$

The rest of the terms in Equation. (6.12) give rise to scattering. We shall now focus on

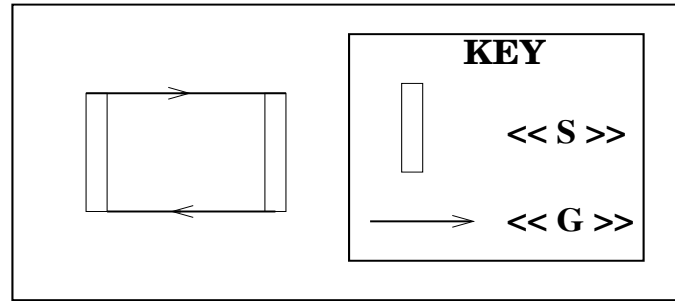


Figure 6.3: The VCA or zero-th order approximation for $\ll \kappa(z_1, z_2) \gg$.

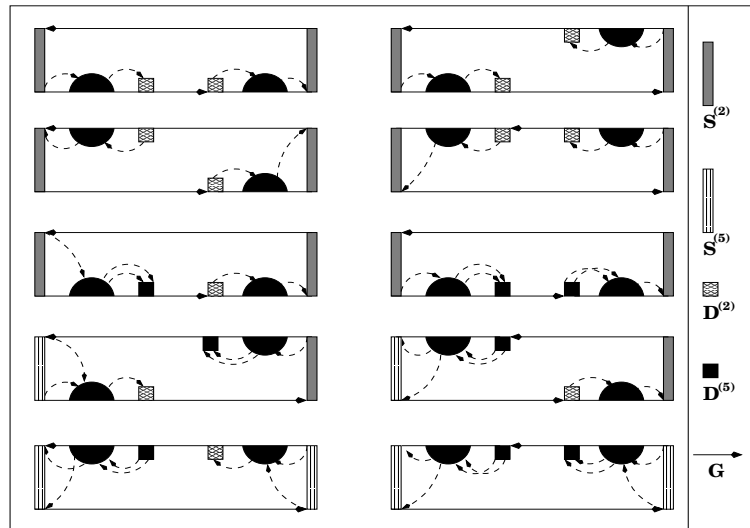


Figure 6.4: Few examples of scattering diagrams where no disorder line joins the two phonon propagators.

the main correction terms to the expression in Equation. (6.13). These are the correction terms to the averaged current which, as we will show, are closely related to the self-energies. The first type of scattering diagrams are those in which no disorder propagator (shown as the dashed lines) joins either two phonon propagators or two of the current lines directly. Fig. (6.4) shows few such scattering diagrams. These sets of diagrams may be

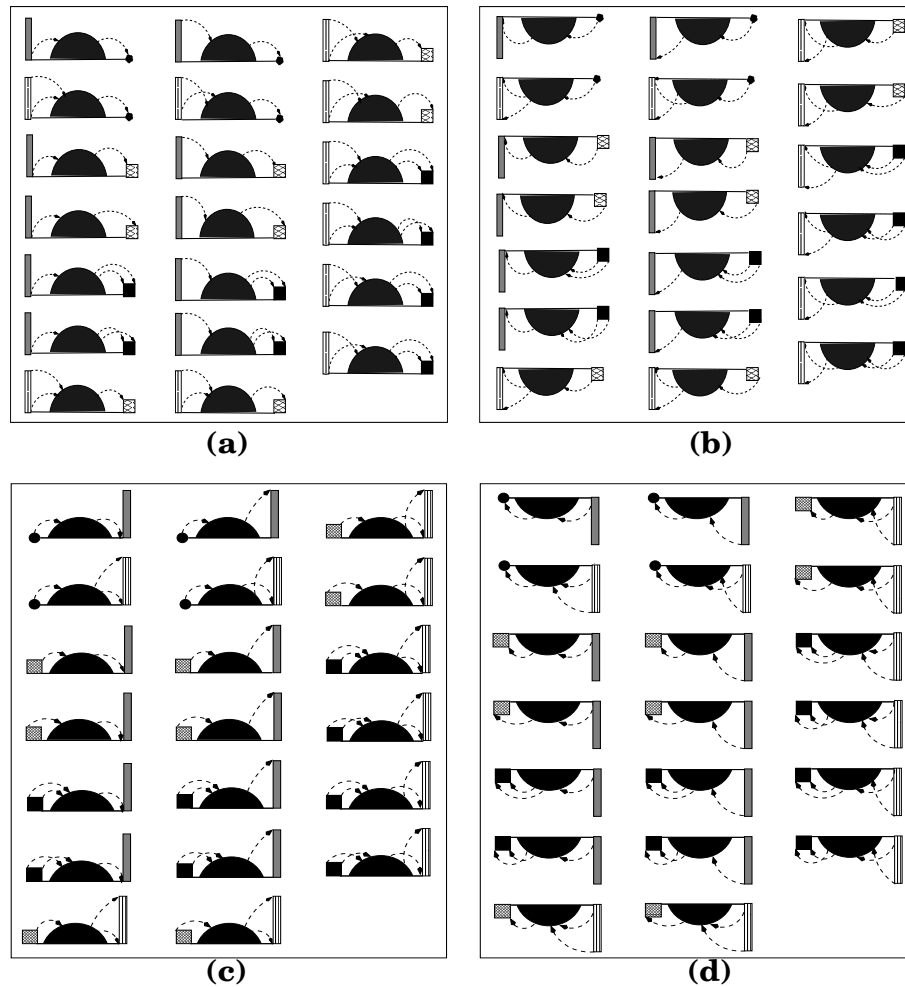


Figure 6.5: Scattering diagrams contributing to effective heat current.

clubbed together and renormalized in a form which will consist of two fully renormalized phonon propagators connected at the two ends by a new form of the renormalized current. This new form of the renormalized current may be obtained in the following way.

Fig. (6.4) clearly shows that these types of diagrams are made out of a left *renormalized* current diagram chosen out of any one of the diagrams from (a,b) in Fig. (6.5) and one right *renormalized* current diagram from any one of the diagram (c,d) of Fig. (6.5) connected by two *renormalized* propagators. Let us now obtain expressions for the renormalized currents. A careful look at the self-energy diagrams (See Fig. (5.7) of the previous

chapter) shows that all self-energy diagrams have the structure

$$\Sigma(\mathbf{k}, z) = \Delta(\mathbf{k}, z) \Omega(\mathbf{k}, z) \Delta(\mathbf{k}, z) \quad (6.14)$$

Where $\Omega(\mathbf{k}, z)$ is the Fourier transform of

$$\Omega_{RR'}(z) = \sum_{R_1 R_2} G_{RR_1}(z) P_{R_1 R_2}^{RR'}(z) G_{R_2 R'}(z) \quad (6.15)$$

and

$$\Delta(\mathbf{k}, z) = \mathbf{F} z^2 + 2 \Delta^{(2)}(\mathbf{k}) + 2 \Delta^{(5)}(\mathbf{k}).$$

In the above equation, the quantity ‘ P ’ stands for the central dark semicircle of Fig. (5.7) of chapter(5) which represents all possible arrangements of scattering vertices to all orders.

If we compare the diagrams of Fig. 6.5(a) with the diagrams for the self energy Fig. (5.7), we note that the only difference between the two is that the left most scattering vertex is replaced by a very similar current term. In the diagrams of Fig. 6.5(a), the left most diagonal terms similar to the vertex \mathbf{F} of Fig. (6.1) is off course missing. The contribution of such diagrams may be written in a mathematical form as

$$\left(2 \mathbf{S}^{(2)}(\mathbf{k}) + 2 \mathbf{S}^{(5)}(\mathbf{k}) \right) \Omega(\mathbf{k}, z) \Delta(\mathbf{k}, z)$$

which may be expressed in terms of the self energy ‘ Σ ’ by using Equation. (6.14) as

$$\left(2 \mathbf{S}^{(2)}(\mathbf{k}) + 2 \mathbf{S}^{(5)}(\mathbf{k}) \right) \left[\Delta(\mathbf{k}, z_1) \right]^{-1} \Sigma(\mathbf{k}, z_1).$$

The contribution of the diagrams in Fig. 6.5(b) is

$$\Sigma(\mathbf{k}, z_2) \left[\Delta(\mathbf{k}, z_2) \right]^{-1} \left(2 \mathbf{S}^{(2)}(\mathbf{k}) + 2 \mathbf{S}^{(5)}(\mathbf{k}) \right).$$

Similarly the contribution of the diagrams in Fig. 6.5(c) and Fig. 6.5(d) are respectively given by

$$\Sigma(\mathbf{k}, z_1) \left[\Delta(\mathbf{k}, z_1) \right]^{-1} \left(2 \mathbf{S}^{(2)}(\mathbf{k}) + 2 \mathbf{S}^{(5)}(\mathbf{k}) \right) \& \left(2 \mathbf{S}^{(2)}(\mathbf{k}) + 2 \mathbf{S}^{(5)}(\mathbf{k}) \right) \left[\Delta(\mathbf{k}, z_2) \right]^{-1} \Sigma(\mathbf{k}, z_2)$$

The next most dominant disorder corrections come from a group of diagrams which describe joint fluctuation of one current and two propagators. A few such diagrams are shown in Fig. (6.6).

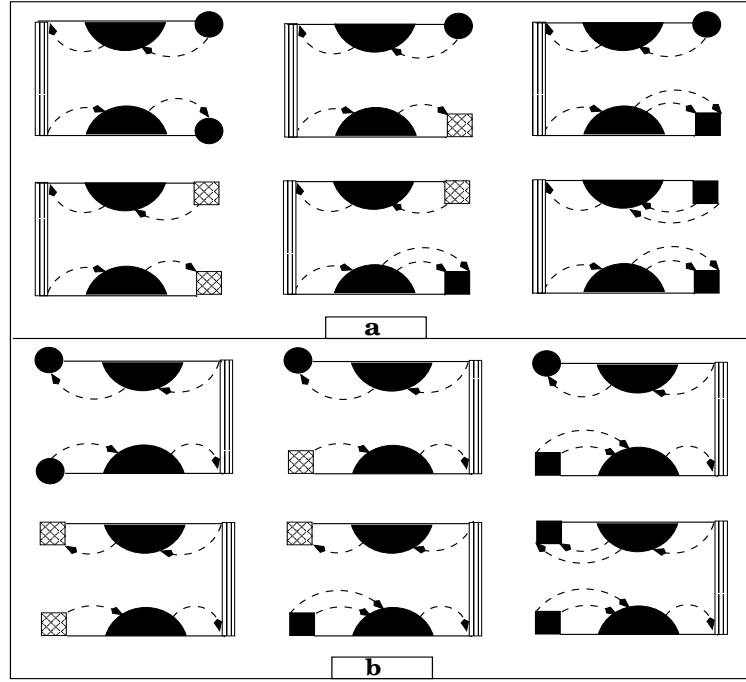


Figure 6.6: The scattering diagrams associated with joint fluctuations of one current term and two propagators.

The contributions of these diagrams [Fig. 6.6(a,b)] can also be expressed in terms of the self energy as,

$$\begin{aligned}
 (a) \quad & \Sigma(\mathbf{k}, z_2) \left[\Delta(\mathbf{k}, z_2) \right]^{-1} \mathbf{S}^{(5)}(\mathbf{k}) \left[\Delta(\mathbf{k}, z_1) \right]^{-1} \Sigma(\mathbf{k}, z_1) \\
 (b) \quad & \Sigma(\mathbf{k}, z_1) \left[\Delta(\mathbf{k}, z_1) \right]^{-1} \mathbf{S}^{(5)}(\mathbf{k}) \left[\Delta(\mathbf{k}, z_2) \right]^{-1} \Sigma(\mathbf{k}, z_2).
 \end{aligned}$$

If we now gather all the contributions from these diagrams [From Fig. 6.5(a,b,c,d) and Fig. 6.6(a,b)], we may define a renormalized current term as follows :

$$\mathbf{S}_{\text{eff}}(\mathbf{k}, z_1, z_2) = \ll \hat{\mathbf{S}}(\mathbf{k}) \gg + \Delta \mathbf{S}_1(\mathbf{k}, z_1, z_2) + \Delta \mathbf{S}_2(\mathbf{k}, z_1, z_2) \quad (6.16)$$

where

$$\begin{aligned}
 \Delta \mathbf{S}_1(\mathbf{k}, z_1, z_2) &= 2 \left(\mathbf{S}^{(2)}(\mathbf{k}) + \mathbf{S}^{(5)}(\mathbf{k}) \right) \left[\Delta(\mathbf{k}, z_1) \right]^{-1} \Sigma(\mathbf{k}, z_1) + \\
 &\quad \Sigma(\mathbf{k}, z_2) \left[\Delta(\mathbf{k}, z_2) \right]^{-1} 2 \left(\mathbf{S}^{(2)}(\mathbf{k}) + \mathbf{S}^{(5)}(\mathbf{k}) \right) \\
 \Delta \mathbf{S}_2(\mathbf{k}, z_1, z_2) &= \Sigma(\mathbf{k}, z_2) \left[\Delta(\mathbf{k}, z_2) \right]^{-1} \mathbf{S}^{(5)}(\mathbf{k}) \left[\Delta(\mathbf{k}, z_1) \right]^{-1} \Sigma(\mathbf{k}, z_1).
 \end{aligned}$$

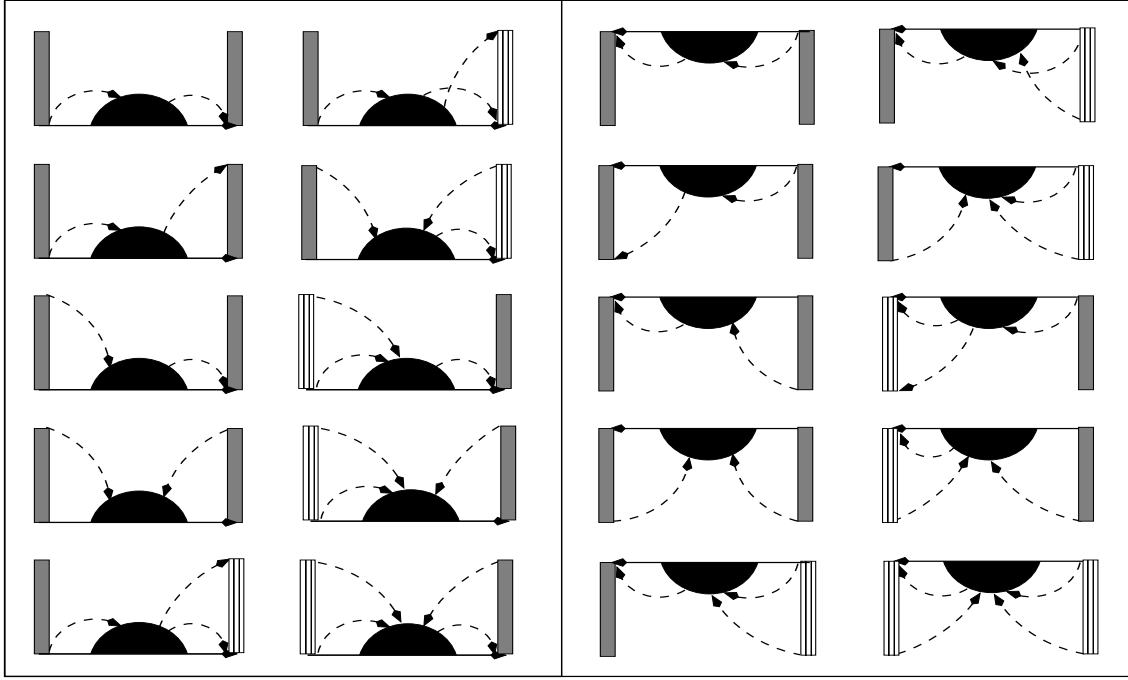


Figure 6.7: The scattering diagrams associated with joint fluctuations of two current terms and one propagator.

The contribution of these disorder-renormalized currents and propagators to the correlation function is

$$\ll \kappa_{(1)}(z_1, z_2) \gg = \int \frac{d^3 \mathbf{k}}{8\pi^3} \text{Tr} \left[\mathbf{S}_{\text{eff}}(\mathbf{k}, z_1, z_2) \ll \mathbf{G}(\mathbf{k}, z_1) \gg \mathbf{S}_{\text{eff}}^\dagger(\mathbf{k}, z_1, z_2) \ll \mathbf{G}(\mathbf{k}, z_2) \gg \right]. \quad (6.17)$$

We shall now discuss the disorder correction terms which involve joint fluctuations between the two current terms and one propagator. Few such diagrams are shown in Fig. (6.7). A close inspection of these diagrams shows that these are also related to the self energy diagrams with vertices at both ends replaced by currents. The corrections due to these terms can therefore be related to the self-energy as before. The contribution of these diagrams to the correlation function is given by

$$\ll \kappa_{(2)}(z_1, z_2) \gg = 4 \int \frac{d^3 \mathbf{k}}{8\pi^3} \text{Tr} \left[\Delta \mathbf{S}_3(\mathbf{k}, z_1) \ll \mathbf{G}(\mathbf{k}, z_2) \gg + \Delta \mathbf{S}_4(\mathbf{k}, z_2) \ll \mathbf{G}(\mathbf{k}, z_1) \gg \right]. \quad (6.18)$$

where

$$\begin{aligned}\Delta\mathbf{S}_3(\mathbf{k}, z_1) &= \left(\mathbf{S}^{(2)}(\mathbf{k}) + \mathbf{S}^{(5)}(\mathbf{k})\right) \left[\Delta(\mathbf{k}, z_1)\right]^{-1} \boldsymbol{\Sigma}(\mathbf{k}, z_1) \left[\Delta(\mathbf{k}, z_1)\right]^{-1} \left(\mathbf{S}^{(2)}(\mathbf{k}) + \mathbf{S}^{(5)}(\mathbf{k})\right)^\dagger \\ \Delta\mathbf{S}_4(\mathbf{k}, z_2) &= \left(\mathbf{S}^{(2)}(\mathbf{k}) + \mathbf{S}^{(5)}(\mathbf{k})\right) \left[\Delta(\mathbf{k}, z_2)\right]^{-1} \boldsymbol{\Sigma}(\mathbf{k}, z_2) \left[\Delta(\mathbf{k}, z_2)\right]^{-1} \left(\mathbf{S}^{(2)}(\mathbf{k}) + \mathbf{S}^{(5)}(\mathbf{k})\right)^\dagger.\end{aligned}$$

In an earlier paper [Saha and Mookerjee 2004] on a similar problem, we have argued that these are the dominant disorder corrections to the average current. Intuitively we also expect the same to be true in the present case as well. It is important to note that these corrections can be obtained from the self-energy and is therefore eminently computationally feasible in the case of realistic alloys, once we have a feasible method for obtaining the self-energy.

There are other scattering diagrams which are not related to the self-energy but rather to the vertex corrections. In these diagrams, a disorder line connects both the phonon propagators directly. We expect the corrections from these types of diagrams to be less dominant. For the sake of completeness, we shall indicate in detail how to obtain them within a ladder diagram approximation in the next section.

6.3.2 The vertex correction

The vertex corrections are basically those scattering diagrams in which disorder lines connect both the propagators directly. We have not yet incorporated these kinds of diagrams in the disorder renormalization. These types of diagrams arise due to the correlated propagation. The diagrams leading to the vertex corrections may be of different kinds *e.g.* ladder diagrams, maximally crossed diagrams etc. The ladder diagrams are those diagrams which are built out of repeated vertices shown on the first line of Fig. (6.8). These kinds of diagrams can be summed up to all orders. This is the disorder scattering version of the *random-phase approximation* (RPA) for the phonon-phonon scattering. The maximally crossed diagrams are those diagrams in which the ladder inserts between the crossed vertices. These types of diagrams are shown in the second line of Fig. (6.8). In general we obtain a Bethe-Salpeter equation for the averaged two particle propagator. This is diagrammatically shown in Fig. (6.9). Here we shall consider the ladder diagrams in detail and show how to obtain the contribution of these diagrams in terms of mathematical

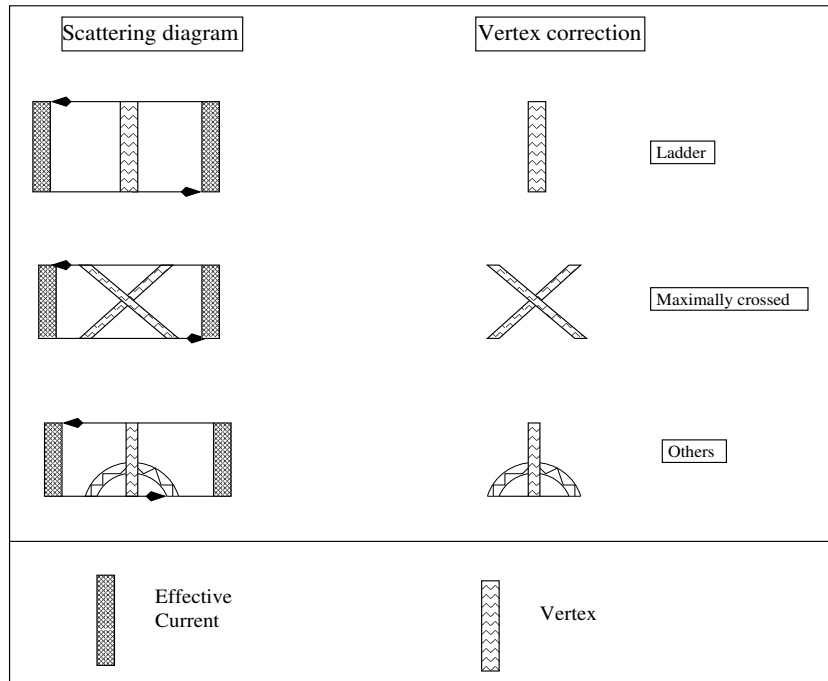


Figure 6.8: The scattering diagrams leading to vertex correction.

expression. We then sum these ladder diagrams to all orders. The possible scattering diagrams for the ladder kind of vertex correction involving the vertices \mathbf{B} , \mathbf{F} , $\mathbf{D}^{(1)}$ to $\mathbf{D}^{(5)}$ are as shown in Fig. (6.10). The contribution of seven categories (A-G) of the ladder scattering diagrams in terms of mathematical expression are as given below.

Category A

$$\left(W_{\alpha\beta}^{\gamma\delta}\right)_A = (z_1 z_2)^2 F_\alpha F_\gamma \delta_{\alpha\beta} \delta_{\gamma\delta} + 2 z_2^2 D_{\alpha\beta}^{(2)} F^\gamma \delta_{\gamma\delta}$$

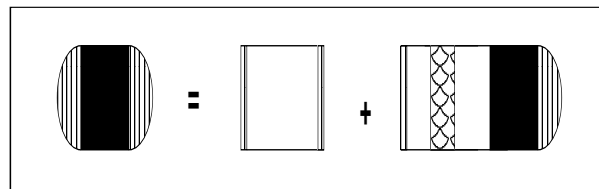


Figure 6.9: The Bethe-Salpeter equation for the thermal conductivity

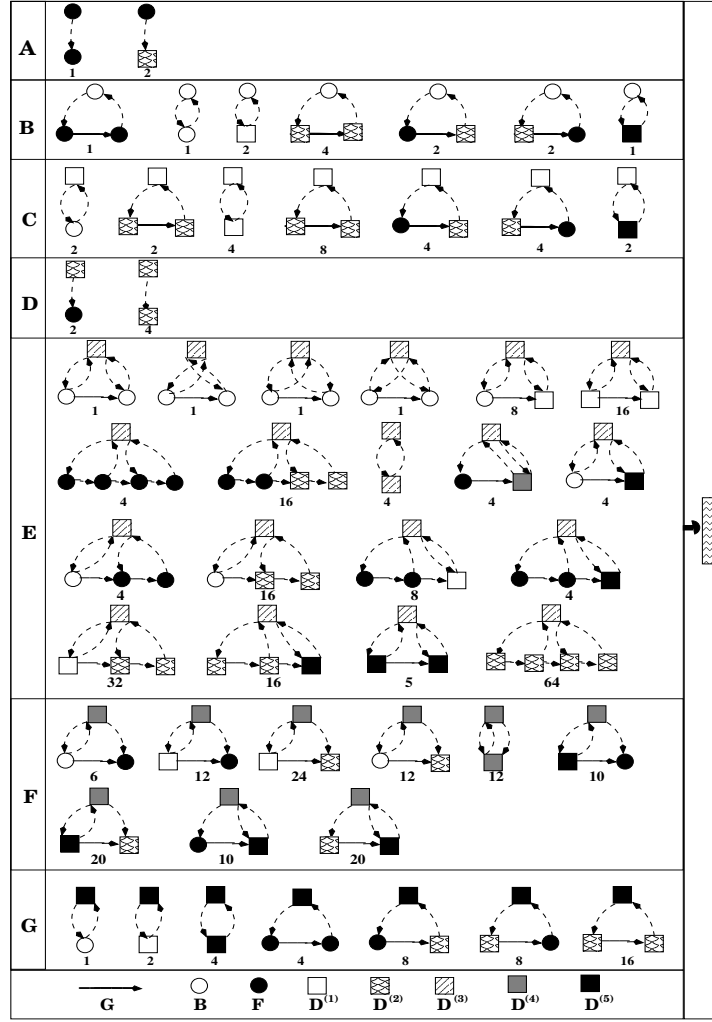


Figure 6.10: The ladder scattering diagrams for the vertex correction.

Category B

$$\begin{aligned}
(W_{\alpha\beta}^{\gamma\delta})_B &= (z_1^2 z_2)^2 \left[\sum_{\nu'\nu''} (F_{\alpha\nu'} \delta_{\alpha\nu'}) G_{R\nu', R\nu''} (F_{\nu''\beta} \delta_{\nu''\beta}) \right] (B_{\nu\delta} \delta_{\nu\delta}) \\
&+ (z_1^2 B_{\alpha\beta} \delta_{\alpha\beta}) (z_2^2 B_{\nu\delta} \delta_{\nu\delta}) + 2 \left[D_{\alpha\beta}^{(1)} (z_2^2 B_{\nu\delta} \delta_{\nu\delta}) \right] + 4 \left[\sum_{\nu'\nu''} D_{\alpha\nu'}^{(2)} G_{R\nu', R\nu''} D_{\nu''\beta}^{(2)} \right] \\
&\quad \times (z_2^2 B_{\nu\delta} \delta_{\nu\delta}) + 2 \left[\sum_{\nu'\nu''} (z_1^2 F_{\alpha\nu'} \delta_{\alpha\nu'}) G_{R\nu', R\nu''} D_{\nu''\beta}^{(2)} \right] (z_2^2 B_{\nu\delta} \delta_{\nu\delta}) \\
&2 \left[\sum_{\nu'\nu''} D_{\alpha\nu'}^{(2)} G_{R\nu', R\nu''} (z_1^2 F_{\nu''\beta} \delta_{\nu''\beta}) \right] (z_2^2 B_{\nu\delta} \delta_{\nu\delta}) + D_{\alpha\beta}^{(5)} (z_2^2 B_{\nu\delta} \delta_{\nu\delta}).
\end{aligned}$$

Category C

$$\begin{aligned}
(W_{\alpha\beta}^{\gamma\delta})_C &= 2 \left[(z_1^2 B_{\alpha\beta} \delta_{\alpha\beta}) D_{\nu\delta}^{(1)} \right] + 2 \left[\sum_{\nu'\nu''} (z_1^2 F_{\alpha\nu'} \delta_{\alpha\nu'}) G_{R\nu',R\nu''} (z_1^2 F_{\nu''\beta} \delta_{\nu''\beta}) \right] D_{\nu\delta}^{(1)} \\
&+ 4 D_{\alpha\beta}^{(1)} D_{\nu\delta}^{(1)} + 8 \left[\sum_{\nu'\nu''} D_{\alpha\nu'}^{(2)} G_{R\nu',R\nu''} D_{\nu''\beta}^{(2)} \right] D_{\nu\delta}^{(1)} + 4 \left[\sum_{\nu'\nu''} (z_1^2 F_{\alpha\nu'} \delta_{\alpha\nu'}) \right. \\
&\quad \left. G_{R\nu',R\nu''} D_{\nu''\beta}^{(2)} \right] D_{\nu\delta}^{(1)} + 2 \left[\sum_{\nu'\nu''} D_{\alpha\nu'}^{(2)} G_{R\nu',R\nu''} (z_1^2 F_{\nu''\beta} \delta_{\nu''\beta}) \right] D_{\nu\delta}^{(1)}
\end{aligned}$$

Category D

$$(W_{\alpha\beta}^{\gamma\delta})_D = 2 \left[(z_1^2 F_{\alpha\beta} \delta_{\alpha\beta}) D_{\nu\delta}^{(2)} \right] + 4 D_{\alpha\beta}^{(2)} D_{\nu\delta}^{(2)}$$

Category E

$$\begin{aligned}
(W_{\alpha\beta}^{\gamma\delta})_E &= 2 \left[\sum_{\nu'\nu''} (z_1^2 B_{\alpha\nu'} \delta_{\alpha\nu'}) G_{R\nu',R\nu''} (z_1^2 B_{\nu''\beta} \delta_{\nu''\beta}) \right] D_{\nu\delta}^{(3)} + 8 \left[\sum_{\nu'\nu''} (z_1^2 B_{\alpha\nu'} \delta_{\alpha\nu'}) \right. \\
&\quad \left. G_{R\nu',R\nu''} D_{\nu''\beta}^{(1)} \right] D_{\nu\delta}^{(3)} + 16 \left[\sum_{\nu'\nu''} D_{\alpha\nu'}^{(1)} G_{R\nu',R\nu''} D_{\nu''\beta}^{(1)} \right] D_{\nu\delta}^{(3)} + \\
&+ 4 \left[\sum_{\nu_1 \dots \nu_6} (z_1^2 F_{\alpha\nu_1} \delta_{\alpha\nu_1}) G_{R\nu_1,R\nu_2} (z_1^2 F_{\nu_2\nu_3} \delta_{\nu_2\nu_3}) G_{R\nu_3,R\nu_4} (z_1^2 F_{\nu_4\nu_5} \delta_{\nu_4\nu_5}) \right. \\
&\quad \left. G_{R\nu_5,R\nu_6} (z_1^2 F_{\nu_6\beta} \delta_{\nu_6\beta}) \right] D_{\nu\delta}^{(3)} + 16 \left[\sum_{\nu_1 \dots \nu_6} (z_1^2 F_{\alpha\nu_1} \delta_{\alpha\nu_1}) G_{R\nu_1,R\nu_2} \right. \\
&\quad \left. (z_1^2 F_{\nu_2\nu_3} \delta_{\nu_2\nu_3}) G_{R\nu_3,R\nu_4} D_{\nu_4\nu_5}^{(2)} G_{R\nu_5,R\nu_6} D_{\nu_6\beta}^{(2)} \right] D_{\nu\delta}^{(3)} + 4 D_{\alpha\beta}^{(3)} D_{\nu\delta}^{(3)} \\
&+ 4 \left[\sum_{\nu'\nu''} (z_1^2 F_{\alpha\nu'} \delta_{\alpha\nu'}) G_{R\nu',R\nu''} D_{\nu''\beta}^{(4)} \right] D_{\nu\delta}^{(3)} + 4 \left[\sum_{\nu'\nu''} (z_1^2 F_{\alpha\nu'} \delta_{\alpha\nu'}) \right. \\
&\quad \left. G_{R\nu',R\nu''} D_{\nu''\beta}^{(5)} \right] D_{\nu\delta}^{(3)} + 4 \left[\sum_{\nu_1 \dots \nu_4} (z_1^2 B_{\alpha\nu_1} \delta_{\alpha\nu_1}) G_{R\nu_1,R\nu_2} (z_1^2 F_{\nu_2\nu_3} \delta_{\nu_2\nu_3}) \right. \\
&\quad \left. G_{R\nu_3,R\nu_4} (z_1^2 F_{\nu_4\delta} \delta_{\nu_4\delta}) \right] D_{\nu\delta}^{(3)} + 16 \left[\sum_{\nu_1 \dots \nu_4} (z_1^2 B_{\alpha\nu_1} \delta_{\alpha\nu_1}) G_{R\nu_1,R\nu_2} (D_{\nu_2\nu_3}^{(2)}) \right. \\
&\quad \left. G_{R\nu_3,R\nu_4} (D_{\nu_4\beta}^{(2)}) \right] D_{\nu\delta}^{(3)} + 8 \left[\sum_{\nu_1 \dots \nu_4} (z_1^2 F_{\alpha\nu_1} \delta_{\alpha\nu_1}) G_{R\nu_1,R\nu_2} (z_1^2 F_{\nu_2\nu_3} \delta_{\nu_2\nu_3}) \right.
\end{aligned}$$

$$\begin{aligned}
& G_{R\nu_3, R\nu_4} (D_{\nu_4\beta}^{(1)}) \Big] D_{\nu\delta}^{(3)} + 4 \left[\sum_{\nu_1 \dots \nu_4} (z_1^2 F_{\alpha\nu_1} \delta_{\alpha\nu_1}) G_{R\nu_1, R\nu_2} (z_1^2 F_{\nu_2\nu_3} \delta_{\nu_2\nu_3}) \right. \\
& G_{R\nu_3, R\nu_4} (D_{\nu_4\beta}^{(5)}) \Big] D_{\nu\delta}^{(3)} + 32 \left[\sum_{\nu_1 \dots \nu_4} (D_{\alpha\nu_1}^{(1)}) G_{R\nu_1, R\nu_2} (D_{\nu_2\nu_3}^{(2)}) G_{R\nu_3, R\nu_4} (D_{\nu_4\beta}^{(2)}) \right] \\
& D_{\nu\delta}^{(3)} + 16 \left[\sum_{\nu_1 \dots \nu_4} (D_{\alpha\nu_1}^{(2)}) G_{R\nu_1, R\nu_2} (D_{\nu_2\nu_3}^{(2)}) G_{R\nu_3, R\nu_4} (D_{\nu_4\beta}^{(5)}) \right] D_{\nu\delta}^{(3)} \\
& + 5 \left[\sum_{\nu' \nu''} (D_{\alpha\nu'}^{(5)}) G_{R\nu', R\nu''} (D_{\nu''\beta}^{(5)}) \right] D_{\nu\delta}^{(3)} + 64 \left[\sum_{\nu_1 \dots \nu_6} (D_{\alpha\nu_1}^{(2)}) G_{R\nu_1, R\nu_2} (D_{\nu_2\nu_3}^{(2)}) \right. \\
& \left. G_{R\nu_3, R\nu_4} (D_{\nu_4\nu_5}^{(2)}) G_{R\nu_5, R\nu_6} (D_{\nu_6\beta}^{(2)}) \right] D_{\nu\delta}^{(3)}
\end{aligned}$$

Category F

$$\begin{aligned}
(W_{\alpha\beta}^{\gamma\delta})_F &= 6 \left[\sum_{\nu' \nu''} (z_1^2 B_{\alpha\nu'} \delta_{\alpha\nu'}) G_{R\nu', R\nu''} (z_1^2 F_{\nu''\beta} \delta_{\nu''\beta}) \right] D_{\nu\delta}^{(4)} + 12 \left[\sum_{\nu' \nu''} (D_{\alpha\nu'}^{(1)}) G_{R\nu', R\nu''} \right. \\
& \left. (z_1^2 F_{\nu''\beta} \delta_{\nu''\beta}) \right] D_{\nu\delta}^{(4)} + 24 \left[\sum_{\nu' \nu''} (D_{\alpha\nu'}^{(1)}) G_{R\nu', R\nu''} (D_{\nu''\beta}^{(2)}) \right] D_{\nu\delta}^{(4)} \\
& + 12 \left[\sum_{\nu' \nu''} (z_1^2 B_{\alpha\nu'} \delta_{\alpha\nu'}) G_{R\nu', R\nu''} (D_{\nu''\beta}^{(2)}) \right] D_{\nu\delta}^{(4)} + 12 D_{\alpha\beta}^{(4)} D_{\nu\delta}^{(4)} \\
& + 10 \left[\sum_{\nu' \nu''} (D_{\alpha\nu'}^{(5)}) G_{R\nu', R\nu''} (z_1^2 F_{\nu''\beta} \delta_{\nu''\beta}) \right] D_{\nu\delta}^{(4)} + 20 \left[\sum_{\nu' \nu''} (D_{\alpha\nu'}^{(5)}) G_{R\nu', R\nu''} \right. \\
& \left. \times (D_{\nu''\beta}^{(2)}) \right] D_{\nu\delta}^{(4)} + 10 \left[\sum_{\nu' \nu''} (z_1^2 F_{\alpha\nu'} \delta_{\alpha\nu'}) G_{R\nu', R\nu''} (D_{\nu''\beta}^{(5)}) \right] D_{\nu\delta}^{(4)} \\
& + 20 \left[\sum_{\nu' \nu''} (D_{\alpha\nu'}^{(2)}) G_{R\nu', R\nu''} (D_{\nu''\beta}^{(5)}) \right] D_{\nu\delta}^{(4)}
\end{aligned}$$

Category G

$$\begin{aligned}
(W_{\alpha\beta}^{\gamma\delta})_G &= (z_1^2 B_{\alpha\beta} \delta_{\alpha\beta}) D_{\nu\delta}^{(5)} + 2D_{\alpha\beta}^{(1)} D_{\nu\delta}^{(5)} + 4D_{\alpha\beta}^{(5)} D_{\nu\delta}^{(5)} + 4 \left[\sum_{\nu' \nu''} (z_1^2 F_{\alpha\nu'} \delta_{\alpha\nu'}) G_{R\nu', R\nu''} \right. \\
& \left. (z_1^2 F_{\nu''\beta} \delta_{\nu''\beta}) \right] D_{\nu\delta}^{(5)} + 8 \left[\sum_{\nu' \nu''} (z_1^2 F_{\alpha\nu'} \delta_{\alpha\nu'}) G_{R\nu', R\nu''} (D_{\nu''\beta}^{(2)}) \right] D_{\nu\delta}^{(5)} \\
& + 8 \left[\sum_{\nu' \nu''} (D_{\alpha\nu'}^{(2)}) G_{R\nu', R\nu''} (z_1^2 F_{\nu''\beta} \delta_{\nu''\beta}) \right] D_{\nu\delta}^{(5)} \\
& + 16 \left[\sum_{\nu' \nu''} (D_{\alpha\nu'}^{(2)}) G_{R\nu', R\nu''} (D_{\nu''\beta}^{(2)}) \right] D_{\nu\delta}^{(5)}
\end{aligned}$$

Therefore, the sum of all possible scattering diagrams contributing to the four legged vertex (shown in the extreme right column of Fig. (6.10)) will be given by

$$W_{\alpha\beta}^{\gamma\delta} = \sum_{i=A}^G (W_{\alpha\beta}^{\gamma\delta})_i$$

Here we shall sum the ladder diagrams to all orders. The contribution of a single ladder diagram to the correlation function as shown in the top line of Fig. (6.11) is

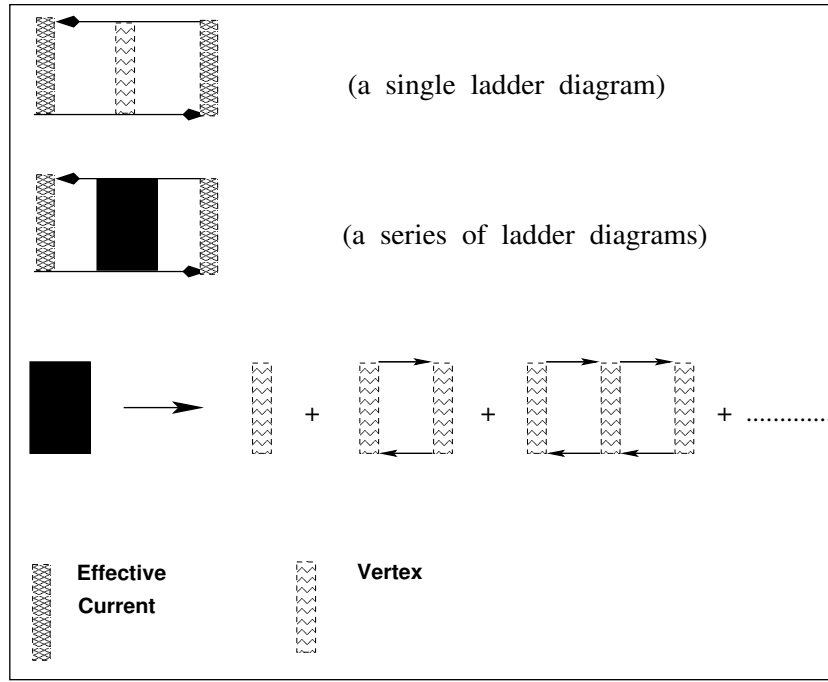


Figure 6.11: The structure of infinite series of ladder diagrams contributing to the correlation function $\ll \kappa(z_1, z_2) \gg$.

$$\sum_{R_1 R_2} \sum_{R_3 R_4} \sum_{R_5} \sum_{\alpha_1 \alpha_2} \sum_{\alpha_3 \alpha_4} \sum_{\alpha_5 \alpha_6} S_{R_5 \alpha_6, R_1 \alpha_1}^{\text{eff}} G_{R_1 \alpha_1, R_2 \alpha_2}(z_1) W_{\alpha_2 \alpha_2}^{\alpha_5 \alpha_5} G_{R_2 \alpha_2, R_3 \alpha_3}(z_1) (S_{R_3 \alpha_3, R_4 \alpha_4}^{\text{eff}})^\dagger G_{R_4 \alpha_4, R_2 \alpha_5}(z_2) G_{R_2 \alpha_5, R_5 \alpha_6}(z_2) \quad (6.19)$$

If we apply the homogeneity in full augmented space, it will imply that the above expression is independent of ‘R’ which allows us to take the Fourier transform leading to

$$\left[\int_{BIZ} \frac{d^3 \mathbf{k}}{8\pi^3} \mathbf{G}(\mathbf{k}, z_2) \mathbf{S}^{\text{eff}}(\mathbf{k}, z_1, z_2) \mathbf{G}(\mathbf{k}, z_1) \right] \mathbf{W}$$

$$\left[\int_{BIZ} \frac{d^3\mathbf{k}'}{8\pi^3} \mathbf{G}(\mathbf{k}', z_1) \left(\mathbf{S}^{\text{eff}}(\mathbf{k}', z_1, z_2) \right)^\dagger \mathbf{G}(\mathbf{k}', z_2) \right] = \mathbf{\Gamma}(z_1, z_2) \mathbf{W} \hat{\mathbf{\Gamma}}(z_1, z_2)$$

where we have defined

$$\begin{aligned} \mathbf{\Gamma}(z_1, z_2) &= \int_{BIZ} \frac{d^3\mathbf{k}}{8\pi^3} \mathbf{G}(\mathbf{k}, z_2) \mathbf{S}^{\text{eff}}(\mathbf{k}, z_1, z_2) \mathbf{G}(\mathbf{k}, z_1), \\ \hat{\mathbf{\Gamma}}(z_1, z_2) &= \int_{BIZ} \frac{d^3\mathbf{k}'}{8\pi^3} \mathbf{G}(\mathbf{k}', z_1) \left(\mathbf{S}^{\text{eff}}(\mathbf{k}', z_1, z_2) \right)^\dagger \mathbf{G}(\mathbf{k}', z_2). \end{aligned}$$

Let us now look at the contribution of the infinite series of ladder diagrams (shown in the third column of Fig. (6.11)) to the correlation function. Each one of them has the same structure as Equation. (6.19), We may then sum up the series as follows :

Let us define

$$\Theta_{\alpha\beta}^{\gamma\delta}(z_1, z_2) = \int_{BIZ} \frac{d^3\mathbf{k}}{8\pi^3} G_{\alpha\beta}(\mathbf{k}, z_1) G_{\gamma\delta}(\mathbf{k}, z_2)$$

Then

$$\mathbf{\Lambda}(z_1, z_2) = \mathbf{W} + \mathbf{W}\Theta\mathbf{W} + \mathbf{W}\Theta\mathbf{W}\Theta\mathbf{W} + \dots = \mathbf{W}(z_1, z_2) \left(\mathbf{I} - \Theta(z_1, z_2) \mathbf{W}(z_1, z_2) \right)^{-1}.$$

Thus the contribution of the infinite series of ladder diagram vertex corrections to the correlation function may be expressed as

$$\begin{aligned} \ll \Delta\kappa(z_1, z_2)^{\text{ladder}} \gg &= \sum_{\alpha\beta} \sum_{\gamma\delta} \mathbf{\Gamma}_\beta^\alpha(z_1, z_2) \mathbf{\Lambda}_{\beta\delta}^{\alpha\nu}(z_1, z_2) \hat{\mathbf{\Gamma}}_\delta^\nu(z_1, z_2) \\ &= \text{Tr} \left[\mathbf{\Gamma}(z_1, z_2) \otimes \hat{\mathbf{\Gamma}}(z_1, z_2) \odot \mathbf{\Lambda}(z_1, z_2) \right]. \end{aligned} \quad (6.20)$$

Including all kinds of disorder corrections, the configuration average of the two-particle Green function (or the correlation function) now has the form,

$$\ll \kappa(z_1, z_2) \gg = \ll \kappa_{(1)}(z_1, z_2) \gg + \ll \kappa_{(2)}(z_1, z_2) \gg + \ll \Delta\kappa(z_1, z_2)^{\text{ladder}} \gg. \quad (6.21)$$

6.4 Configuration averaged thermal diffusivity

The thermal diffusivity D_γ for a harmonic solid is defined as

$$D_\gamma^{\mu\nu}(\mathbf{k}) = \pi \sum_{\gamma' \neq \gamma} \frac{1}{\omega_{\mathbf{k}\gamma}^2} \mathbf{S}_{\gamma\gamma'}^\mu(\mathbf{k}) \mathbf{S}_{\gamma'\gamma}^\nu(\mathbf{k}) \delta(\omega_{\mathbf{k}\gamma} - \omega_{\mathbf{k}\gamma'}).$$

This is an intrinsic property of the γ -th normal mode and provides an unambiguous criterion for localization.

The averaged thermal diffusivity (averaged over modes) is then given by

$$\begin{aligned} \mathbf{D}^{\mu\nu}(\omega) &= \frac{\int \frac{d^3\mathbf{k}}{8\pi^3} \sum_{\gamma} D_{\gamma}^{\mu\nu}(\mathbf{k}) \delta(\omega - \omega_{\mathbf{k}\gamma})}{\int \frac{d^3\mathbf{k}}{8\pi^3} \sum_{\gamma} \delta(\omega - \omega_{\mathbf{k}\gamma})} \\ &= \frac{D_{tot}^{\mu\nu}(\omega)}{\int \frac{d^3\mathbf{k}}{8\pi^3} \sum_{\gamma} \delta(\omega - \omega_{\mathbf{k}\gamma})}. \end{aligned} \quad (6.22)$$

Assuming isotropy of the response, we can rewrite the numerator of above equation as

$$D_{tot}^{\mu\mu}(\omega) = \pi \int d\omega' \int \frac{d^3\mathbf{k}}{8\pi^3} \sum_{\gamma} \sum_{\gamma'} \hat{S}_{\gamma\gamma'}^{\mu}(\mathbf{k}) \hat{S}_{\gamma'\gamma}^{\mu}(\mathbf{k}) \delta(\omega' - \omega_{\mathbf{k}\gamma'}) \delta(\omega_{\mathbf{k}\gamma} - \omega') \delta(\omega - \omega_{\mathbf{k}\gamma})$$

where

$$\hat{S}_{\gamma\gamma'}^{\mu}(\mathbf{k}) = \frac{1}{\omega_{\mathbf{k}\gamma}} \mathbf{S}_{\gamma\gamma'}^{\mu}(\mathbf{k}).$$

We may again rewrite the above equation for D_{tot} as

$$D_{tot}^{\mu\mu}(\omega) = \frac{1}{\pi^2} \int d\omega' \int \frac{d^3\mathbf{k}}{8\pi^3} \text{Tr} \left[\Im m \{ \mathbf{G}(\mathbf{k}, \omega') \} \hat{\mathbf{S}}^{\mu}(\mathbf{k}) \Im m \{ \mathbf{G}(\mathbf{k}, \omega') \} \hat{\mathbf{S}}^{\mu}(\mathbf{k}) \Im m \{ \mathbf{G}(\mathbf{k}, \omega) \} \right]$$

The averaged thermal diffusivity can then be expressed as (for an isotropic response)

$$\begin{aligned} \mathbf{D}(\omega) &= \frac{1}{3} \sum_{\mu} D^{\mu\mu}(\omega) \\ &= \frac{\pi}{3} \frac{\sum_{\mu} \mathbf{D}_{tot}^{\mu\mu}(\omega)}{\int \frac{d^3\mathbf{k}}{8\pi^3} \text{Tr} [\Im m \{ \mathbf{G}(\mathbf{k}, \omega) \}]} \end{aligned} \quad (6.23)$$

For disordered material, we shall be interested as before in obtaining the configuration averaged thermal diffusivity. We have already discussed the configuration averaging of the two particle Green function using scattering diagram technique in subsection (6.3.1). It has been found that the net effect is to replace the current terms by an effective heat current $\mathbf{S}_{eff}(\mathbf{k}, z_1, z_2)$. The effective current is a sum of average current and the terms arising out of the disorder correction. As in the case of optical conductivity calculation

[Saha and Mookerjee 2004], it will be shown that the overall contribution of disorder correction terms to the thermal conductivity is small as compared to the average current $\ll \hat{\mathbf{S}}(\mathbf{k}) \gg$. Keeping in mind this effect of disorder correction terms to the heat current, the configuration averaged thermal diffusivity can be expressed (to a 1st order approximation) in the form

$$\ll \mathbf{D}(\omega) \gg = \frac{\pi}{3} \frac{\sum_{\mu} \ll \mathbf{D}_{tot}^{\mu\mu}(\omega) \gg}{\int \frac{d^3\mathbf{k}}{8\pi^3} \text{Tr} [\Im m \ll \mathbf{G}(\mathbf{k}, \omega) \gg]} \quad (6.24)$$

where

$$\begin{aligned} \ll D_{tot}^{\mu\mu}(\omega) \gg \simeq & \frac{1}{\pi^2} \int d\omega' \int \frac{d^3\mathbf{k}}{8\pi^3} \text{Tr} \left[\Im m \ll \mathbf{G}(\mathbf{k}, \omega') \gg \right. \\ & \left. \ll \hat{\mathbf{S}}^{\mu}(\mathbf{k}) \Im m \{ \mathbf{G}(\mathbf{k}, \omega') \} \hat{\mathbf{S}}^{\mu}(\mathbf{k}) \Im m \{ \mathbf{G}(\mathbf{k}, \omega) \} \gg \right]. \end{aligned} \quad (6.25)$$

6.5 Details of Numerical Implementation

Although we have used the scattering diagrammatic technique to analyze the effects of disorder scattering on the thermal conductivity and obtain relation between the effective current and self-energy, we shall not use this approach to actually numerically obtain the thermal conductivity for a real alloy system. If we look at the earlier sections we note that what we need to obtain are essentially the configuration averaged Green matrices and the self energy matrices. For this we shall use the augmented space block-recursion [Alam and Mookerjee¹ 2005] and also the Brillouin zone integration scheme developed by us earlier [Saha *et al* 2005] for disordered alloys. In subsection (Godin and Haydock 1988, Godin and Haydock 1992) of chapter (1), we have already described the block recursion technique, which calculates the entire green matrix and the self energy matrix.

The need of efficient techniques for Brillouin zone (BZ) integration in solid state physics has been widely appreciated in recent years. Such techniques are of great importance in the numerical calculation of density of state, conductivity, susceptibility, dielectric function etc. The tetrahedron method allows us a very accurate k-space integration for both the spectral functions and conductivities for ordered systems. Recently our group has developed a generalization of this technique for disordered alloys. The spectral functions

are now no longer delta functions, but Lorentzians with a disorder induced non-zero half-widths [Saha *et al* 2005]. We will use the efficient codes developed by our group to carry out the integrations over the Brillouin zone. We refer the reader to the above referenced paper for details of the calculation.

6.6 Results and Discussion

The details of numerical calculation for the two alloys of our interest in the present work are as follows :

- We have carried out calculations on 501 ν -points.
- A small imaginary part of the frequency $\delta = 0.001$ has been used for evaluating the Green matrix and Self-energy matrix in the augmented space block recursion Alam and Mookerjee¹ 2005.
- The calculation of lattice conductivity has been done at 40 temperatures.
- For the Brillouin zone integration, 145 \mathbf{k} -points in the irreducible 1/48-th of the zone produced well converged results.

6.6.1 NiPd alloy : Strong mass and weak force constant disorder.

This particular alloy has already been studied experimentally by Farrell and Greig 1969 using conventional potentiometric techniques. But unfortunately their investigation was limited only to very dilute alloys in the temperature range 2-100 K.

Figure (6.12) shows the results for disordered $Ni_{50}Pd_{50}$ alloy. The black curve represents the lattice conductivity including all kinds of disorder induced corrections : e.g. corrections to the heat current and the vertex corrections, while the red curve stands for the same quantity but using averaged heat currents and without vertex corrections. The green curve in this figure shows the scaled joint density of states. From the figure it is clear that the transition rate ' τ ' is strongly dependent both on the initial and the final energies throughout the phonon frequency (ν). That is

$$\kappa(\nu, T) \neq |\tau(\nu, T)|J(\nu), \quad (6.26)$$

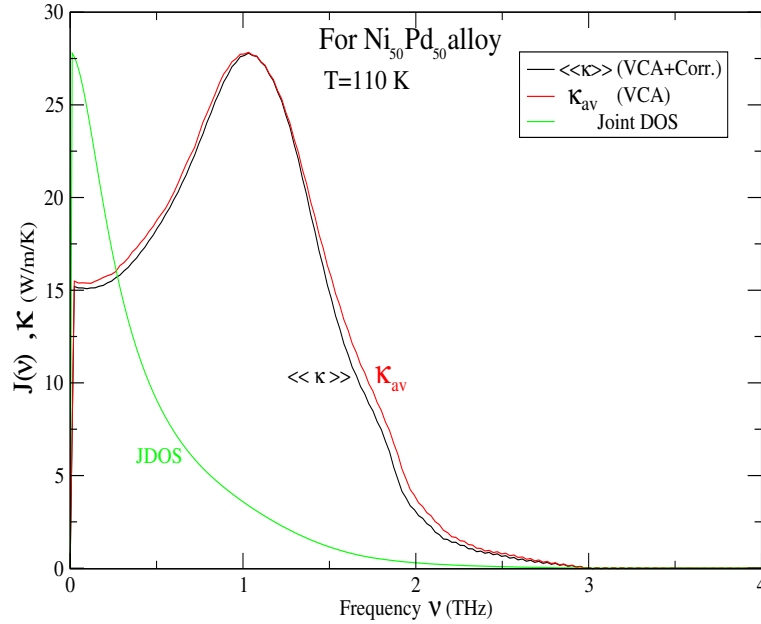


Figure 6.12: Configuration averaged lattice thermal conductivity vs phonon frequency ν (THz) for $\text{Ni}_{50}\text{Pd}_{50}$ disordered alloy. The red line and black line shows the conductivity using the average VCA current and effective current (consisting of average VCA current + disorder corrections + vertex correction) respectively. The green line in indicates the configuration averaged joint density of states.

where $J(\nu)$ is the joint density of states given by

$$J(\nu) = \int d\nu' \int \frac{d^3\mathbf{k}}{8\pi^3} \text{Tr} \left[\Im m \ll \mathbf{G}(\mathbf{k}, \nu') \gg \Im m \ll \mathbf{G}(\mathbf{k}, \nu' + \nu) \gg \right] \quad (6.27)$$

Figure (6.12) shows that the effect of disorder corrections to the current terms on the overall shape of lattice conductivity is rather small. We should note that the effect of disorder corrections to current and the vertex corrections in these alloys become negligible beyond phonon frequencies $\simeq 2.5$ THz. For the higher frequency modes the effect of scattering phenomenon is well described by the mean field approximation. It is in the low frequency region that configuration fluctuation effects beyond the mean-field becomes significant.

There is a very important feature in Fig. (6.12) that still needs discussion : which is how to explain the origin of a dip in $\kappa(\nu)$ at the lowest energy $\nu = 0$? A similar kind of dip has also been reported by Feldman *et al* 1993 while studying amorphous

Si and $\text{Si}_{1-x}\text{Ge}_x$ alloys. Their $\kappa(\nu)$ have a small Lorentzian shaped dip centered at $\nu=0$. This reflects the missing intra-band conductivity κ^H . This dip in $\kappa(\nu)$ stands at a small but finite value ($\nu \simeq 0$). The finiteness of the dip in $\kappa(\nu)$ is because of the fact that their calculation was based on a Kubo-Greenwood expression for the thermal conductivity with the delta functions in the expression broadened into a Lorentzian of small (but finite) width η . However in our case it is evident from the Fig. (6.12) that this dip in $\kappa(\nu)$ stands at $\kappa(\nu) \rightarrow 0$ at $\nu = 0$. This is due to the simple reason that in our calculation the Lorentzian broadening has not been put in by hand, but it arises automatically from the disorder effect on the crystalline spectral function $\Im m[\mathbf{G}(\mathbf{k}, \nu)]$. Another reason for this difference in the position of dip in $\kappa(\nu)$ may be due to the fact that Feldman *et.al.* carried out their calculation at a fixed wave-vector \mathbf{k} , while we have summed over the entire Brillouin zone.

The origin of this dip can also be explained by looking at the joint density of states (JDOS) represented by green line in Fig. (6.12). This quantity has a dip near $\nu = 0$ reminiscent of the dip in the $\kappa(\nu)$ curves. This indicates that a smooth convolution of two Green matrices $\mathbf{G}(\mathbf{k}, \nu')$ and $\mathbf{G}(\mathbf{k}, \nu' + \nu)$ (or two smooth densities of states obtained after summing \mathbf{k} over the Brillouin zone), as appeared in the expression (6.5) is mainly responsible for such a sharp dip in the lattice conductivity at $\nu = 0$. As discussed by Feldman *et.al.*, this dip at $\nu = 0$ disappears as the system size $N \rightarrow \infty$. They have also suggested an appropriate method to eliminate this dip in a sensible manner, which allows us to extrapolate the $\kappa(\nu)$ curve from a value at $\nu > 0$ ($\nu \simeq 0$) to a value at $\nu=0$. This extrapolated value of $\kappa(\nu)$ at $\nu = 0$ is nothing but the d.c. value of the lattice thermal conductivity κ_0 . In an attempt to calculate (κ_0), we have obtained a value of 15.25 W/m/K for $\text{Ni}_{50}\text{Pd}_{50}$ alloy at T=110 K.

Direct comparison with the experimental data on these systems is difficult, because the experimental thermal conductivity also has a component arising out of the contribution from electrons. Figure. (6.13) shows the temperature dependence of lattice conductivity. The top panel shows our theoretical result for the $\text{Ni}_{99}\text{Pd}_{01}$ alloy at three different frequencies. The bottom panel shows the experimental data Farrell and Greig 1969 on the total (electronic and lattice) thermal conductivity of the same 99-01 NiPd alloy. Since the frequency is not mentioned in the experimental data, we assume that it must be for low frequencies. The best comparison then will be between the middle (black)

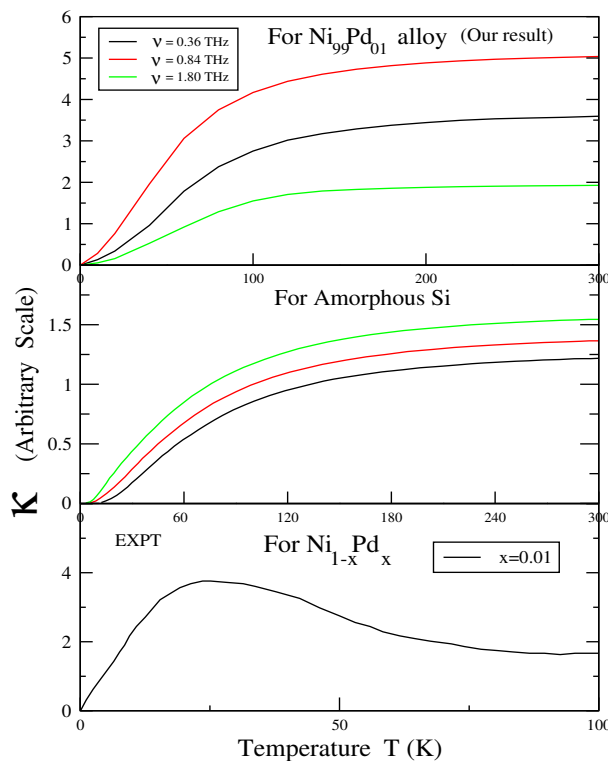


Figure 6.13: Thermal conductivity vs temperature $T(K)$ for NiPd alloys and Amorphous Si. The top panel shows our results on the lattice conductivity for $Ni_{99}Pd_{01}$ alloy at three different frequency cut-off ν . The middle panel shows the lattice conductivity for amorphous Si [Feldman *et al* 1993] at three different cut-off frequency, while the panel at the bottom shows the experimental data [Farrell and Greig 1969] for the total thermal conductivity (= lattice + electronic contribution) of the same $Ni_{99}Pd_{01}$ alloy.

curve on the top panel and that in the bottom one. The two agree qualitatively, except at low temperatures where we expect the electronic contribution to dominate. In order to understand whether the deviation *does arise* from the electronic contribution, we have compared the top panel with the thermal conductivity of amorphous-Si [Feldman *et al* 1993], shown in the middle panel. In a-Si the electrons near the Fermi level are localized and hence cannot carry any current. The contribution to thermal conductivity arises from scattering due to configuration fluctuations in the amorphous material. Qualitatively we expect the results to be similar to configuration fluctuation scattering in random alloys. Almost the entire contribution should come from the phonons. The behaviour of the two panels are quite similar. The origin of the hump in the experimental lattice conductivity

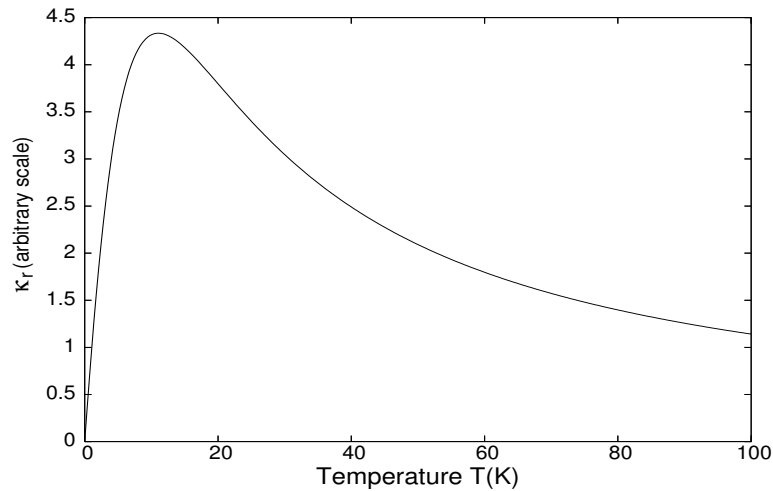


Figure 6.14: Residual or impurity contribution of the electronic part of the thermal conductivity

can also be understood if we assume Wiedemann-Franz law and write the residual part of the electronic contribution of the thermal resistivity as $\kappa_r = L_0 T / \rho_0(T)$. Here L_0 is the Lorenz number and $\rho_0(T)$ is the electrical resistivity. Assuming that the electrical resistivity behaves as $\rho_0(T) = A + BT + CT^2$ at low temperatures and with a suitable choice of the parameters, this contribution does show a hump followed by a decreasing behaviour flattening out at larger temperatures (see Fig 6.14). The sum of the contribution shown in the top panel of Fig. (6.13) and that in Fig. (6.14) would lead to the experimental behaviour shown in the bottom panel of Fig. (6.13). This is a plausibility argument and needs to be confirmed by a detailed calculation of the electronic contribution to the thermal conductivity. A careful inspection of our results (top panel of Fig. (6.13) indicates that at low temperatures where only low-energy vibrations are excited, $\kappa(T)$ is approximately a quadratic function of T . Figure. (6.15) shows a plot of κ vs T^2 in the low temperature regime. The calculated curve fits reasonably well with a straight line. This has been seen in experimental observations [Farrell and Greig 1969]. Additional scattering processes leading to a different temperature dependence of lattice conductivity become apparent at higher temperatures. At $T > 25$ K, $\kappa(T)$ rises smoothly to a T -independent saturated value. The dominant mechanism in this regime is the intrinsic harmonic diffusion of higher energy delocalized vibrations. These modes have not been well described by most previous theories. In Fig. (6.16), we display the frequency dependence of lattice

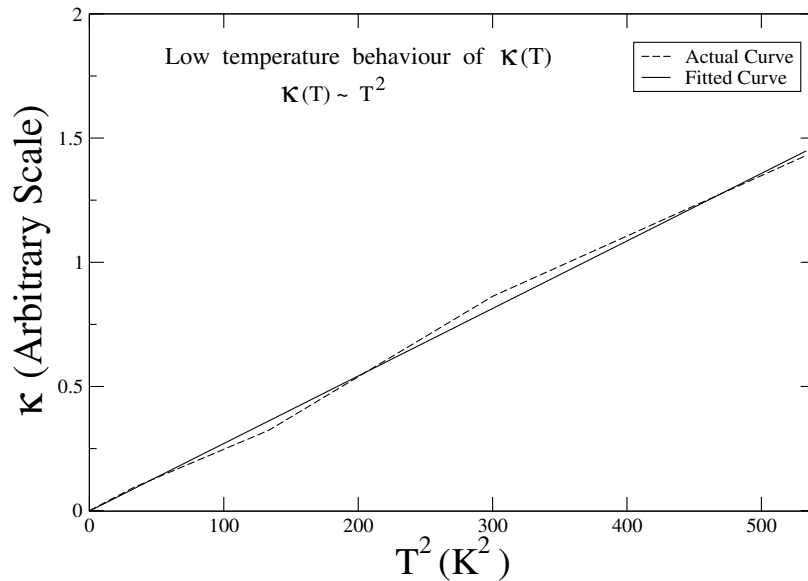


Figure 6.15: κ vs T^2 for low temperatures for 50-50 NiPd alloy

conductivity for $\text{Ni}_{50}\text{Pd}_{50}$ alloy at various temperatures. The figure clearly shows the saturation of lattice conductivity as we proceed toward the higher temperatures. The d.c. value of the conductivity (κ_0), which is just extrapolation of $\kappa(\nu)$ curve from a value at $\nu > 0$ to a value at $\nu = 0$, increases as we increase the temperature. Figure (6.17) shows the lattice conductivity as a function of frequency at $T=100$ K for various alloy compositions. From the figure, it is clear at a glance that the overall shape of frequency dependence of κ for various alloys of $\text{Ni}_{1-x}\text{Pd}_x$ looks similar except for $x=0.8$ and $x=0.9$, where extra structure appears in the frequency dependence. Similar behaviour has also been observed for $x=0.9$ in $\text{Ni}_{1-x}\text{Pt}_x$ alloy. We believe that this behaviour for $\text{Ni}_{1-x}\text{Pd}_x$ alloy at $x=0.8$ and 0.9 may be due to the strong disorder in masses, the effect of which becomes important in the two dilute limit alloys.

The thermal diffusivities $D(\nu)$ are important because the effect of disorder is often manifested in them more directly than in the conductivities. Not only that, thermal diffusivity also gives an approximate idea about the location of mobility edge as well as the fraction of delocalized states. In Fig. (6.18) we display the thermal diffusivity $D(\nu)$ vs frequency for various compositions. The extent of the phonon frequency spectrum is

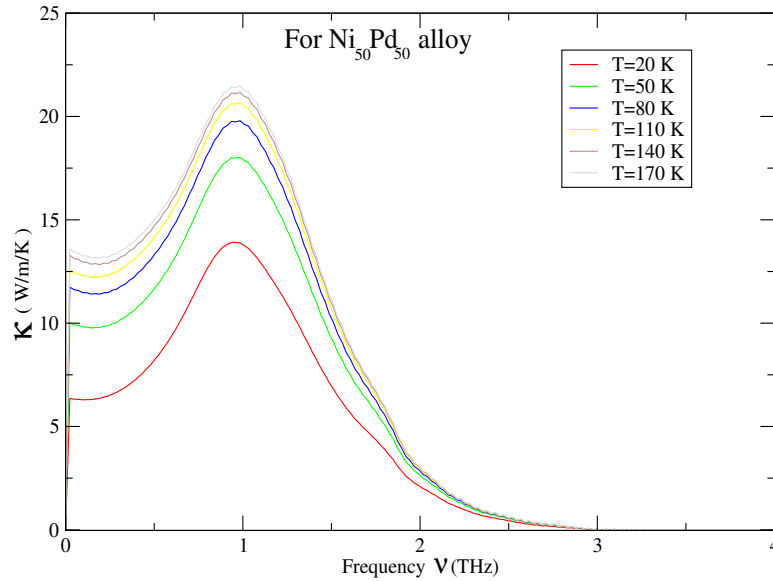


Figure 6.16: The configuration averaged lattice thermal conductivity vs phonon frequency ν (THz) at different temperatures T for $\text{Ni}_{50}\text{Pd}_{50}$ alloy.

shown by the broad lines. These have been obtained from the phonon density of states calculations. The density of states is non-zero across this spectrum range. The first thing to note is that, the region of large diffusivity in the five sets of alloys at the higher frequency side is not the same. In other words the weakly defined hump in the lower as well as higher frequency side are located at different positions for different alloys. The low frequency maximum in diffusivity is a minimum around the 50-50 composition where the disorder scattering is the maximum. Above 3 THz, there is a smooth decrease of diffusivity approximately linear in frequency $D(\nu) \propto (\nu_c - \nu)^\alpha$, with the critical exponent $\alpha \simeq 1$ and a critical frequency ν_c where $D(\nu)$ vanishes to within a very small level of noise. Figure (6.19) shows a plot of $D(\nu)$ vs $(\nu_c - \nu)^\alpha$ for $\text{Ni}_{50}\text{Pd}_{50}$. The allowed phonon states beyond this frequency must be due to localized phonon modes. The critical exponent $\alpha \simeq 1$ in our case agrees with scaling and other theories of Andersen localization [Lee and Ramakrishnan 1958]. The critical frequency ν_c locates the mobility edge above which the diffusivity is strictly zero in the infinite size limit. Once the mobility edge is located, the fraction of de-localized states may be obtained by evaluating the area under the $D(\nu)$

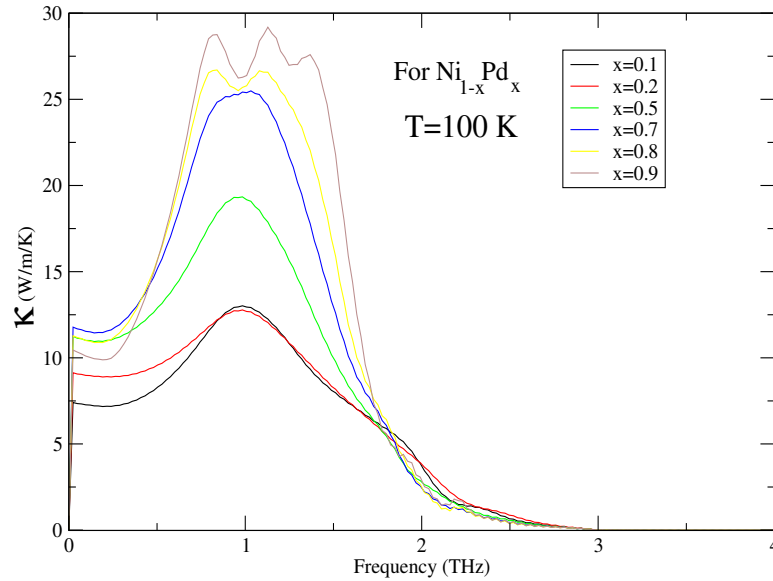


Figure 6.17: Frequency dependence of lattice thermal conductivity for various alloys $\text{Ni}_{1-x}\text{Pd}_x$ at $T=100$ K.

vs ν curve from $\nu = 0$ to $\nu = \nu_c$. It is clear from Fig. (6.18) that location of mobility edge varies with composition. Consequently the percentage of de-localized states available for thermal conduction in the system also varies with composition. An inspection of Fig. (6.18) determines the location of the mobility edges (ν_c) for the five different compositions. Figure (6.20) which shows the position of the mobility edge and the percentage of mobile phonon states in the spectrum as a function of the composition is quite illustrative. The maximum percentage of localized states occur at 50-50 composition where we expect disorder scattering to be a maximum. The mobility edge moves to higher frequencies as the concentration of Ni increases, but so does the band width of the phonon spectrum. The minimum percentage of mobile phonon states available for thermal conduction occurs, as expected, at around the 50-50 composition. A similar behaviour has also been discussed by Feldman *et al* 1993 while studying the effects of mass disorder on various $\text{Si}_{1-x}\text{Ge}_x$ alloys.

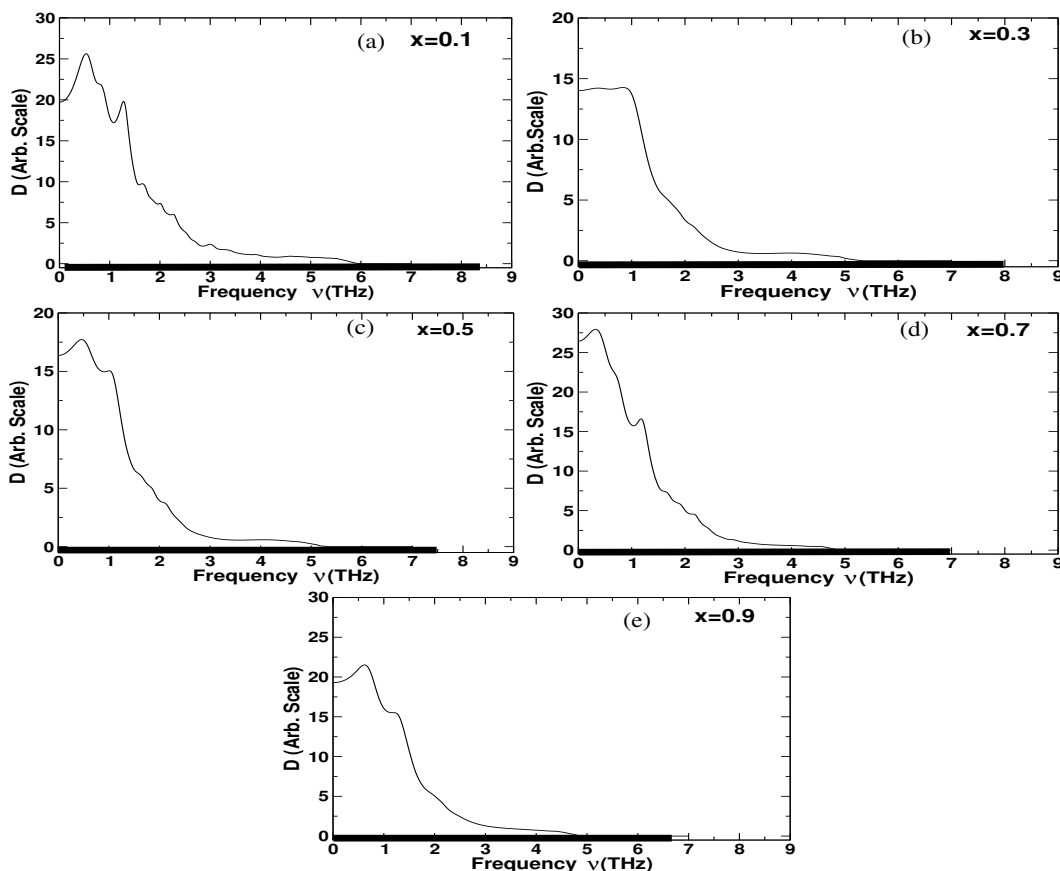


Figure 6.18: The configuration averaged thermal diffusivities $D(\nu)$ for $\text{Ni}_{1-x}\text{Pd}_x$ alloys. (a) $x=0.1$; (b) $x=0.3$; (c) $x=0.5$; (d) $x=0.7$; (e) $x=0.9$. The broad line on the frequency axis shows the extent of the vibrational spectrum.

6.6.2 NiPt alloy : Strong mass and force constant disorder.

It has been our experience [Alam and Mookerjee 2004, Alam and Mookerjee¹ 2005] that the effect of disorder in NiPt alloy is more dramatic than NiPd. For instance the appearance of sharp discontinuities observed in the dispersion where we have resonance states and consequent increase in the line-width [Alam and Mookerjee 2004].

Figure (6.21) shows the results for disordered $\text{Ni}_{50}\text{Pt}_{50}$ alloy. As before, the black curve represents the lattice conductivity including all kinds of disorder induced corrections while the red curve stands for the same quantity but using averaged heat currents and without vertex corrections. The green curve shows the scaled joint density of states. From the

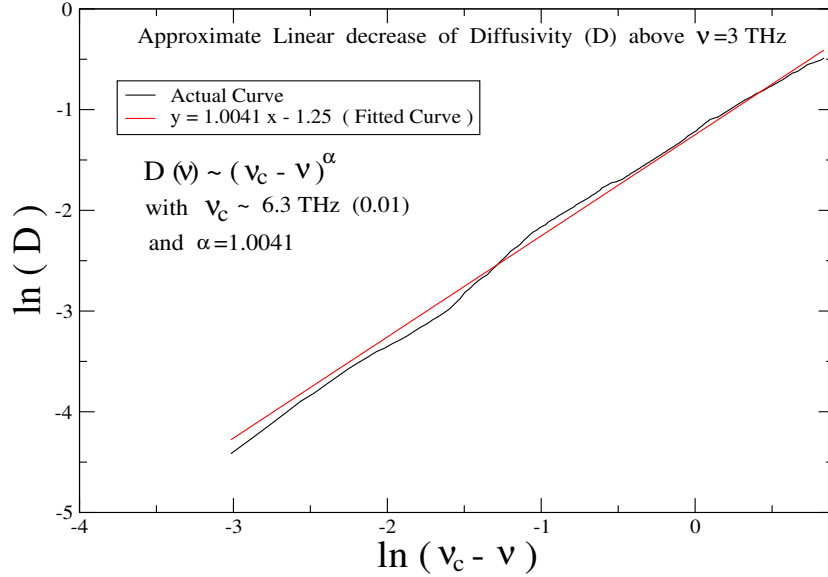


Figure 6.19: The behaviour of thermal diffusivity as a function of $(\nu_c - \nu)^\alpha$

figure it is clear that as in the case of NiPd, the transition rate ‘ τ ’ is strongly dependent both on the initial and the final energies throughout the phonon frequency (ν). Figure (6.21) also clarifies that although the effect of disorder corrections to the current terms is small, but this effect is comparatively more pronounced in $Ni_{50}Pt_{50}$ than in $Ni_{50}Pd_{50}$. The effect of disorder corrections to current and the vertex corrections in the present case become negligible beyond phonon frequencies $\simeq 2.4$ THz. In the low frequency region, configuration fluctuation effects beyond the mean-field is more pronounced in NiPt than in NiPd. This may be because of the two simple physical reasons : First, the NiPt is an alloy where both mass ($m_{Pt}/m_{Ni} \simeq 3$) as well as force constant (Pt-force constants are on an average 55% larger than those of Ni) disorder dominates, while in NiPd alloy the mass disorder ($m_{Pd}/m_{Ni} \simeq 1.812$) is weaker than NiPt and the force constants are almost the same for the two constituents. Second, from a purely phenomenological point of view, there is a larger size mismatch between Ni and Pt in NiPt alloy as compared to Ni and Pd in NiPd alloy.

The temperature dependence of lattice conductivity for $Ni_{50}Pt_{50}$ alloy at various cut-off frequencies are shown in Fig. (6.22). The conductivity increases initially (in the low

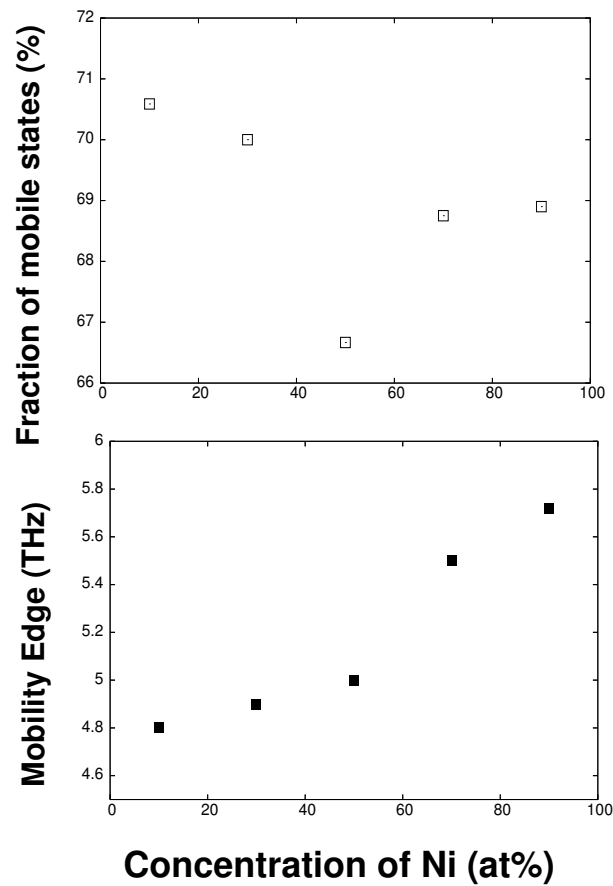


Figure 6.20: The position of the mobility edge (bottom) and the percentage of mobile phonon states (top) as a function of the alloy composition for NiPd alloy.

T-regime) as an approximate quadratic function of temperature and ultimately increases smoothly to a T-independent saturated value. As far as such dependence of $\kappa(T)$ in the high temperature regime is concerned, the heat in this conduction channel is carried by non-propagating modes which are strongly influenced by the disorder but mostly not localized and therefore able to conduct by intrinsic harmonic diffusion. This is a smooth dependence which closely resembles the specific heat and saturates like the specific heat at high temperatures. Following Slack 1979 we could call this piece the “*minimum thermal conductivity*”. A number of authors have discussed that low temperature dependence of $\kappa(T)$ shows a mild plateau like region. In this regime the heat is mainly carried by the propagating long wavelength acoustic modes. The complex inelastic scattering processes

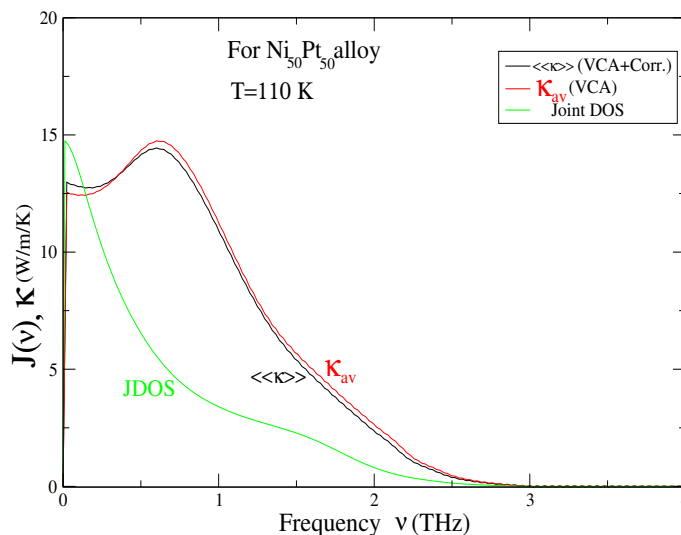


Figure 6.21: Same as Fig. (6.12) but for $\text{Ni}_{50}\text{Pt}_{50}$ disordered alloy.

then kill off the low frequency contribution at higher temperatures leaving a peak which becomes the plateau. However there are situations, where the propagating modes become reasonably well damped (as in our calculation) and are no longer able to carry much heat. In such cases the contribution of delocalized and poorly conducting vibrations takes over, giving a net result in good accord with the Kittel's old idea. Under these circumstances the plateau like region in the low temperature regime almost disappears. The damping of propagating modes is also amplified as we make the alloy more and more concentrated. This can easily be verified by looking at the results of Farrell and Greig 1969, which shows that as we increase the concentration, the plateau like region goes down and gets smoother.

The concentration dependence of lattice conductivity at a fixed phonon frequency $\nu = 1.05 \text{ THz}$ are plotted in Fig. (6.23). The various curves in this figure stand for various values of the temperature T starting from a lower value of 50 K to a higher value of 230 K. It is clear from the figure that the concentration dependence is almost symmetric about $x=0.5$. It has been discussed by Flicker and Leath 1973 within the framework of coherent potential approximation that this asymmetry is a function of the size of the sample chosen i.e. a large N leads to less asymmetry. They have verified this

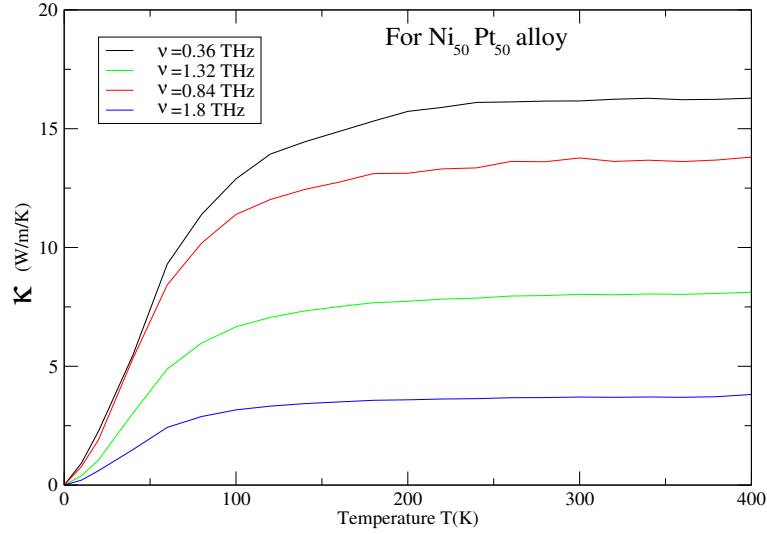


Figure 6.22: The averaged lattice thermal conductivity vs temperature $T(K)$ at various cut-off frequency ν_{cutoff} for $Ni_{50}Pt_{50}$ alloy.

statement by performing two calculations one for $N=100$ and other for $N=2000$. The concentration dependence in the later case is more symmetric as compared to the former ones. In our case, the results shown in Fig. (6.23) are the optimal symmetric structure for the concentration dependence of κ . This is because our calculations are performed in the reciprocal space representation which involves the entire lattice.

An interesting challenge remaining in this problem is to calculate the effect of adding anharmonicity to the model. The reason why one should be interested in calculating the anharmonicity effect is because in real systems at high temperature phonon-phonon Umklapp scattering becomes the dominant scattering mechanism. This Umklapp scattering actually arises due to the presence of anharmonic terms in the Hamiltonian. The effect of this anharmonicity is to flatten the lattice conductivity vs concentration curve.

Fig. (6.24) shows the frequency dependence of diffusivity $D(\nu)$ for various alloy compositions. The thick lines on the frequency axes shows the extent of the frequency spectrum. It is clear from Fig. (6.24) that there are basically two regions of large thermal diffusivity : one near the lower frequency region ($\simeq 0.5 THz$) and the other around a somewhat higher frequency region ($\simeq 1.25 THz$). But as we go on increasing the Pt-concentration,

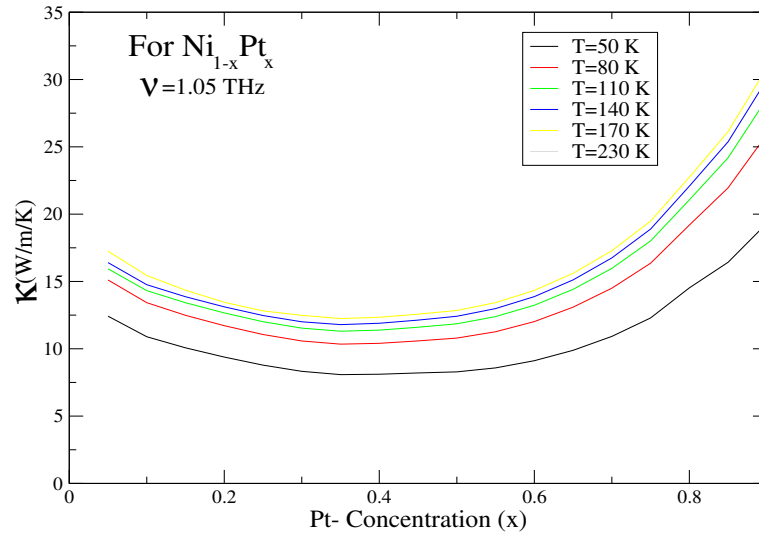


Figure 6.23: Lattice thermal conductivity vs Pt-concentration for various temperature T at phonon frequency $\nu = 1.05 THz$.

the former region of large diffusivity starts decreasing gradually and becomes almost flat for the maximum Pt-concentration of 90%. The latter region of large diffusivity sits on a portion of the frequency spectrum above the transverse acoustic vibrations. Here the modes have large velocities and are probably very effective carriers of heat. The approximate linear decrease in diffusivity starts at about 3 THz. But the location of mobility edge in this case varies with composition in a slightly different way as compared to the case of NiPd alloy. Fig. (6.25) (bottom) shows the position of the mobility edge ν_c as a function of the alloy composition. As the concentration of heavy Pt increases, the band width of the frequency spectrum (which is proportional to the square root of the mass) shrinks and the position of the mobility edge within the band also shrinks. Fig. (6.25) (top) shows the fraction of the frequency band which is extended. When the disorder is the strongest, i.e. at 50-50 composition, this fraction is a minimum.

One thing is very clear from the above discussion that, in an alloy where mass disorder dominates and the force constant disorder is weak (as in the case of NiPd alloy), the complex disorder scattering processes try to localize more vibrational modes as compared to those in an alloy where both mass as well as the force constant disorder dominates

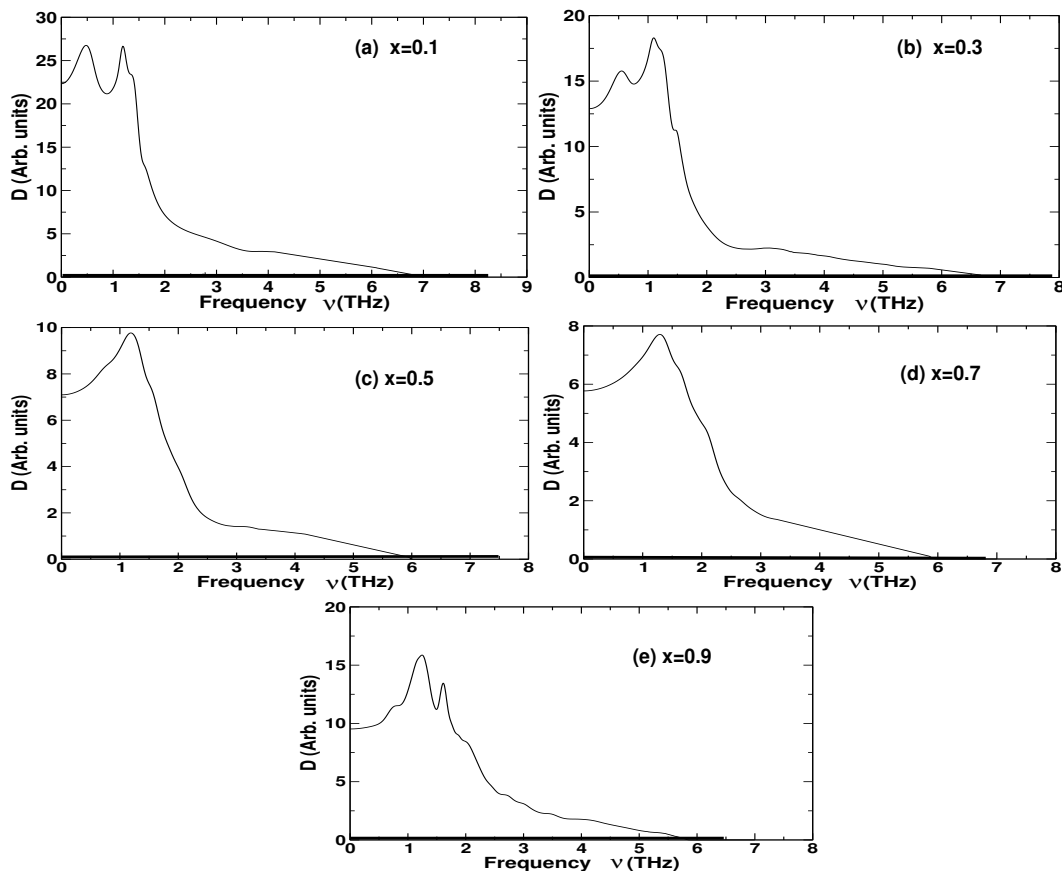


Figure 6.24: Same as Fig. (6.18) but for $\text{Ni}_{50}\text{Pt}_{50}$ alloy.

(as in the case of NiPt alloy). The result can be interpreted in a slightly different way as : “*the role of force constant disorder in binary alloys is to make the vibrational eigenstates more delocalized*” , i.e. the more dominant the force constant disorder is, the more delocalized the vibrational modes will be.

6.7 Conclusion

We have formulated a theory for the calculation of configuration averaged lattice thermal conductivity and thermal diffusivity based on a realistic model. The augmented space block recursion allows us to include, in the calculation of our averaged propagators, effects of joint fluctuations at more than one site. The scattering diagram approach proves to be useful in analyzing and calculating the disorder corrections to the averaged current.

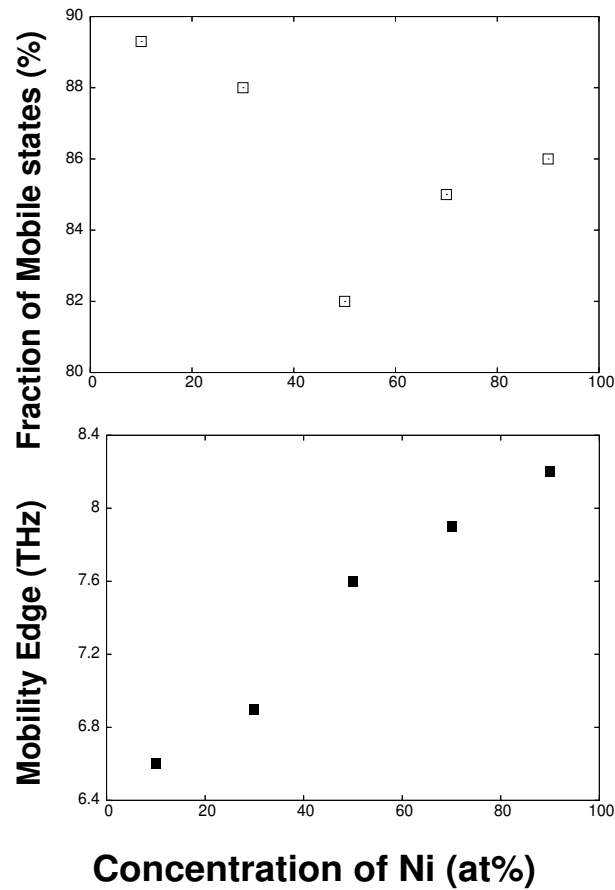


Figure 6.25: Same as Fig. (6.20) but for $\text{Ni}_{50}\text{Pt}_{50}$ alloy.

These are shown to be the dominant corrections and are related to the self energy. Next in importance, we have studied the effect of vertex corrections arising out of the correlated propagation. We have shown explicitly how to obtain these corrections within the ladder diagram approximation. We have demonstrated through our numerical results that how this multiple scattering based formalism captures the effect of off-diagonal and environmental disorder present in the problem. A significant contribution of this particular work beyond the earlier theoretical approaches is the inclusion of force constant fluctuations properly in the theory. Our efficient Brillouin zone integration codes for disordered alloys makes the numerical calculation stable and accurate. We have already shown in the previous chapter that the approximation involving termination of the matrix continued fraction expansion of the green matrix retains the essential Herglotz analytic properties of

the diagonal green function. We have applied the formalism to two realistic disordered alloys ; namely NiPd and NiPt. We have shown that the effect of disorder corrections to the current and the vertex correction on the overall shape of lattice thermal conductivity for both the alloys are very small. Comparatively the effect is found to be more pronounced in NiPt alloy, which is due to the presence of strong disorder both in masses and force constants in this alloy. The saturation of lattice conductivity at higher temperatures has been shown for both the alloys. The numerical results on the harmonic diffusivity provide an interesting idea about the localization and delocalization of the vibrational eigenstates. It says that in disordered binary alloys “ the more stronger the force constant disorder is, the more delocalized the vibrational modes will be” . That is why NiPt alloy has larger fraction of delocalized states as compared to that in NiPd alloy.

Chapter 7

An assessment of the work and future plans

7.1 Concluding Remarks

In this chapter, we shall assess our work: that is, specify our initial plan of work, assess how much we have achieved and finally lay out our future plans.

Our aim was to systematically develop a theoretical scheme to study vibrational properties of disordered alloys based on a recursion method. This includes the phonon dispersion relation, disorder induced line widths, inelastic neutron scattering cross section, lattice thermal conductivity and thermal diffusivity. The configuration averaging is done using the augmented space method combined with a generalized scattering diagram technique. In the following, we shall briefly describe the steps we followed to reach our goal.

In chapter 1 we have presented an overview of the lattice dynamics calculation for a 3D realistic system. We have then defined the basic quantities of interest like phonon density of states, coherent structure factors, phonon line-widths, inelastic neutron scattering cross sections and thermal conductivity. we have also given a brief description of the recursion method as well as a generalized version of this, called *Block Recursion Method*, which calculate the entire Green matrix and self-energy matrix.

In chapter 2, we have described the augmented space recursion method for configuration averaging in disordered systems. Because of the presence of off-diagonal disorder in the phonon problem, it becomes very difficult to include the effects of extended environment. We would like to mention that, the recursion calculations can be carried out much faster and for many more recursive steps exactly, if it is performed on a subspace of the

original augmented space reduced by using the symmetries of both the underlying lattice and random configurations on the lattice.

In chapter 3, we have derived the augmented space recursion formulation for phonons in disordered alloys in the reciprocal space representation. In this formulation the real space part was taken into account exactly and there was no truncation of this in the recursion. We have investigated the phonon dispersion, disorder induced line-widths etc. in three different alloy systems, the choice of which is not arbitrary. The comparison of our results with experiments and other recent theories comes out to be quite satisfactory.

For the entire numerical studies in the previous chapter, however, we had no prior information about the species dependence of the force constants but rather choose a set of force constants empirically. A better understanding of the role of disorder in the vibrational properties of random alloys could be achieved with prior information about the force constants, which could be obtained from more microscopic theories. In chapter 4 we have rectified this and make use of a first principles calculation (i.e. the *Density Functional Perturbation Theory*) for phonons to obtain the dynamical matrices themselves from this calculation. Further calculations are performed using these first principles parameters.

Chapter 5 has been devoted for the study of inelastic neutron scattering in random binary alloys. A multiple scattering diagram approach has been combined with augmented space representation to separate the coherent and incoherent part of the total inelastic scattering cross section. Since we require the off diagonal elements of the Green matrix for the calculation of cross section, we have generalized the ordinary recursion to a block recursion technique. The termination procedure used by us is rather brute force. In the termination process we have repeatedly invert a 3×2 (3-modes) matrix for 10^3 times, which may carry inaccuracies in the calculation. Using a better termination scheme will improve the accuracy of the calculation. This we may think over in nearest future.

It has been known that the thermal conductivity expression based on traditional reciprocal space, that is, based on Bloch's theorem, is unsuitable for disordered systems as they do not enjoy potential periodicity. So in chapter 6, we have obtained an alternate expression where the quantum states are directly labeled by energy and frequency rather than by modes and crystal momentum indices. We have proposed a modified expression for the lattice thermal conductivity as a convolution of a frequency-temperature depen-

dent transition matrix and energy resolved JDOS. We have then presented a formulation for the configuration averaged lattice thermal conductivity in random alloys. The disorder scattering renormalizes the averaged current to an effective current and the average VCA to a configuration averaged propagator beyond the CPA approximation. We have also calculated the configuration averaged thermal diffusivity within the harmonic approximation. Finally we have set up a computationally feasible program and applied it to NiPd and NiPt alloys. We have reported a quadratic temperature dependence of thermal conductivity in the low temperature regime which is similar to the findings of previous theories and experiment. The frequency dependence of lattice thermal conductivity for $x > 0.7$, in both the alloys $\text{Ni}_{1-x}\text{Pd}_x$ and $\text{Ni}_{1-x}\text{Pt}_x$, looks quite unusual, which is due to the strong disorder in masses. The thermal diffusivity gives an idea about the location of mobility edge as well as the fraction of localized and de-localized states. A comparative study of two alloys (NiPd and NiPt) predicted a very important result that “ the role of force constant disorder in binary alloys is to make the vibrational eigenstates more delocalized ”

7.2 Future directions

As far as the thermal conductivity calculation is concerned, so far we have presented a formulation which calculates only the lattice contribution to the thermal conductivity. For comparison with experiment we have assumed the validity of thermal analogue of Matthiessen’s rule, and calculate the electronic contribution to thermal conductivity using the Wiedemann-Franz law. We have then summed up the two contributions to finally compare our results with the experiment. This is however a plausibility argument and need to be confirmed by a detailed calculation of the electronic contribution to the thermal conductivity. We shall be taking this as one of our future project and derive a formulation for the calculation of the electronic contribution to thermal conductivity for disordered binary alloys.

Another future direction is to repeat the entire calculation of this thesis for systems with more than one atom per unit cell. The basic idea is to look at the effects of optical modes on the properties studied presently. The augmented space recursion is ideally

suitable for such a study. The electronic problem in systems with more than one atom per unit cell has already been developed by our group.

The investigation of the nature of electron-phonon interaction in disordered alloys is another area of interest which can be thought of in future.

We also have a plan to study the behaviour of phonon excitations in random ternary alloys.

A PhD. programme is always time bound and a person's thirst for knowledge may not find its fulfillment in this limited span of time. But this endeavor may be considered as a training ground for research and it does elevate his thirst for more. I cannot assess how much knowledge of disorder physics I have been able to pick up, but I sincerely believe that this work with all its limitations will encourage me to go on working in this vastly exciting area of materials studies.

1. Operations in augmented reciprocal space

The main operations of the effective dynamical matrix on a general state $|\mathbf{k} \otimes \{\mathcal{C}\}\rangle = ||\{\mathcal{C}\}\rangle$ in the augmented reciprocal space are given below, where $\{\mathcal{C}\} = \{R_1, R_2, \dots, R_c\}$ indicates the cardinality sequence with $|\downarrow\rangle$ configuration at R_1, R_2, \dots, R_c sites. This is required to implement the recursion procedure :

$$\begin{aligned} \left(\sum_R \mathbf{p}_R^\downarrow \otimes \mathbf{P}_R \right) ||\{\mathcal{C}\}\rangle &= \left(\sum_R \mathbf{p}_R^\downarrow \otimes \mathbf{P}_R \right) \frac{1}{\sqrt{N}} \sum_{R'} \exp(i\mathbf{k} \cdot R') |R', \{\mathcal{C}\}\rangle \\ &= ||\{\mathcal{C}\}\rangle \delta(R_0 \in \{\mathcal{C}\}) \quad (R_0 \text{ is any reference site}) \\ \left(\sum_R \mathbf{T}_R^{\uparrow\downarrow} \otimes \mathbf{P}_R \right) ||\{\mathcal{C}\}\rangle &= ||\{\mathcal{C} \pm R_0\}\rangle \\ \left(\sum_R \sum_\chi \mathbf{I} \otimes \mathbf{T}_{R, R+\chi} \right) ||\{\mathcal{C}\}\rangle &= \left(\sum_R \sum_\chi \mathbf{I} \otimes \mathbf{T}_{R, R+\chi} \right) \frac{1}{\sqrt{N}} \sum_{R'} \exp(i\mathbf{k} \cdot R') |R', \{\mathcal{C}\}\rangle \\ &= s(\mathbf{k}) ||\{\mathcal{C} - \chi\}\rangle \quad (\chi \text{ is a lattice vector}) \end{aligned}$$

where, $s(\mathbf{k}) = \sum_\chi \exp(-i\mathbf{k} \cdot \chi)$

$$\begin{aligned} \left(\sum_R \sum_\chi (\mathbf{p}_R^\downarrow + \mathbf{p}_{R+\chi}^\downarrow) \otimes \mathbf{T}_{R, R+\chi} \right) ||\{\mathcal{C}\}\rangle &= s(\mathbf{k}) ||\{\mathcal{C} - \chi\}\rangle \left[\delta(R_0 \in \{\mathcal{C} - \chi\}) \right. \\ &\quad \left. + \delta(R_0 + \chi \in \{\mathcal{C} - \chi\}) \right] \\ \left(\sum_R \sum_\chi (\mathbf{T}_R^{\uparrow\downarrow} + \mathbf{T}_{R+\chi}^{\uparrow\downarrow}) \otimes \mathbf{T}_{R, R+\chi} \right) ||\{\mathcal{C}\}\rangle &= s(\mathbf{k}) \left[||\{\mathcal{C} - \chi\} \pm R_0\right. \\ &\quad \left. + ||\{\mathcal{C} - \chi\} \pm (R_0 + \chi)\right] \\ \left(\sum_R \sum_\chi (\mathbf{p}_R^\downarrow \mathbf{p}_{R+\chi}^\downarrow) \otimes \mathbf{T}_{R, R+\chi} \right) ||\{\mathcal{C}\}\rangle &= s(\mathbf{k}) ||\{\mathcal{C} - \chi\}\rangle \left[\delta(R_0 \in \{\mathcal{C} - \chi\}) \right. \\ &\quad \left. \delta(R_0 + \chi \in \{\mathcal{C} - \chi\}) \right] \\ \left(\sum_R \sum_\chi (\mathbf{T}_R^{\uparrow\downarrow} \mathbf{T}_{R+\chi}^{\uparrow\downarrow}) \otimes \mathbf{T}_{R, R+\chi} \right) ||\{\mathcal{C}\}\rangle &= s(\mathbf{k}) \left[||\{\mathcal{C} - \chi\} \pm R_0 \pm (R_0 + \chi)\right] \\ \left(\sum_R \sum_\chi (\mathbf{p}_{R+\chi}^\downarrow \mathbf{T}_R^{\uparrow\downarrow} + \mathbf{p}_R^\downarrow \mathbf{T}_{R+\chi}^{\uparrow\downarrow}) \otimes \mathbf{T}_{R, R+\chi} \right) ||\{\mathcal{C}\}\rangle &= s(\mathbf{k}) \left[||\{\mathcal{C} - \chi\} \pm R_0\right. \\ &\quad \delta((R_0 + \chi) \in \{\mathcal{C} - \chi\}) + \\ &\quad ||\{\mathcal{C} - \chi\} \pm (R_0 + \chi)\rangle \\ &\quad \left. \delta(R_0 \in \{\mathcal{C} - \chi\}) \right] \end{aligned} \quad (.1)$$

We note that all operations involve only manipulations of the configuration part of the state [Biswas *et al* 1995] (i.e. manipulations of the cardinality sequence only). The operation of the effective dynamical matrix thus entirely takes place in the configuration space and the calculation does not involve the real space \mathcal{H} at all. This is an enormous simplification over the standard augmented space recursion described earlier Saha *et al* 1994, where the entire reduced real space part as well as the configuration part was involved in the recursion process. Since one can efficiently store the configurations in bits of words so now the calculation becomes much simpler. These operations finally involve simple bit manipulation routines.

It is interesting to note that the second operation in the above list creates a new configuration. In the next step of recursion the third operation translates the entire operation by lattice translations $\{\chi\}$. The cluster of configurations thus ‘travel’ across the lattice as recursion proceeds.

Bibliography

- Aiyer P N, Elliott R J, Krummhansl J A and Leath P L *Phys. Rev.* **181** 1006 (1969).
- Alam A and Mookerjee A *Phys. Rev.* **B 69** 024205 (2004).
- Alam A and Mookerjee¹ A *Phys. Rev.* **B 71** 094210 (2005).
- Allen P B and Feldman J L *Phys. Rev.* **B 48** 12581 (1993).
- Baroni S, Gironcoli S De and Dal Corso A *Rev. Mod. Phys.* **73** 515 (2001).
- Bauers E, Gratz E, Hutflesz G, and Muller H *J. Phys. Condens Matter* **3** 7641 (1991).
- Beer N and Pettifor D G *Electronic Structure of Complex Systems* ed. Phariseau P and Temmerman W M (Plenum, New York, 1984) p 769.
- Biava D A, Ghosh S, Johnson D D, Shelton W A and Smirnov A *Phys. Rev.* **B 72** 113105 (2005).
- Biswas P, Sanyal B, Fakhruddin M, Halder A, Mookerjee A, Ahmed M *J. Phys. Condens Matter* **7** 8569 (1995).
- Bosi P, Dupre F, Menzinger F, Sacchetti F and Spinelli M C *Nuovo Cim. Lett.* **21** 436 (1978a) ; *Nuovo Cim.* **46** 337 (1978b).
- Brouers F *Solid State Commun.* **10** 757 (1972).
- Brouers F and Van der Rest J *J. Phys. F: Metal Phys* **2** 1070 (1972).
- Brouers F, Ducastelle F, Gautier F and Van der Rest J *J. Phys. F: Metal Phys* **3** 2120 (1973).
- Dasgupta I, Saha T and Mookerjee A *J. Phys. Condens Matter* **8** 1979 (1996).
- Dutton D H, Brockhouse B N and Miller A P *Can. J. Phys.* **50** 2915 (1972).

Edwards S F *Phil. Mag.* **3** 1020 (1958).

Elliot R J, Krumhansl J A and Leath P L *Rev. Mod. Phys.* **46** 465 (1974).

Elliot R J and Taylor D W *Proc. Phys. Soc. Lond.* **83** 189 (1964) ; *Proc. Roy. Soc. Lond.*
A 296 161 (1967)

Farrell T and Greig D *J. Phys. C : Solid State Phys* **2** 1465 (1969).

Feldman J L, Kluge M D, Allen P B and Wooten F *Phys. Rev.* **B 48** 12589 (1993).

Flicker J K and Leath P L *Phys. Rev.* **B 7** 2296(1973).

Foo E-ni, Amar A and Ausloos M *Phys. Rev.* **B 4** 3350 (1971).

Garber M, Scott B W, and Blatt F J *Phys. Rev.* **130** 2188 (1963); Lindenfeld P and
Pennebaker W B *Phys. Rev.* **127** 1881 (1962).

Ghosh S, Das N and Mookerjee A *J. Phys. Condens Matter* **9** 10701 (1997).

Ghosh S, Das N and Mookerjee A *Int. J. Mod. Phys.* **B 21** 723 (1999).

Ghosh S, Leath P L, and Cohen Morel H *Phys. Rev.* **B 66** 214206 (2002).

Ghosh S, Neaton J B, Antons A H, Cohen M H and Leath P L *Phys. Rev.* **B 70** 024206
(2004)

Godin T J and Haydock R *Phys. Rev.* **B 38** 5237 (1988).

Godin T J and Haydock R *Phys. Rev.* **B 46** 1528 (1992).

Gonis A and Garland J W *Phys. Rev.* **B 18** 3999 (1978).

Grunewald G *J. Phys. F: Met. Phys.* **6** 999 (1976).

Hardy R J *Phys. Rev.* **132** 168 (1963).

Haydock R, Heine V and Kelly M J *J. Phys. C : Solid State Phys* **5** 2845 (1972).

Haydock R *Solid State Phys.* (Academic Press, New York) **35** 216 (1980).

Heine V in *Solid State Physics Vol. 35* edited by Ehrenreich H, Seitz F, and Turnbull D
(Academic, NewYork) (1980).

Jarrell M and Krishnamurthy H R *Phys. Rev.* **B 63** 125102 (2001).

Kamitakahara W A and Brockhouse B.N *Phys. Rev.* **B 10** 1200 (1974).

Kamitakahara W A and Taylor D W *Phys. Rev.* **B 10** 1190 (1974).

Kaplan T and Gray L J *Phys. Rev.* **B 14** 3462 (1976) ; *Phys. Rev.* **B 24** 1872 (1981).

Kaplan T, Leath P L, Gray L J and Diehl H W *Phys. Rev.* **B 10** 1200 (1980).

Kaplan T and Mostoller M *Phys. Rev.* **B 9** 353 (1974).

Kumar V, Mookerjee A and Srivastava V K *J. Phys. C : Solid State Phys* **15** 1939 (1982).

Langer J S *Phys. Rev.* **120** 714 (1960) ; *J. Math. Phys.* **2** 584 (1961).

Leath P L *Phys. Rev.* **171** 725 (1968).

Leath P L *Phys. Rev.* **B 2** 3078 (1970).

Lee P A and Ramakrishnan T V, *Rev. Mod. Phys.* **57** 287 (1985).

Leibfried G and Breuer N *Points Defects in Metals I* (Springer Tracts in Modern Physics, Vol. 81, Springer – Verlag Berlin, New York).

Louie S G, Froyen S and Cohen M L *Phys. Rev.* **B 26** 1738 (1982).

Lovesey S W and Marshal W *Theory of thermal neutron scattering* (Oxford University press, London) (1971).

Luchini M U and Nex C M M *J. Phys. C : Solid State Phys* **20** 3125 (1987).

Maradudin A A, Montrol E W, Weiss G H, Ipatova I P *Theory of lattice dynamics in the harmonic approximation (Solid State Physics Suppl. 3, Academic press, New York and London)*(1971).

Mehaddene T, Kentzinger E, Hennion B, Tanaka K, Numakura H, Marty A, Parasote V, Cadville M C, Zemirli M and Pierron-Bohnes V *Phys. Rev.* **B 69** 024304 (2004).

Methfessel M and Paxton T A *Phys. Rev.* **B 40** 3616 (1989).

Mills R and Ratanavaraksa R *Phys. Rev.* **B 18** 5291 (1978).

Mookerjee A *J. Phys. C : Solid State Phys* **6** L205 (1973).

Mookerjee A *J. Phys. C : Solid State Phys* **6** 1340 (1973).

Mookerjee A *J. Phys. C : Solid State Phys* **8** 1524 (1975).

Mookerjee A *J. Phys. C : Solid State Phys* **9** 1225 (1976).

- Mookerjee A, *Electronic Structure of Alloys, Surfaces and Clusters* (ed. Sarma D D and Mookerjee A) (Taylor Francis, London) (2003).
- Mookerjee A and Prasad R *Phys. Rev. B* **48** 17724 (1993).
- Mookerjee A and Singh R P *J. Phys. C : Solid State Phys* **18** 4261 (1985).
- Mookerjee A and Singh R P *J. Phys. F: Met. Phys.* **18** 2171 (1988).
- Mookerjee A, Srivastava V K and Choudhry V *J. Phys. C : Solid State Phys* **16** 4555 (1983).
- Mookerjee A and Yussouff M *Phys. Rev. B* **33** 5414 (1986).
- Nickel B G and Krummhanl J A *Phys. Rev. B* **4** 4354 (1971).
- Nicklow R M in *Methods of Experimental Physics*(Academic Press, 1983) Vol 23 p. 172.
- Nicklow R M, Vijayaraghavan P R, Smith H G and Wilkinson M K *Phys. Rev. Lett.* **20** 1245 (1968) ; Lynn J W, Smith H G and Nicklow R M *Phys. Rev. B* **8** 3493(1973) ; Mozer B, Otnes K and Myers V M *Phys. Rev. Lett.* **8** 278(1962).
- Nowak E and Dederichs P H *Phys. Rev. B* **25** 875 (1982).
- Paudyal D, Saha-Dasgupta T and Mookerjee A *J. Phys. Condens Matter* **16** 2317 (2004).
- Perdew J P and Zunger A *Phys. Rev. B* **23** 5048 (1981).
- Rowlands D A, Satunton J B, Gyorffy B L, Bruno E and Ginatempo B *Phys. Rev. B* **72** 045101 (2005).
- Saha K K and Mookerjee A *Cond-Mat/0405175* (2004) ; Biswas P, Sanyal B, Fakhruddin M, Halder A, Mookerjee A and Ahmed M *J. Phys. Condens Matter* **7** 8569 (1995) ; Biswas P, Sanyal B, Mookerjee A, Huda A, Chowdhury N, Ahmed M and Halder A *Int. J. Mod. Phys. B* **11** 3703 (1997).
- Saha K K and Mookerjee A *Phys. Rev. B* **70** 134205 (2004).
- Saha K K, Mookerjee A and Jepsen O *Phys. Rev. B* **71** 094207 (2005).
- Saha K K, Saha-Dasgupta T, Mookerjee A, Dasgupta I *J. Phys. Condens Matter* **16** 1409 (2004).
- Saha T, Dasgupta I and Mookerjee A *Phys. Rev. B* **50** 13267 (1994).

- Saha T, Dasgupta I and Mookerjee A *J. Phys. Condens Matter* **6** L245 (1994).
- Schultz T D and Shapero D *Phys. Rev.* **181** 1062 (1973).
- Shiba H, *Prog. Theor. Phys.* **40** 942 (1968).
- Shiba W *Prog. Theo. Phys.* **46** 77 (1971).
- Singh R P, *PhD Thesis IIT Kanpur India* (1982).
- Sjölander A in “Phonons and phonon interactions” edited by T.A. Bak (Benjamin, New York)(1964).
- Slack G A in *Solid State Physics* edited by Ehrenreich H, Seitz F, and Turnbull D (Academic, New York, 1979) Vol. 34, p. 1.
- Smith H G and Wakabayashi N *Bull. Am. Soc.* **21** 410 (1976).
- Soven P *Phys. Rev.* **156** 809 (1967).
- Srivastava B N, Chatterjee S, Sen S K, and Chakraborty D K *J. Phys. C : Solid State Phys* **2** S169 (1970).
- Svensson E C and Brockhouse B N *Phys. Rev. Lett.* **18** 858 (1967) ; Wakabayashi N *Phys. Rev.* **B 8** 6015 (1973) ; Mozer B, Otnes K and Thaper C *Phys. Rev.* **152** 535(1966).
- Taylor D W *Phys. Rev.* **156** 1017 (1967).
- Tsunoda Y, Kunitomi N, Wakabayashi N, Nicklow R M and Smith H G *Phys. Rev.* **B 19** 2876 (1979).
- Van Hove L *Phys. Rev.* **95** 249 (1954).
- Vanderbilt D *Phys. Rev.* **B 41** 7892 (1990).
- Yussouff M and Mookerjee A *J. Phys. C : Solid State Phys* **17** 1009 (1984).